

Supplement:
Contrary to widespread belief, the Fresnel zone plate
outperforms the metalens at high NA.

1.1 Metalens design:

A meta-atom is the fundamental building block of a metalens. Meta-atoms are nano-sized cells, each with specific dimensions and geometries, arranged in precise patterns to create the metalens. These meta-atoms exhibit unique optical properties determined by the Locally Periodic Approximation (LPA), where the pitch, Λ subwavelength ($\Lambda < \lambda$). Each meta-atom on the metalens contributes to the desired phase shift necessary for focusing light.

For this study, we implemented a circular nano-post pattern in which each meta-atom was designed as a cylindrical dielectric post mounted on a 0.2 μm -thick glass substrate. Assessing the transmission and reflection characteristics of each meta-atom was crucial for optimal metalens performance. Under the LPA, the transmission and reflection coefficients of a single unit cell could be calculated using periodic boundary conditions in the transverse direction and open boundary conditions in the longitudinal direction.

A Bidirectional Scattering Distribution Function (BSDF) Generation Utility was employed using RSoft FullWAVE FDTD to model light interaction with the meta-atom. The BSDF characterized scattering behavior by defining reflection and transmission across multiple directions, taking into account variables such as incident angle, wavelength, and polarization. During the BSDF generation, a parametric scan was performed across meta-atom cylinder lengths (0.01 μm to 0.50 μm) and widths (0.0102 μm to 0.36 μm) to build a comprehensive scattering profile. The compiled BSDF library was used to determine the optimal lens design with desired target in MetaOptic Designer (MOD), an inverse-design tool from Synopsys. Using this BSDF data, MOD automated the metalens design, optimizing the configuration to achieve the target optical performance. This iterative design approach ensured the most effective arrangement of meta-atoms, tailored to desired specifications through an inverse-design process. There is a parameter of period, which is the center-to-center spacing between the meta-atoms. MOD uses the meta-atom period as a computation grid, so that the XY resolution is fixed by the lattice period. The period, or spacing of the meta-atoms, of the lens was set to 0.3 μm as this was found to be optimal.

The phase profile of the meta-atoms for a metalens is typically defined as:

$$\Psi(x, y, \lambda) = -\frac{2\pi}{\lambda} (\sqrt{x^2 + y^2 + F^2} - F)$$

The maximum meta-atom width (0.36 μm) exceeded the period (0.3 μm), leading to overlapping meta-atoms in the metalens structure. The metalens was designed with a diameter of 100 μm and a focal length of 9.89 μm , resulting in a numerical aperture (NA) of 0.98, optimized to focus 647 nm wavelength light. The dielectric material used has a refractive index of 1.5039, while the glass substrate has a refractive index of 1.4566.

The generated metalens .ind file from MetaOptic Designer (MOD) was subsequently exported to RSoft FullWAVE FDTD for comprehensive validation through a full 3D simulation. Additional details are provided below.

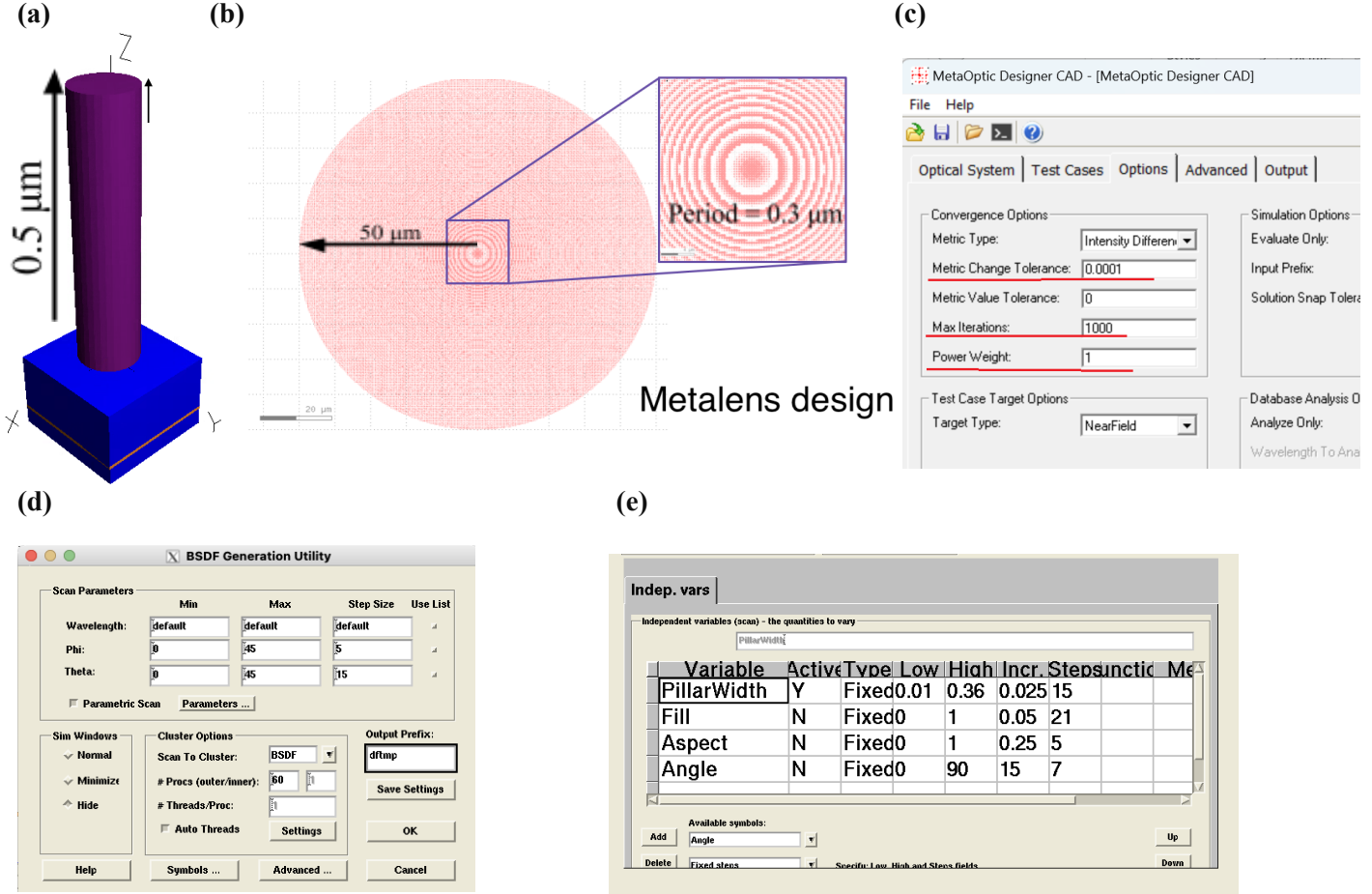


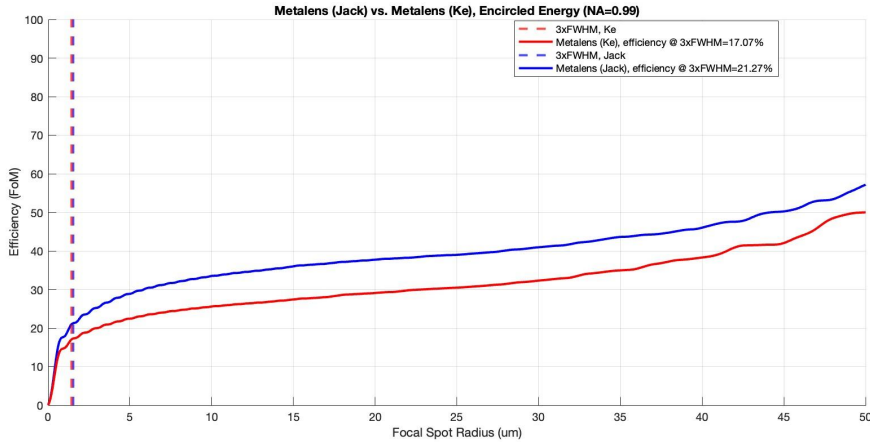
Fig S1.1: Metalens design setup: (a) Meta-atom design of a cylindrical dielectric post mounted on a 0.2 μm-thick SiO₂ substrate. (b) The period, or spacing of the meta-atoms, of the lens was set to 0.3 μm as this was found to be optimal. (c) Settings used in MetaOptic Designer for creating metalens design given BSDF library. (d) Settings for generating BSDF library. (e) Parametric scan used for BSDF library generation.

1.2 Additional Metalens Design:

To evaluate the effectiveness of our metalens design relative to other configurations, we collaborated with Ke Liu (ke.liu2@synopsys.com), an Applications Engineer at Synopsys, to create an additional design based on our parameters (Diameter = 100 μm, Focal Distance = 9.89 μm, NA = 0.98, Wavelength = 0.647 μm, Refractive Index = 1.5039). Ke developed a metalens with a period of 0.325 μm and meta-atom pillar widths ranging from 0.0102 μm to 0.3 μm. As his period was larger than the widest pillar, this alternative design avoided overlapping pillars, unlike our original configuration. Both metalens designs were then simulated under identical conditions (details provided below), followed by an in-depth analysis comparing their performance. The primary metrics assessed were the point spread function (PSF)

and encircled energy in the XZ plane. The analysis concluded that our original design, with a period of 0.3 μm and maximum pillar width of 0.36 μm , outperformed the alternative by exhibiting superior focusing efficiency.

(a)



(b)

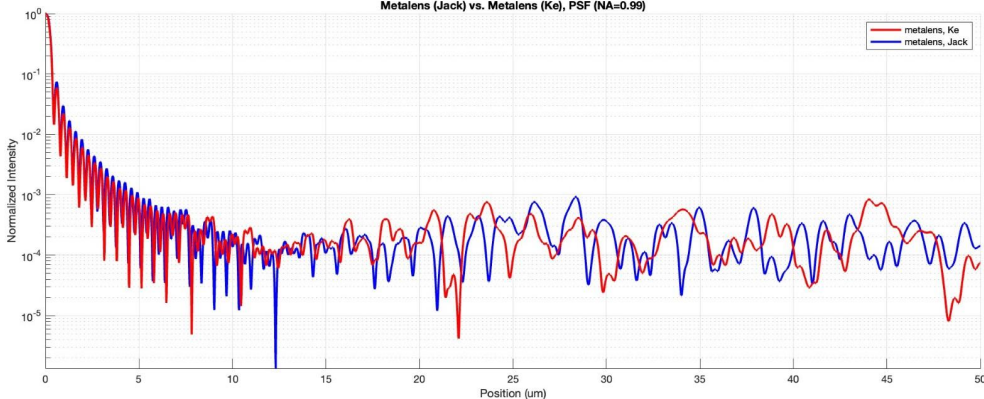


Fig S1.2: Figures comparing metalens designs: (a) Encircled energy comparison in the XZ plane between two lenses of varying period. The lens with smaller period = 0.3 μm demonstrated a higher efficiency. (b) Point Spread function comparison in the XZ plane. Similarly, the lens with smaller period = 0.3 μm demonstrated a higher efficiency though FWHM was equal for both.

1.3 Design of the Fresnel zone plate (FZP):

The parabolic phase shift was calculated for the FZP design. The parabolic phase shift represents the difference in the optical path length between a point at radial distance r from the optical axis and the central point at the optical axis (where $r = 0$). This phase shift is critical for accurately modeling the behavior of light in the FZP. The parabolic phase shift is given by

$$\text{parabolic shift} = \sqrt{r^2 + f^2} - f$$

where f is the focal length, and r is the radial distance from the optical axis. This equation represents the difference between the actual path length of light traveling along a parabolic surface and the straight-line

path along the axis. To determine the maximum phase shift across the entire lens or aperture, we calculate the shift at the edge, where the radial distance is $\frac{D}{2}$ (half of the lens diameter). The maximum parabolic shift, max parabolic shift1, is given by

$$\text{max parabolic shift} = \sqrt{\left(\frac{D}{2}\right)^2 + f^2} - f$$

where D is the total diameter of the lens. Next, we normalize the difference between the maximum parabolic shift and the current parabolic shift to account for the refractive index of the material. This normalization is essential for describing the propagation of light within a medium with refractive index n_{refr} , and is expressed as:

$$x_0 = \frac{\text{max parabolic shift} - \text{parabolic shift}}{n_{refr}}$$

Finally, to ensure that the phase shift remains within a physically meaningful range, typically within one wavelength, we apply a modular operation. This operation constrains the shift to within the wavelength λ , which is critical for optical interference effects. The adjusted phase shift is given by

$$x_0 = \frac{(x_0 \cdot (n_{refr} - 1)) \bmod \lambda_0}{n_{refr} - 1}$$

These equations describe how parabolic phase shift is calculated for our FZP. The FZP structure resulted in 4892 rings, min Ring Width = 0.0102 μm and max Ring Height = 1.28 μm .

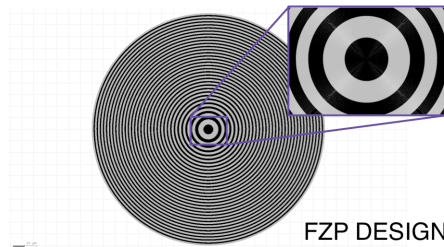


Fig S1.3: Figure of the FZP design highlighting its 4892 total rings.

1.4 Simulation:

RSoft FullWAVE is a commercial software tool designed for comprehensive optical simulations based on the finite-difference time-domain (FDTD) method, ideal for analyzing light behavior in photonic structures. All simulations were conducted in 3D; however, only the first quadrant of each lens was modeled using radial calculation with assumed symmetry to reduce computational resources. The FDTD technique in RSoft was applied with a grid resolution of 0.02 μm in the x, y directions and 0.05 μm in the z direction (approximately 32 points per wavelength). The FDTD algorithm can detect metasurface features with a minimum of five grid points per feature (with 10 being an empirical ideal). At the current grid size, features as small as 0.02 μm would only register one grid point, which is insufficient. Therefore, this setup effectively detects features down to a size of 0.1 μm (i.e., $0.02 \times 5 = 0.1 \mu\text{m}$). To accurately simulate features as small as 0.01 μm , the grid would need to be reduced to 0.002 μm in the x and y directions. However, this setup would demand extensive computational resources, estimated at 30 days and 188 GB of RAM. The FDTD computation time scales with N^4 , where N is the total number of grid

points, reflecting an additional time-dimension complexity in 3D FDTD simulations. The simulation region was confined within boundaries of $51 \times 51 \times 14 \mu\text{m}^3$, surrounded by a Perfectly Matched Layer (PML) with a thickness of $1 \mu\text{m}$ to minimize boundary reflections. Four monitors were positioned on the XZ, YZ, XY exit-plane, and XY focal-plane to measure energy density and electric field components (E_x , E_y , and E_z). Efficiency was determined as the ratio of the energy within a $3 \times \text{FWHM}$ radius at the focal plane over the total energy in the exit plane. A plane wave with a wavelength of 647 nm and transverse electric (TE) polarization was introduced at normal incidence. Each simulation was run on 60 processors with 2 TB of RAM and completed in approximately 8 hours.

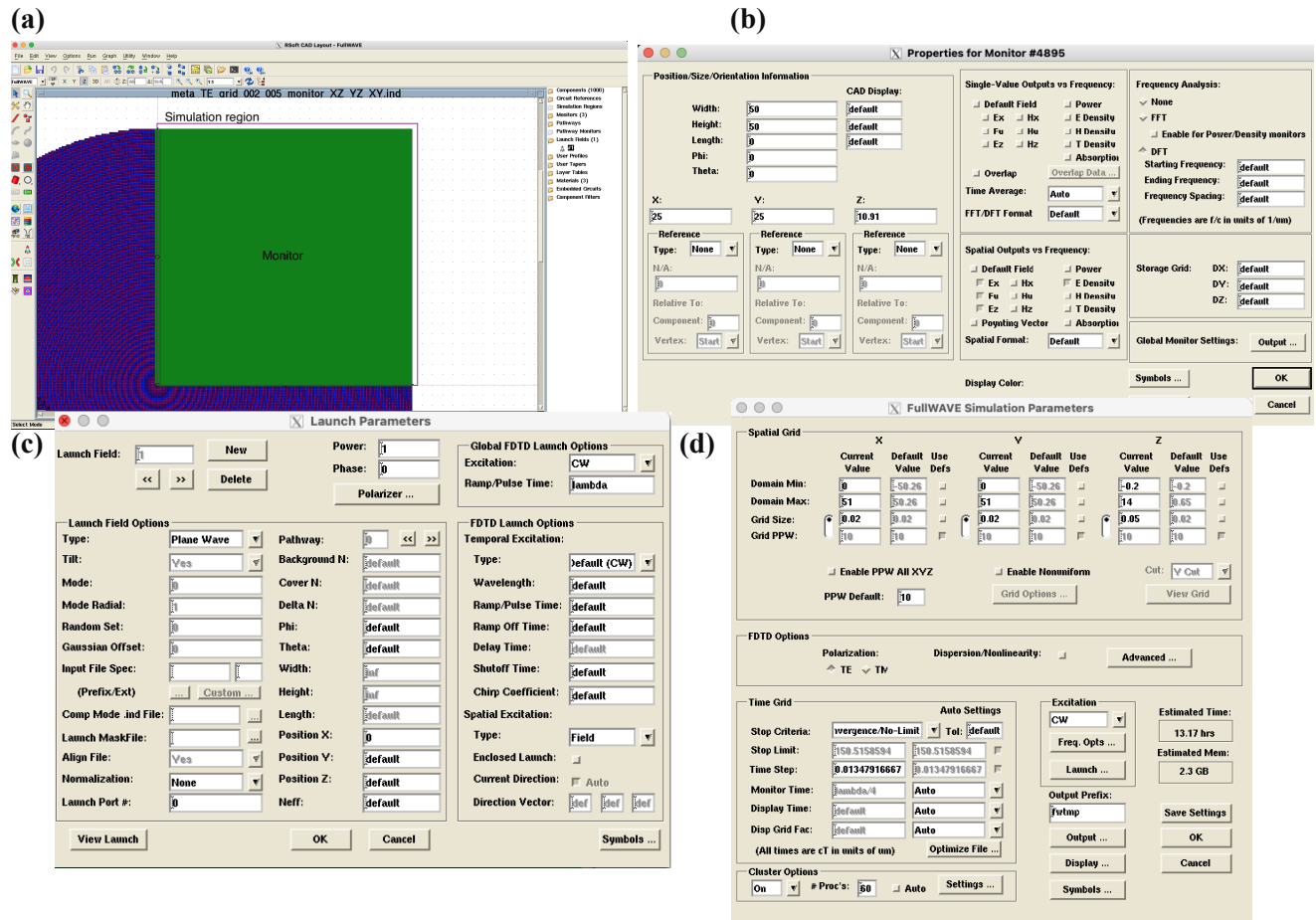


Fig S1.4: Simulation parameters for FDTD simulation in RSoft. (a) Simulation region shown in purple square with green showing monitored position. (b) Monitor settings. Only variation between other monitors was position. (c) Launch parameters including incident light settings. (d) Simulation parameters including resolution and region.

1.5 Validation:

To validate our results, we conducted simulations using an additional FDTD software, MEEP (MIT Electromagnetic Equation Propagation). MEEP is an open-source FDTD tool designed for simulating light behavior in complex photonic structures, similar to RSoft FullWAVE. Both RSoft FullWAVE and MEEP are widely used in photonics research, and theoretically, they should produce

equivalent results under identical simulation structures, parameters, and boundary conditions. We verified this equivalency by simulating an XZ slice of the Fresnel Zone Plate (FZP) in both softwares. In each simulation, a monitor was positioned in the XZ plane to measure energy density within the region. Following the simulations, we conducted a detailed metric analysis of the results using MATLAB. Both MEEP and RSoft produced nearly identical focal point shapes and focal shifts: MEEP recorded a focal shift to 9.5470 μm , while RSoft measured 9.5484 μm . Additionally, both simulations showed comparable depth of focus (DOF) values, with RSoft returning 0.74053 μm and MEEP showing 0.74058 μm . Radial intensity results also aligned closely, each displaying a full-width at half-maximum (FWHM) of 0.41294 μm . The encircled energy and figure of merit (FoM) metrics were similarly consistent between the two tools, with RSoft yielding an FoM of 26.68 and MEEP reporting 26.81. The encircled energy plots from both simulations overlapped almost perfectly, indicating highly reliable results across both software platforms.

As shown in all figures and tables, the results from RSoft and MEEP simulations are nearly identical when simulating the same lens under equivalent FDTD conditions. Metric variations between the two software platforms were minimal, with differences of less than 0.002 μm in focal distance, depth of focus (DOF), focal shift, and FWHM. Efficiency varied by only 0.17%, and intensity profiles and focal shapes were virtually indistinguishable. Thus, we conclude that MEEP and RSoft produce sufficiently consistent results, confirming the accuracy of the FZP simulation results, as they have been successfully reproduced in two different FDTD software platforms.

Beyond validating the FZP, the metalens simulation results were independently verified using a different approach. The metalens design was simulated by two individuals on two separate systems, and the outcomes were compared. Our simulation was conducted on a server with 60 cores and 2 TB of RAM, while the second simulation was performed by Ke Liu (ke.liu2@synopsys.com), an Applications Engineer at Synopsys (developer of RSoft), on a system with 16 cores and 120 GB of RAM. Both simulations adhered to the same protocols and parameters, as detailed above. The results were consistent across both setups, thereby validating the metalens simulation outcomes.

(a)

| Metric | Metalens (Local) | Metalens (Synopsis) |
|----------------------------------|------------------|---------------------|
| Efficiency (FoM) | 21.57 | 21.27 |
| FWHM (μm) | 0.51465 | 0.51465 |
| DOF (μm) | 0.70110 | 0.70090 |
| Focal Distance (μm) | 9.89 | 9.89 |

(b)

| Metric | RSoft | MEEP |
|----------------------------------|---------|---------|
| Efficiency (FoM) | 26.68 | 26.81 |
| FWHM (μm) | 0.41294 | 0.41294 |
| DOF (μm) | 0.74053 | 0.74058 |
| Focal Distance (μm) | 9.5470 | 9.5484 |

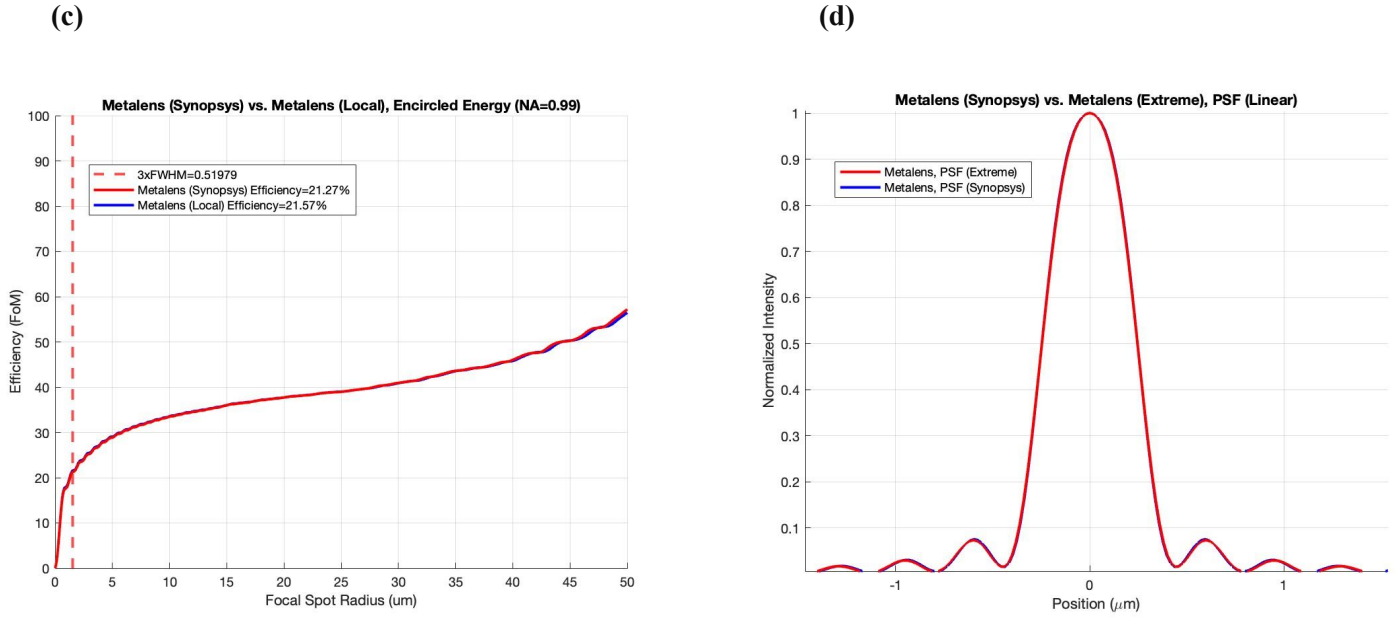


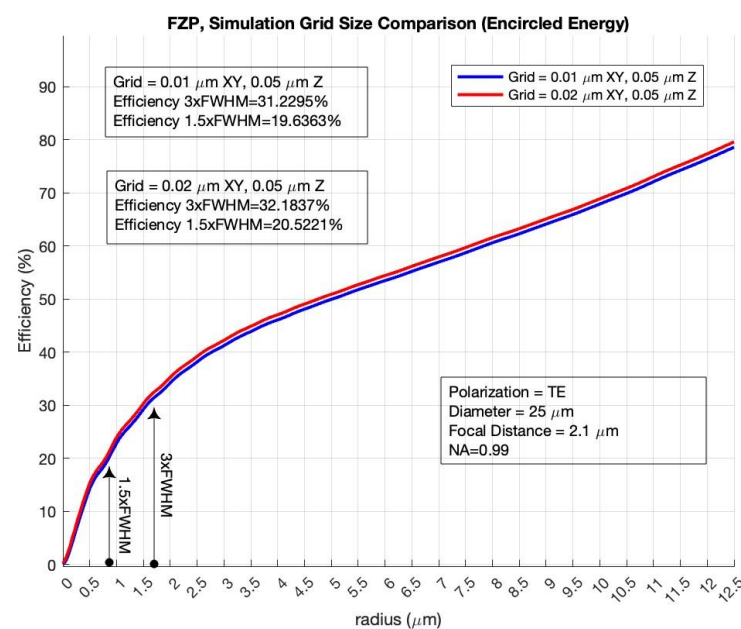
Fig S1.5: Validation results. (a) Metalens results from simulation on a machine with 60 cores and 2 TB of RAM (Local) vs. results from simulation on a machine with 16 cores and 120 GB of RAM (Synopsys). (b) FZP simulation results from different FDTD softwares (RSoft vs. MEEP). (c) Encircled energy comparison demonstrating equivalence in Local vs. Synopsys simulations. (d) Point Spread Function plot comparison demonstrating equivalence in Local vs. Synopsys simulations.

1.6 Check for convergence:

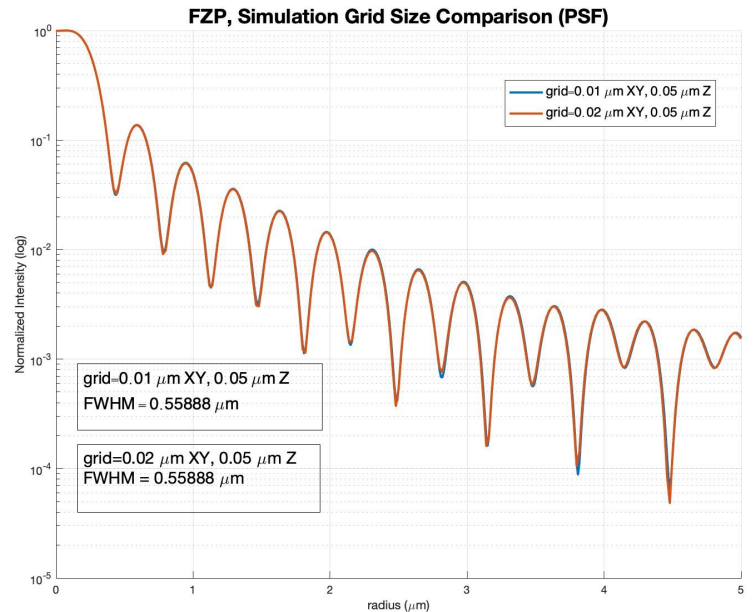
To rigorously validate the adequacy of the selected spatial resolution (20 nm in the XY plane and 50 nm in the Z-direction) for our simulations, we performed supplementary analyses employing a finer resolution grid (10 nm in XY and 50 nm in Z). All other simulation parameters—such as the computational domain, polarization state (TE), and illumination incidence from the substrate—were held constant to isolate the influence of grid resolution on the outcomes. To further probe resolution-dependent effects under varying optical constraints, the lens diameter was systematically reduced from 100 μm to 25 μm, with the focal length correspondingly scaled from 9.89 μm to 2.47 μm, maintaining a numerical aperture (NA) of 0.98. This downsizing accentuated the impact of grid granularity on the simulated optical performance.

Convergence of the results was evaluated by comparing key output metrics—such as full width at half maximum (FWHM), encircled energy, and efficiency—across the two resolution settings. The finer grid (10 nm XY, 50 nm Z) yielded results that were statistically indistinguishable from those obtained with the coarser grid (20 nm XY, 50 nm Z), with discrepancies in performance metrics falling below the threshold of practical significance. This convergence substantiates that the chosen resolution of 20 nm in XY and 50 nm in Z provides sufficient numerical fidelity for capturing the physics of the system across all simulated configurations, thereby optimizing computational efficiency without compromising accuracy.

(a)



(b)



(c)

| FWHM (XZ) (μm) | | FWHM (YZ) (μm) | | Efficiency at FWHM*3 (XZ) (%) | | Efficiency at FWHM*1.5 (XZ) (%) | | Depth of Field (μm) | |
|--------------------------------|----------------|--------------------------------|----------------|-------------------------------------|----------------|---------------------------------------|----------------|-------------------------------------|----------------|
| Fine Grid | Coarse Grid | Fine Grid | Coarse Grid | Fine Grid | Coarse Grid | Fine Grid | Coarse Grid | Fine Grid | Coarse Grid |
| 0.55888 | 0.55888 | 0.25979 | 0.25979 | 31.2295 | 32.1837 | 19.636 | 3 | 20.5221 | 8 |

Fig S1.6: Check for convergence of grid size. (a) Encircled energy plot comparison between varying grid resolutions (Fine vs. Coarse) demonstrating convergence. (b) Point Spread Function plot comparison between varying grid resolutions (Fine vs. Coarse) also demonstrating convergence. (c) Table highlighting simulation results between two resolutions demonstrating convergence.

To extend this analysis, we simulated rotationally symmetric two-dimensional (2D) slices of an equivalent Fresnel Zone Plate (FZP) structure, comparing grid resolutions of 20 nm XY, 50 nm Z against a finer 10 nm XY, 10 nm Z. The results, illustrated in Fig. S1.7, demonstrates convergence across both grid sizes, with the coarser 20 nm XY, 50 nm Z resolution proving sufficient for accurately modeling the optical behavior. This additional check reinforces the reliability of our baseline resolution for structures with cylindrical symmetry, where grid-induced artifacts might otherwise be pronounced.

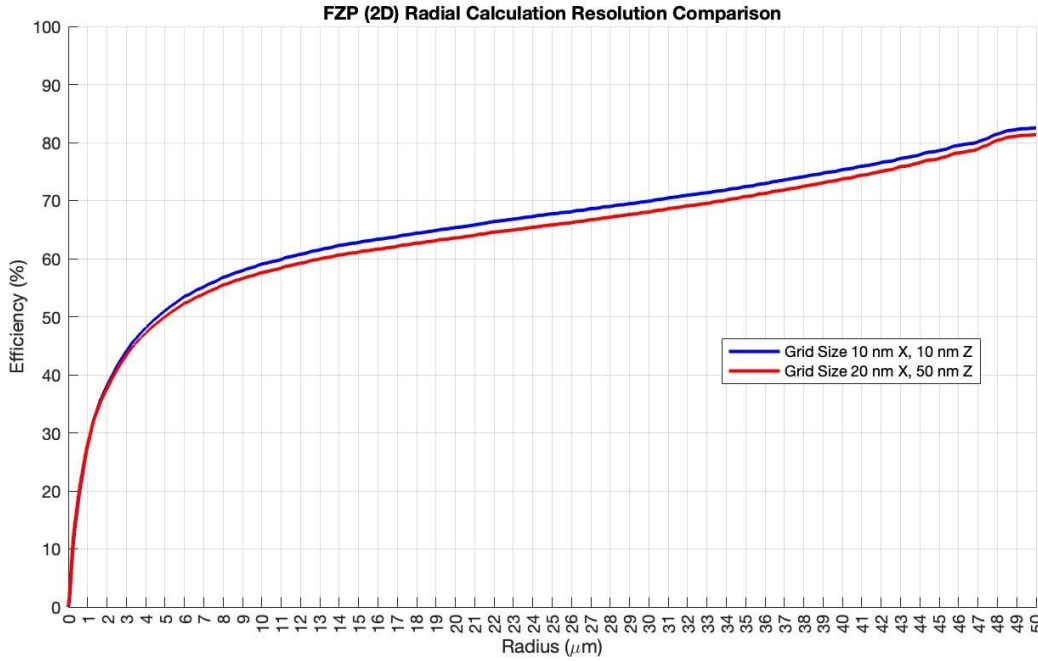


Fig S1.7: Plots of encircled energy for both grid sizes overlap closely, validating that the 20 nm XY, 50 nm Z grid resolves the energy distribution with precision comparable to the finer mesh.

1.7 Check for Transmission loss through Opaque Aperture around Lens

To investigate the potential influence of stray light on the performance of the Fresnel Zone Plate (FZP) and to quantify its total transmission efficiency, we conducted a comparative analysis by introducing an opaque chromium aperture surrounding the lens. The FZP configuration remained consistent with prior simulations: a maximum height of 1.28 μm , fabricated with the IPS material with a refractive index of $n=1.5039$, mounted on a glass substrate with $n=1.4566$, a diameter of 25 μm , and a design focal length of 2.5 μm , corresponding to a numerical aperture (NA) of 0.98. In this study, the illumination was configured for negative Z-incidence—i.e., light incident from the air side, focusing into the glass substrate—representing a practical scenario for substrate-side focusing applications.

The key modification in this experiment was the addition of an opaque chromium ring encircling the FZP, designed to block any stray light that does not pass through the lens aperture. This allowed us to isolate the contribution of light transmitted solely through the FZP and assess whether external light leakage around the lens perimeter impacts the simulation outcomes. The chromium ring was modeled as a perfectly opaque boundary, absorbing all incident radiation outside the 25 μm diameter of the lens. We compared this configuration against an identical FZP without the opaque ring, keeping all other parameters—such as illumination wavelength, polarization (TE), and computational domain—unchanged to ensure a controlled comparison.

The primary metrics evaluated were the encircled energy (EE) within the focal spot and the total transmission efficiency, defined as the ratio of power reaching the focal plane to the transmitted power. Simulations were performed using FDTD in RSoft, with a spatial resolution of 20 nm in the XY plane and 50 nm in the Z-direction, as validated in Section 1.6. The results revealed that the encircled energy profiles for the FZP with and without the opaque chromium ring were effectively identical, with

differences falling below the numerical precision of the simulation (e.g., <0.5% variation in EE). Similarly, the total transmission efficiency remained consistent across both configurations, indicating that stray light bypassing the lens aperture does not measurably contribute to the focal plane intensity under these conditions.

These findings suggest that, for the specified FZP design and incidence geometry, the lens captures and focuses the vast majority of incident light, with negligible transmission losses attributable to regions outside the 25 μm aperture. The equivalence in performance with and without the opaque ring further implies that the simulation domain boundaries and incident beam profile (plane wave) were appropriately defined to exclude artifacts from peripheral light. This validates the robustness of our baseline FZP model for efficiency assessments and confirms that additional aperturing is unnecessary for accurate simulation of this system. Thus, all further simulations were performed without the need of an opaque aperture.

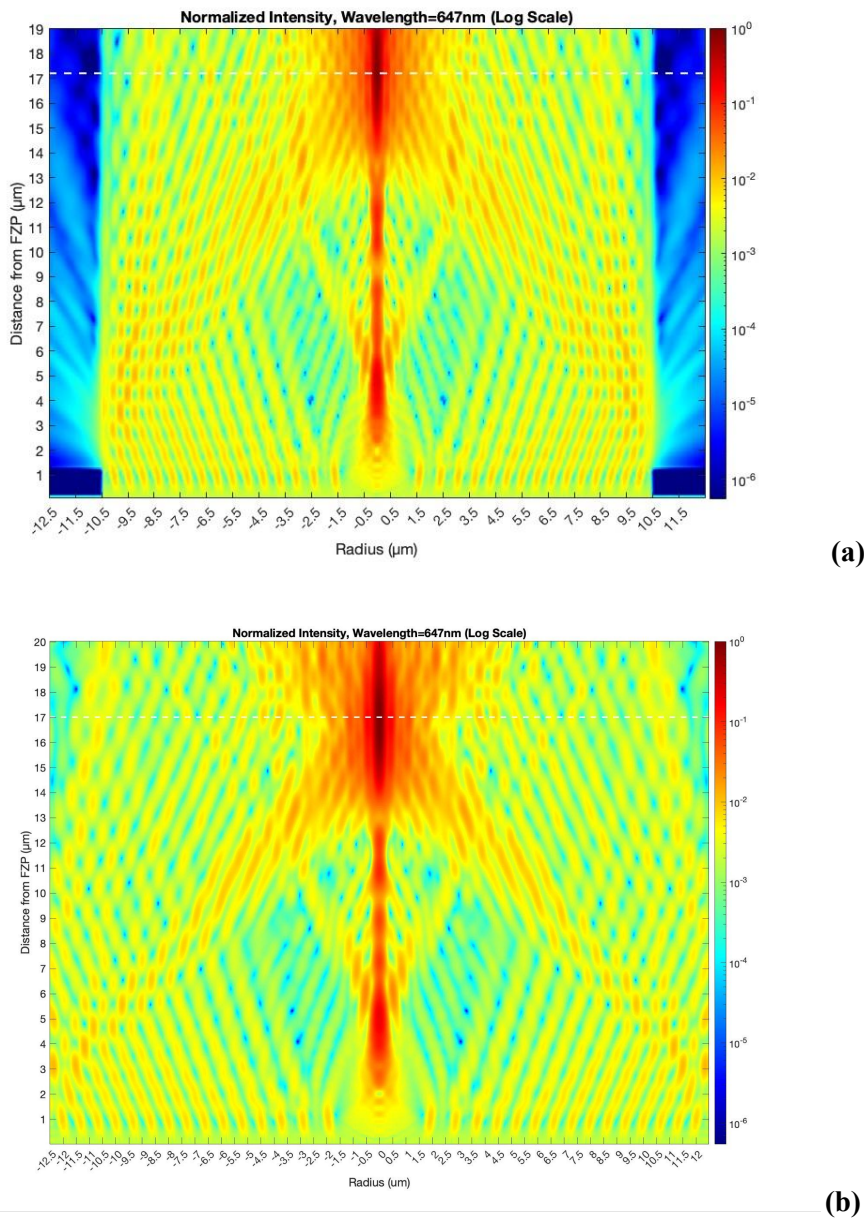


Fig S1.8: Simulated PSF in the XZ plane for the FZP with opaque ring (**a**) and FZP without opaque ring (**b**) with diameter = 25 μm , focal length 17 μm , and incidence from air. Note that the efficiency of the FZP without Opaque ring was 15.8379% and with aperture was 15.4457%

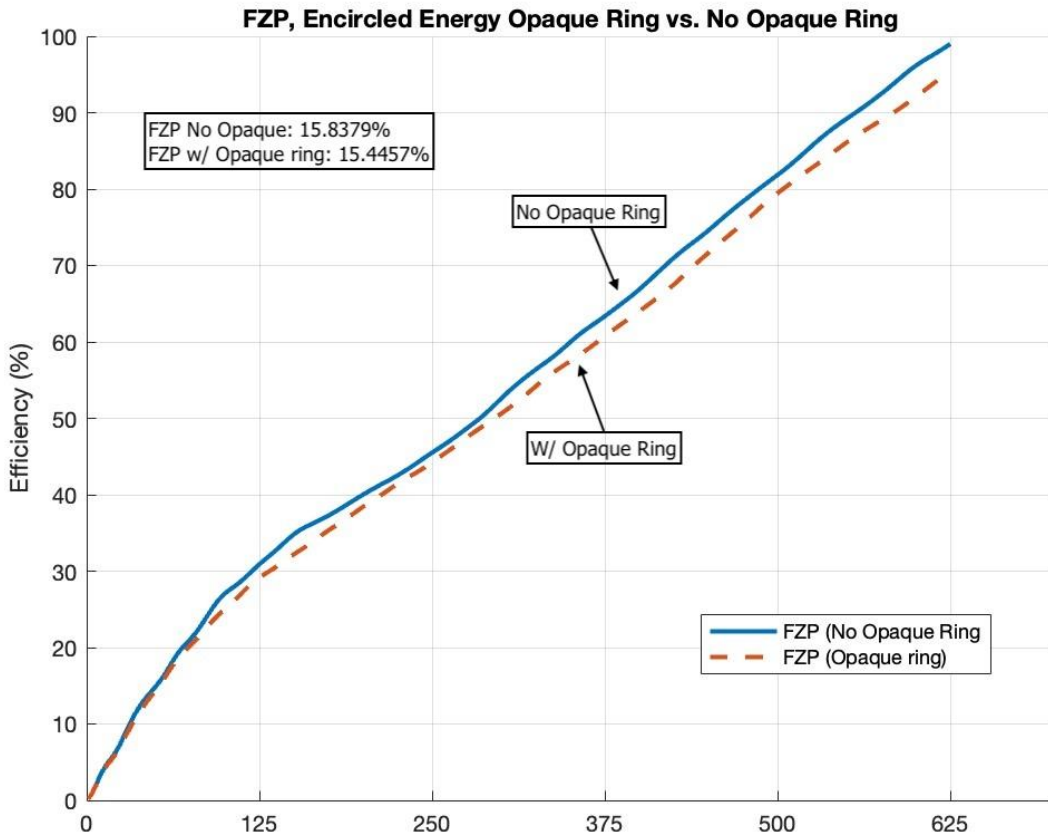


Fig S1.9: Simulated encircled power in the XY (focal) plane for the metalens (red) and FZP (blue) with diameter = 25 μm , focal length = 17 μm , and incidence from substrate. Efficiencies corresponding to the different radii are labeled. Clearly, the FZP outperforms the metalens in terms of efficiency.

1.8 Comparison of FZP and metalens with diameter = 25 μm and glass substrate.

Simulations were conducted to compare the performance of the Fresnel Zone Plate (FZP) lens and the metalens, both designed with a 25 μm diameter on a glass substrate, while maintaining a numerical aperture (NA) of 0.98, corresponding to a focal distance of 2.5 μm . The specific design parameters and geometries of the two lenses are summarized in Fig S1.7. Both lenses were tested under normal incidence from the substrate side (glass) and the air side, with all simulations using Transelectric (TE) polarized light. The same process was repeated with 50 μm diameter devices as well.

A key factor affecting performance was the incidence medium. When light was incident from air, the focusing efficiency of both lenses was cut in half compared to incidence from the glass substrate. This efficiency drop is attributed to reflection losses at the air-glass interface, which prevent a significant portion of the incident light from coupling into the lens structure. Also with illumination from air, both

lenses saw a focal shift from $\sim 2.5 \mu\text{m}$ to $\sim 17 \mu\text{m}$ measured from the lens edge. This corresponds to a numerical aperture of 0.59, a significant shift from the 0.98 design. In contrast, illumination from the glass side improved transmission, leading to higher focusing efficiency for both the FZP and metalens, and the focal point remained at the designed distance of $\sim 2.5 \mu\text{m}$.

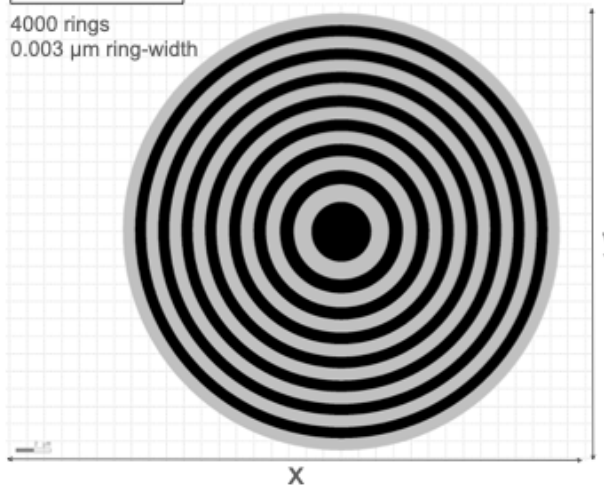
Additionally, shadowing effects played a significant role in the FZP lens performance, particularly under air-side incidence. Due to the discrete nature of the zone plate rings, certain regions received less direct illumination, reducing their contribution to the overall focusing efficiency. This effect was less pronounced for substrate-side incidence, where light could couple more effectively into the phase-altering zones of the FZP. The metalens, with its continuous phase profile, exhibited a more uniform response but still suffered from efficiency losses when illuminated from air. Our findings highlight the strong dependence of both lenses on illumination conditions, particularly the incidence medium, which affects light transmission, phase accumulation, and overall focusing performance. The results are summarized in Fig S1.9-S1.15.

(a)

Diameter = 25 μm
Focal distance = 2.67 μm
 $\lambda = 647 \text{ nm}$
NA=0.98

FZP

4000 rings
0.003 μm ring-width

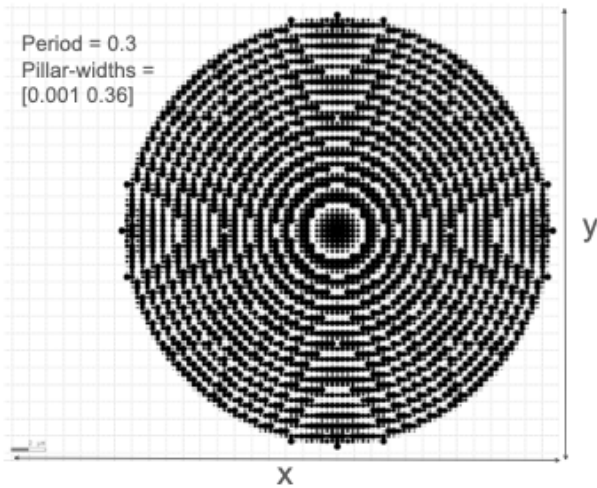


(b)

Grid Size = 0.02 μm XY, 0.05 μm Z
PPW=32.35
TE Polarization

Metalens

Period = 0.3
Pillar-widths =
[0.001 0.36]



(c)

| FWHM (XZ) (μm) | | FWHM (YZ) (μm) | | Efficiency at FWHM*3 (XZ) (%) | | Efficiency at FWHM*1.5 (XZ) (%) | | Depth of Field (μm) | |
|-----------------------------|---------|-----------------------------|---------|-------------------------------|---------|---------------------------------|---------|----------------------------------|---------|
| Metalens | FZP | Metalens | FZP | Metalens | FZP | Metalens | FZP | Metalens | FZP |
| 0.49923 | 0.55911 | 0.26882 | 0.27955 | 10.6019 | 32.2152 | 7.6968 | 20.5422 | 0.65 | 0.88608 |

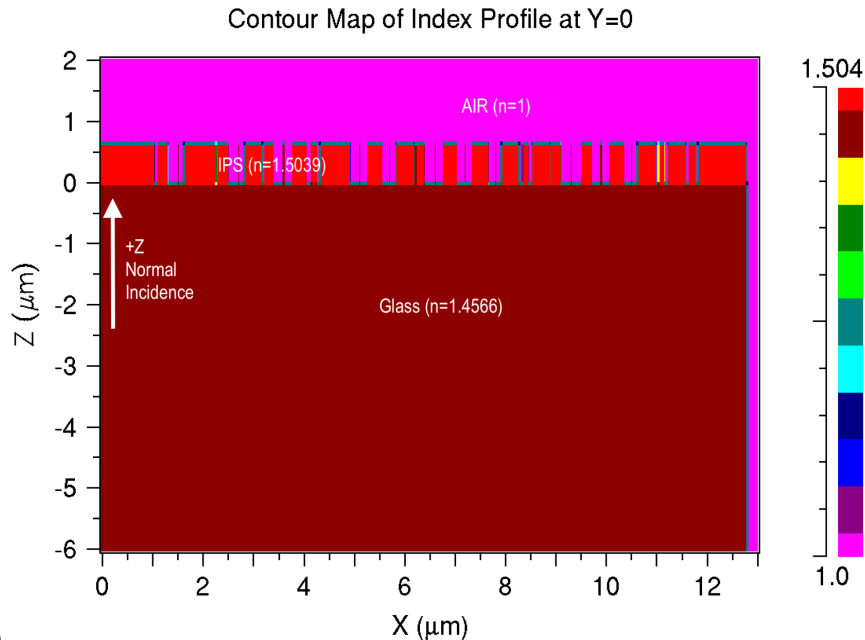
(d)

| FWHM (XZ) (μm) | | FWHM (YZ) (μm) | | Efficiency at FWHM*3 (XZ) (%) | | Efficiency at FWHM*1.5 (XZ) (%) | | Depth of Field (μm) | |
|-----------------------------|-----|-----------------------------|-----|-------------------------------|-----|---------------------------------|-----|----------------------------------|-----|
| Metalens | FZP | Metalens | FZP | Metalens | FZP | Metalens | FZP | Metalens | FZP |
| | | | | | | | | | |

| | | | | | | | | | |
|---------|---------|---------|---------|-------|---------|--------|--------|------|-----|
| 0.39002 | 0.35942 | 0.31201 | 0.23962 | 5.037 | 15.8379 | 3.4863 | 8.4302 | 4.25 | 3.4 |
|---------|---------|---------|---------|-------|---------|--------|--------|------|-----|

Fig S1.10: Metalens (a) and FZP (b) with diameter = $25\mu\text{m}$, and focal length = $2.67 \mu\text{m}$. (c) Incidence from glass substrate results. (d) Incidence from air results.

(a)



(b)

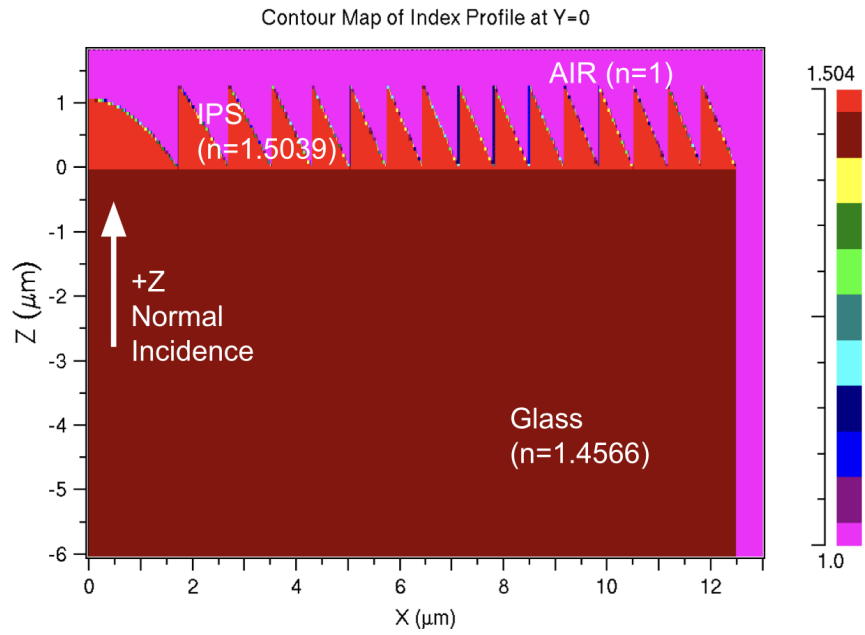


Fig S1.11: Material Profiles of Metalens (a) and FZP (b) with diameter = $25\mu\text{m}$, and focal length = $2.67 \mu\text{m}$ with glass substrate.

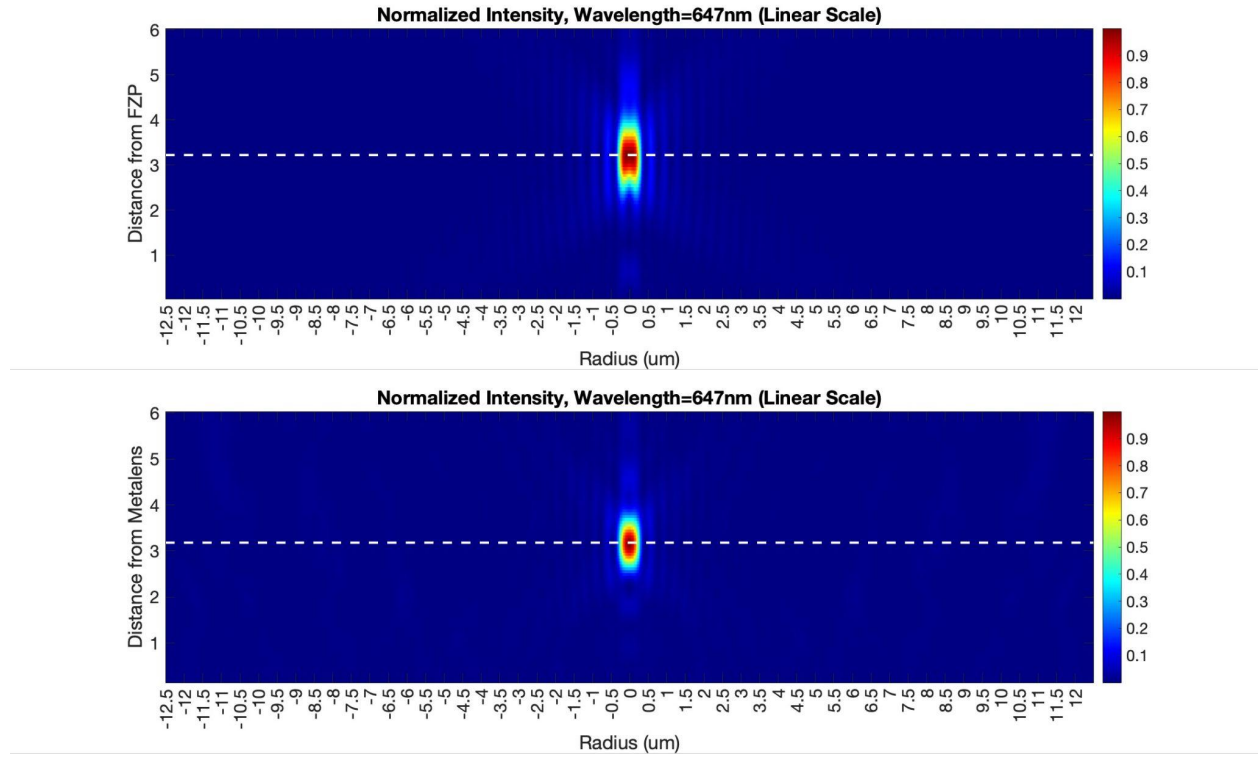


Fig S1.12: Simulated PSF in the XZ plane for the FZP (top) and Metlens (bottom) with diameter = 25 μm , focal length = 2.67 μm , and incidence from substrate. Note that the efficiency of the FZP is 32%, compared to the metalens at 11%.

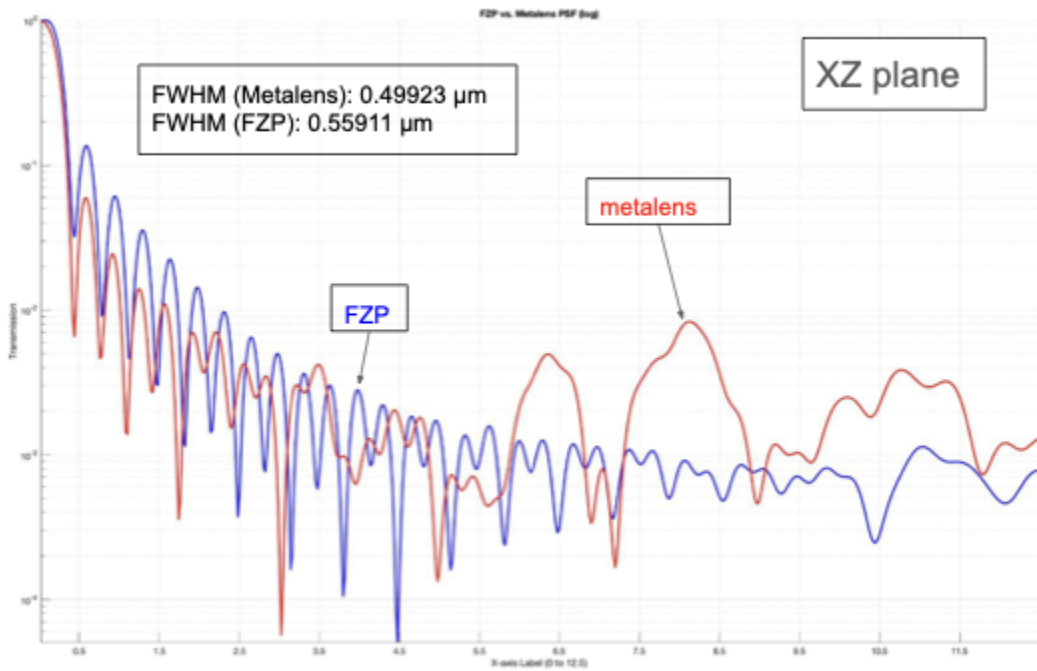


Fig S1.13: Simulated PSF in the XY (focal) plane for the metalens (red) and FZP (blue) with diameter = 25 μm , focal length = 2.67 μm , and incidence from substrate.

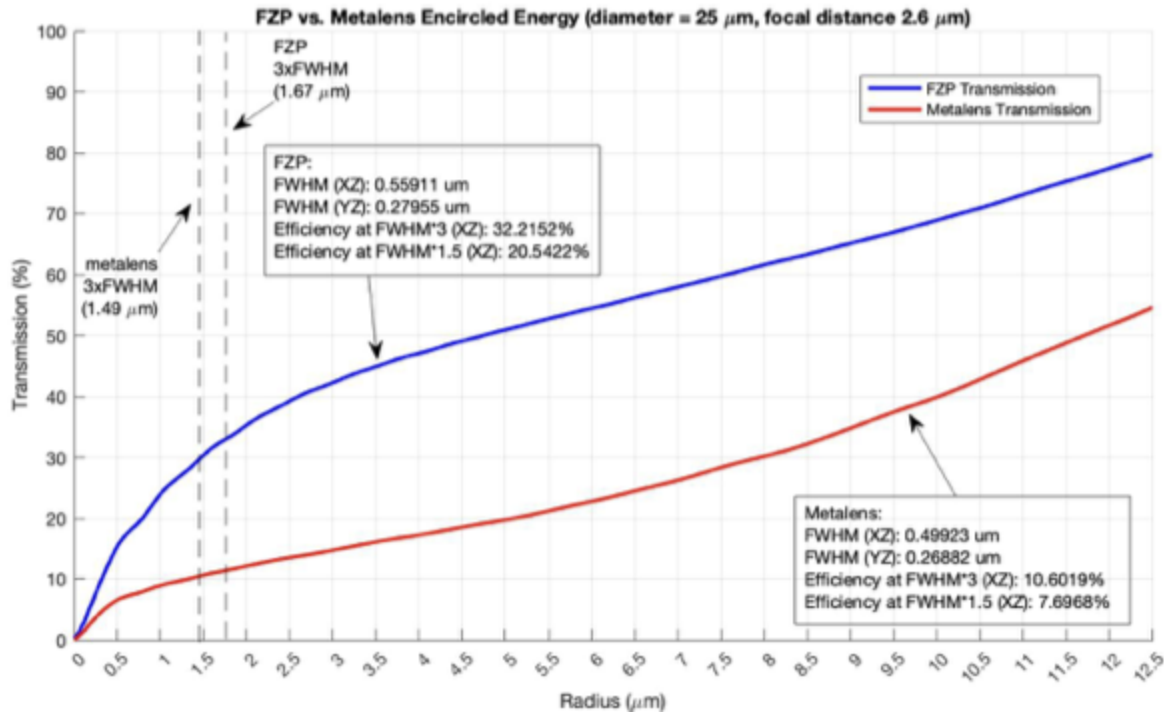
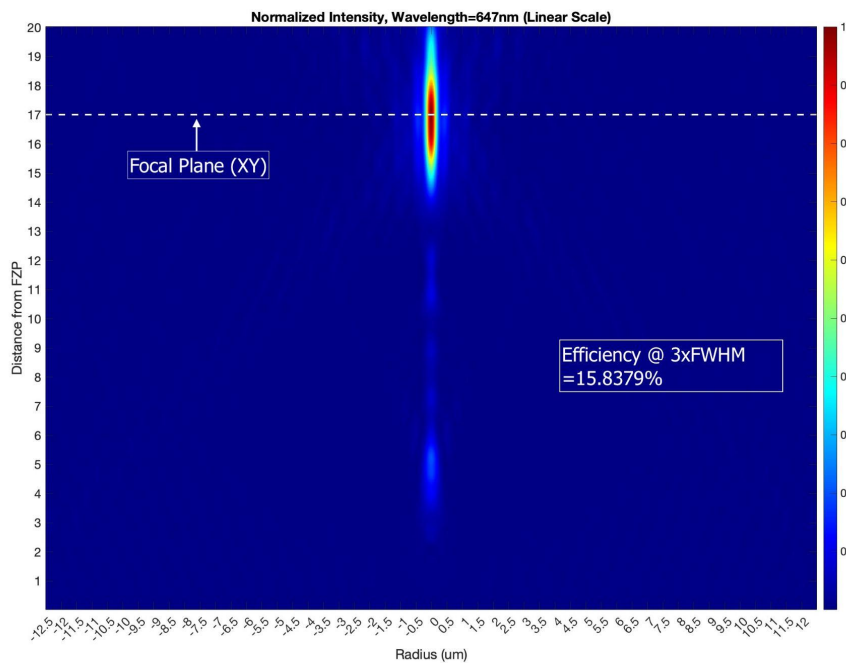


Fig S1.14: Simulated encircled power in the XY (focal) plane for the metalens (red) and FZP (blue) with diameter = 25 μm , focal length = 2.67 μm , and incidence from substrate. Efficiencies corresponding to the different radii are labeled. Clearly, the FZP outperforms the metalens in terms of efficiency.



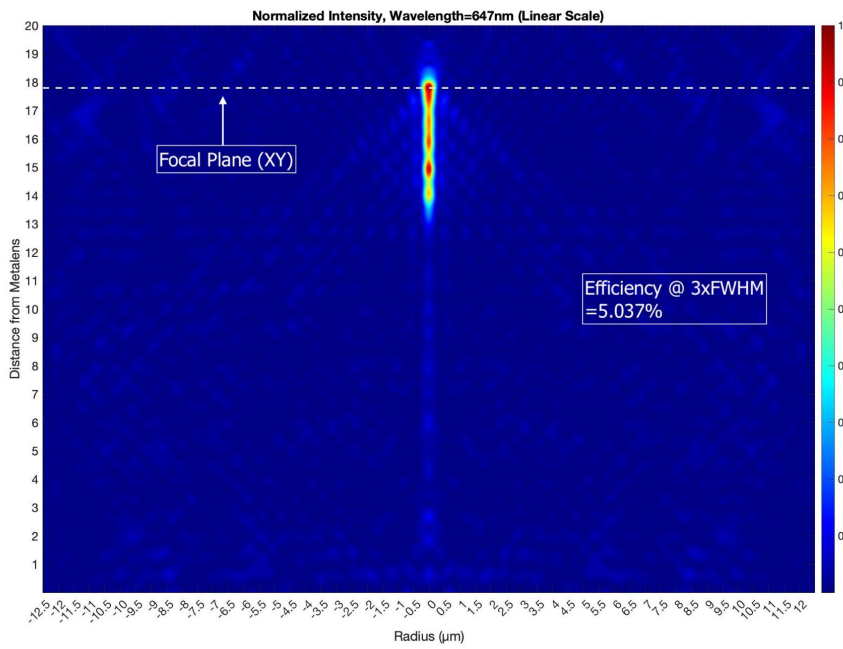


Fig S1.15: Simulated PSF in the XZ plane for the FZP (top) and Metalens (bottom) with diameter = $25\mu\text{m}$, focal length = $17\mu\text{m}$, and incidence from air. Note that the efficiency of the FZP is 16%, compared to the metalens at 5%.

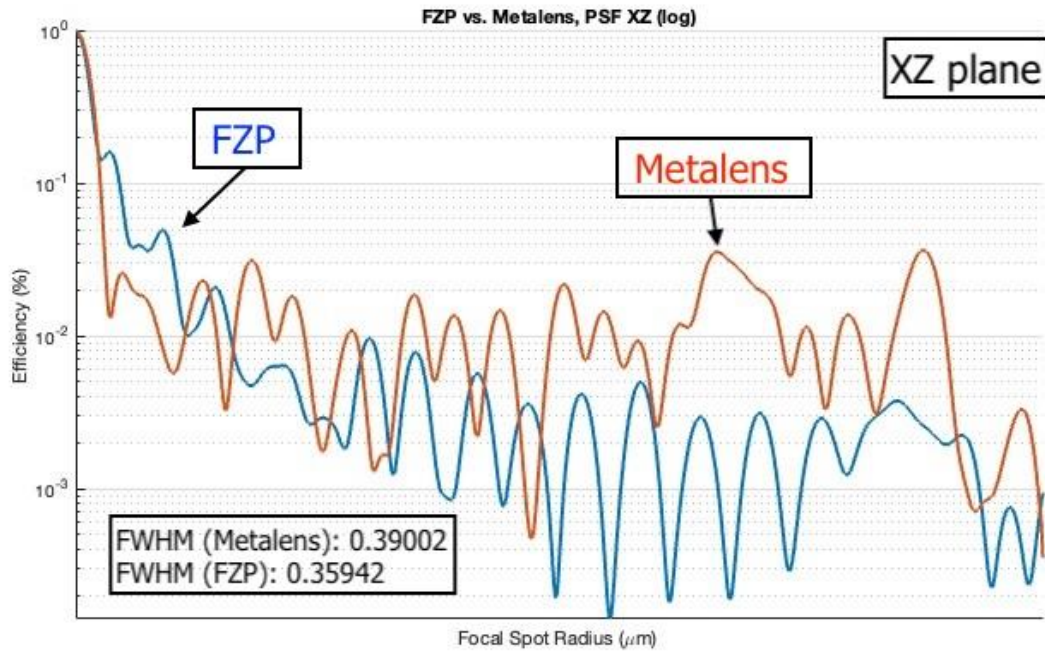


Fig S1.16: Simulated PSF in the XY (focal) plane for the metalens (red) and FZP (blue) with diameter = $25\mu\text{m}$, focal length = $17\mu\text{m}$, and incidence from air.

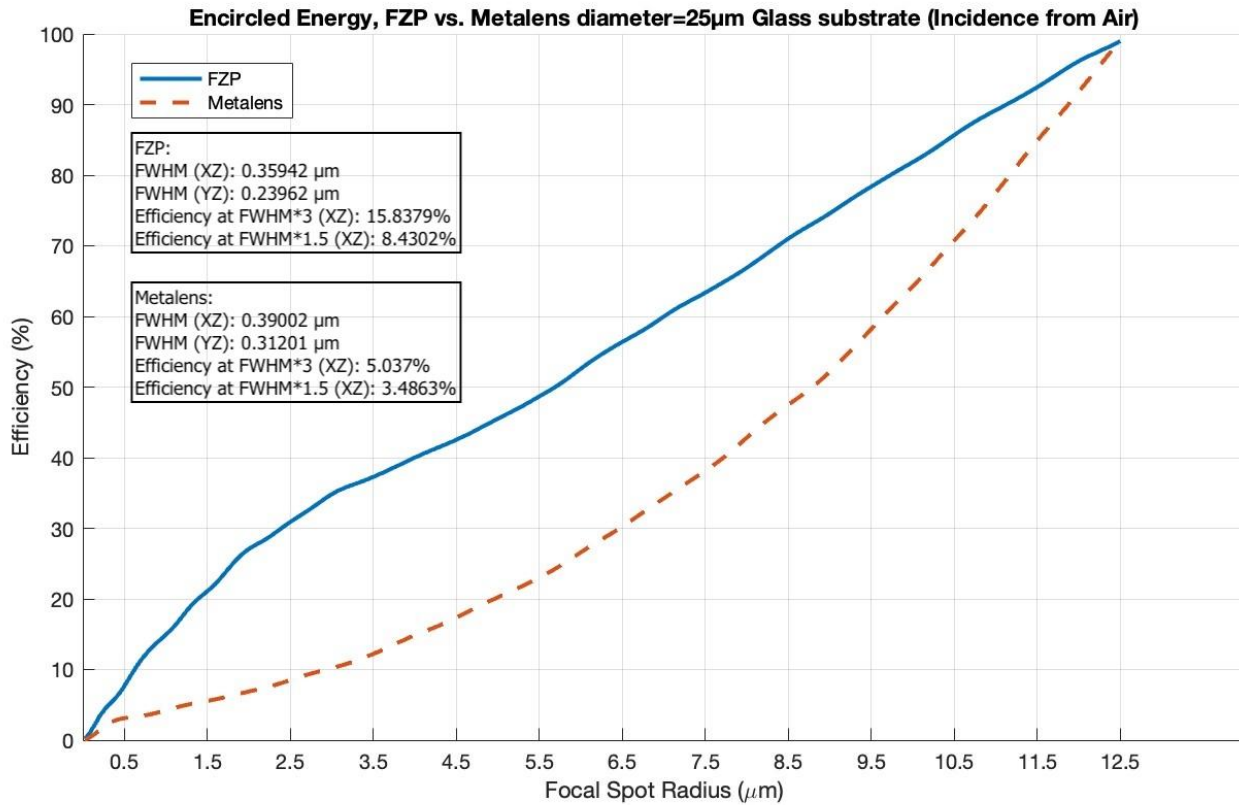


Fig S1.17: Simulated encircled power in the XY (focal) plane for the metalens (red) and FZP (blue) with diameter = 25 μm , focal length = 17 μm , and incidence from substrate. Efficiencies corresponding to the different radii are labeled. Clearly, the FZP outperforms the metalens in terms of efficiency.

1.9 Comparison of FZP and metalens with diameter = 25 μm without substrate.

Simulations were also conducted to compare the performance of the Fresnel Zone Plate (FZP) lens and the metalens at a 25 μm diameter without substrates. All other lens geometries, simulation parameters, and incidence conditions from both directions were kept identical to those in Section 1.7. The specific design parameters and geometries of the two devices are summarized in Figure S1.7 (a) and (b). The results for incidence from glass, summarized in Figures S1.10–S1.12, were equivalent to those for incidence from the air substrate.

Due to the metalens' symmetry about the Z-axis, its simulation results for both incidence directions without a substrate were nearly identical, demonstrating consistent performance regardless of illumination orientation.

The FZP, however, experienced a degradation in performance for incidence from air without a substrate. Due to shadowing, the discrete ring structure of the FZP caused certain regions of the lens to receive less direct illumination, leading to a reduction in their contribution to the overall focusing efficiency. This effect was more pronounced without a substrate, as the absence of a high-index medium (such as glass) further reduced the lens' ability to effectively couple and direct incident light.

These results, summarized in Figures S1.16–S1.18, highlight the increased sensitivity of the FZP to incidence direction in the absence of a substrate, whereas the metalens maintained stable performance due

to its symmetric phase profile about the Z-axis. This is the only case where the metalens outperformed the FZP in terms of efficiency.

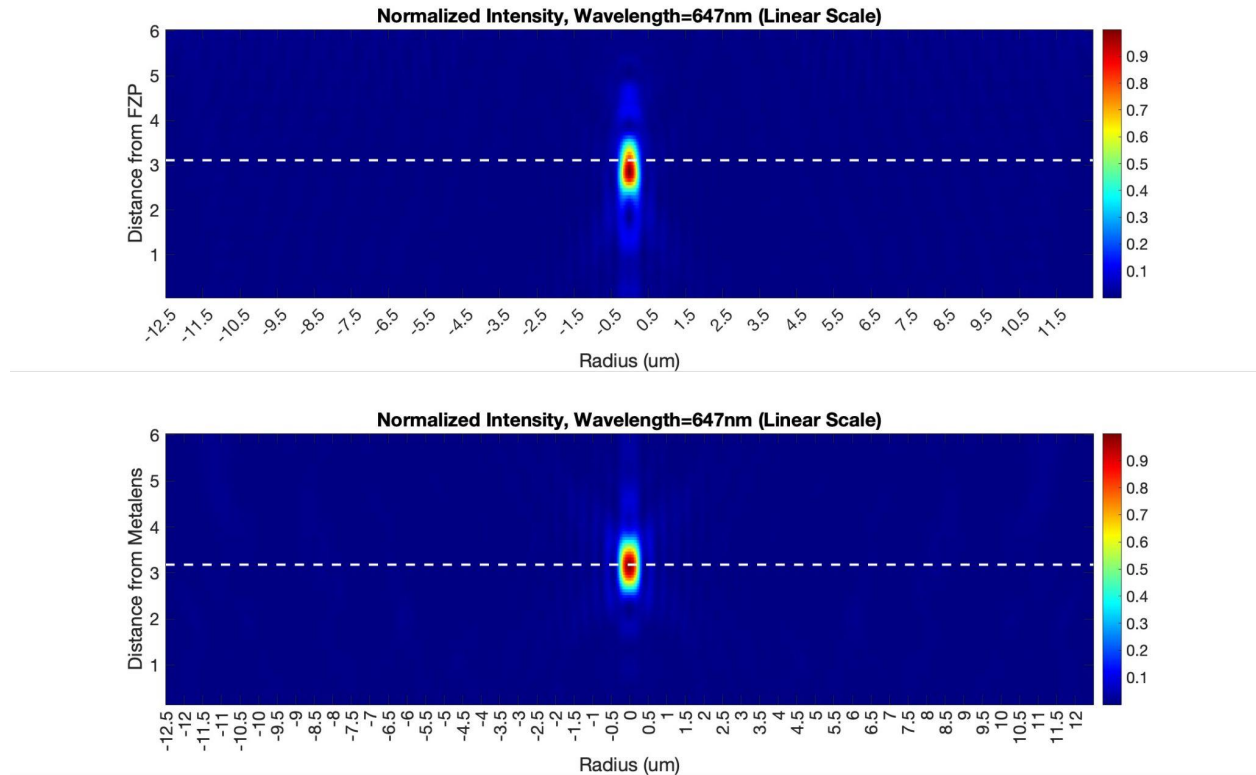
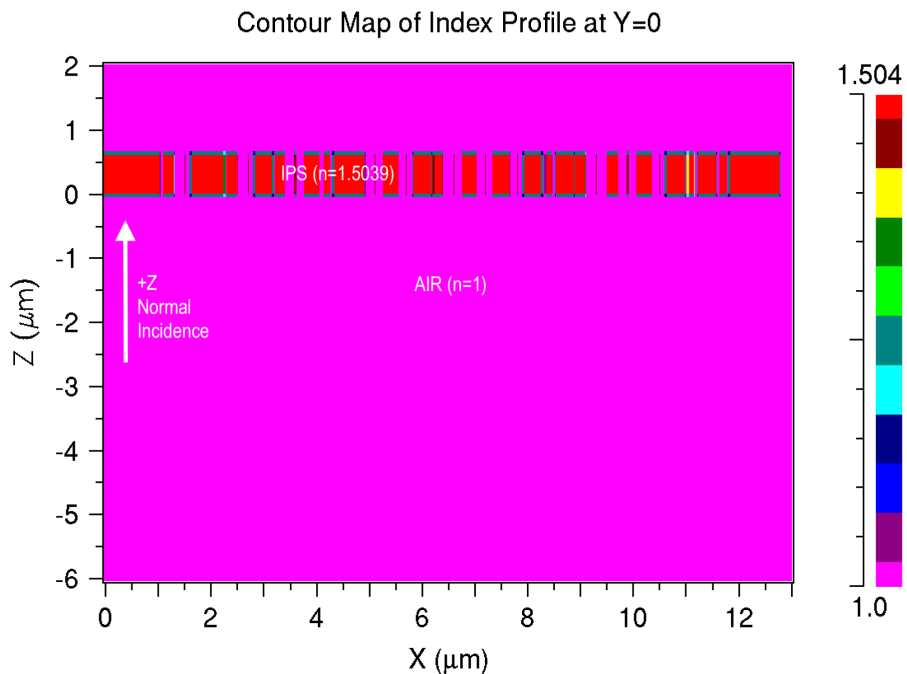


Fig S1.18: Simulated PSF in the XZ plane for the FZP (top) Metalens FZP (bottom) with diameter = 25 μm , and incidence from substrate. Note that the metalens outperformed the FZP in focusing efficiency (FZP at 3.5% compared to the metalens at 11%).

| FWHM (XZ) (μm) | | FWHM (YZ) (μm) | | Efficiency at FWHM*3 (XZ) (%) | | Efficiency at FWHM*1.5 (XZ) (%) | | Depth of Field (μm) | |
|-----------------------------|--------|-----------------------------|---------|-------------------------------|--------|---------------------------------|--------|----------------------------------|------|
| Metalens | FZP | Metalens | FZP | Metalens | FZP | Metalens | FZP | Metalens | FZP |
| 0.50702 | 0.4393 | 0.27301 | 0.27955 | 10.6299 | 3.4526 | 7.5843 | 2.6539 | 0.455 | 0.75 |

Table S1.19: Simulation results for incidence from air and lenses with air substrate (Illumination traveling in -Z direction).

(a)



(b)

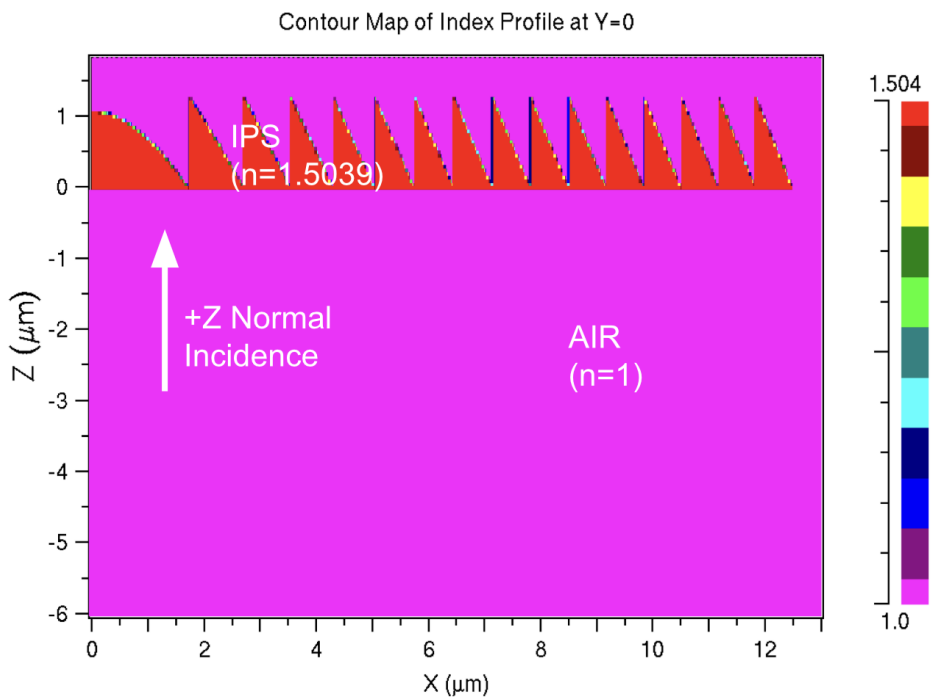


Fig S1.20: Material Profiles of Metalens (a) and FZP (b) with diameter = $25\mu\text{m}$, and focal length = 2.67 um without substrate.

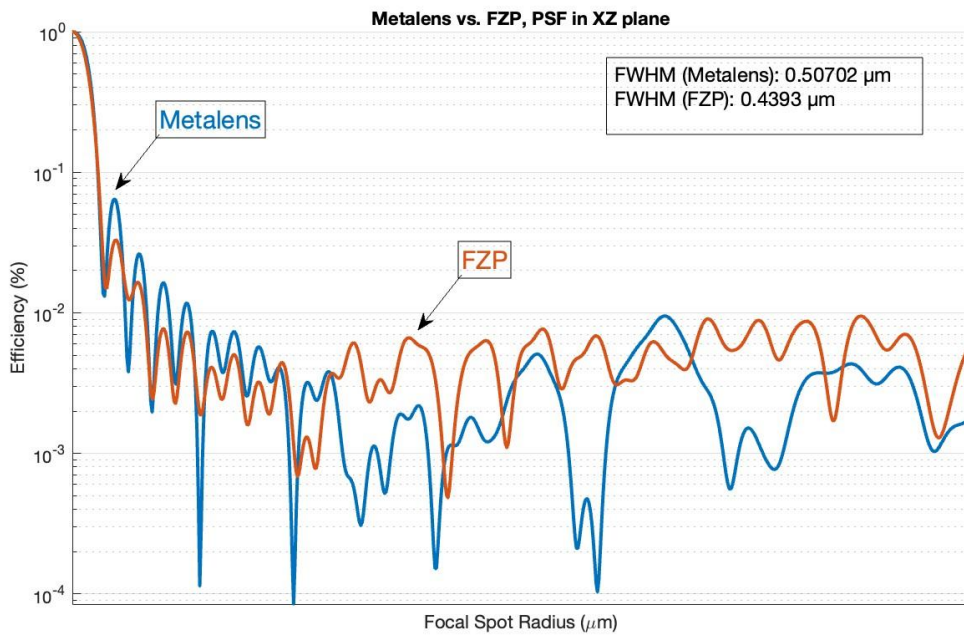


Fig S1.21: Simulated PSF in the XY (focal) plane for the metalens (Blue) and FZP (Red) with diameter = 25 μm , and incidence from air.

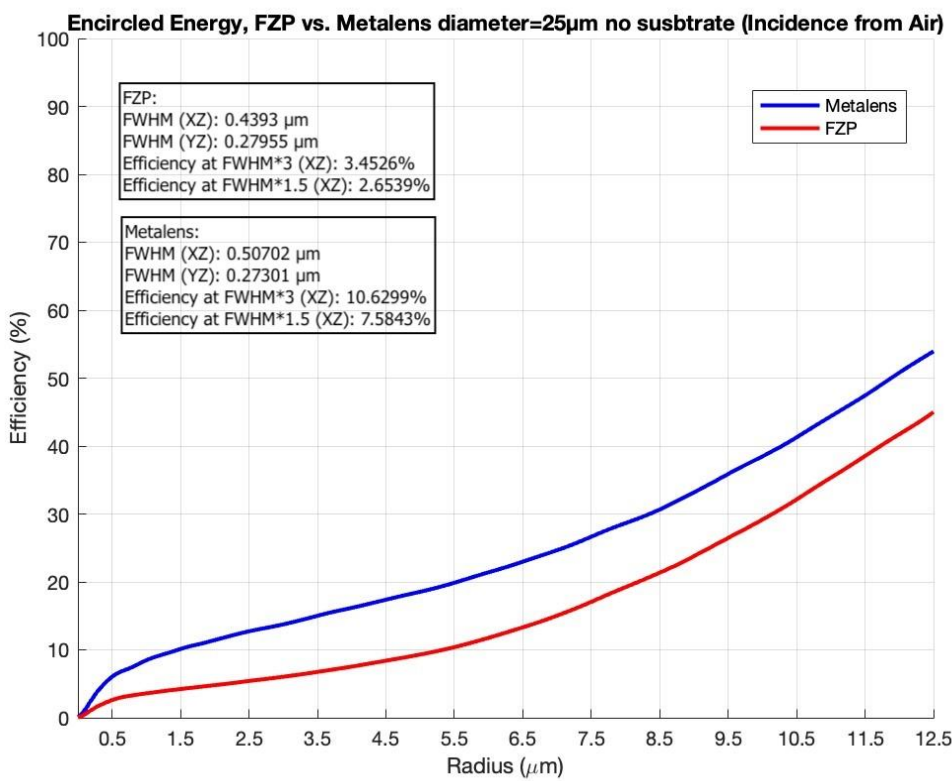


Fig S1.22: Simulated encircled power in the XY (focal) plane for the metalens (blue) and FZP (red) with diameter = 25 μm , and incidence from substrate. Efficiencies corresponding to the different radii are labeled. This is the only case where the metalens outperforms the FZP in terms of efficiency.

1.10 Comparison of efficiencies as function of lens diameter.

We conducted a series of FDTD simulations to evaluate the performance of a Fresnel Zone Plate (FZP) and a metalens across a range of diameters—specifically 100 μm , 50 μm , and 25 μm utilizing glass substrates. The illumination originated from the substrate side in each case, with transverse electric (TE) polarization, while maintaining a constant numerical aperture (NA) of 0.98. This parametric consistency enabled a systematic investigation into the scaling effects of lens diameter on optical efficiency, with the primary objective of elucidating the comparative performance dynamics between the two optical systems. Our findings conclusively demonstrate that the FZP exhibits superior efficiency compared to the metalens across all tested diameters. The results are summarized in Figs S1.11-S1.12.

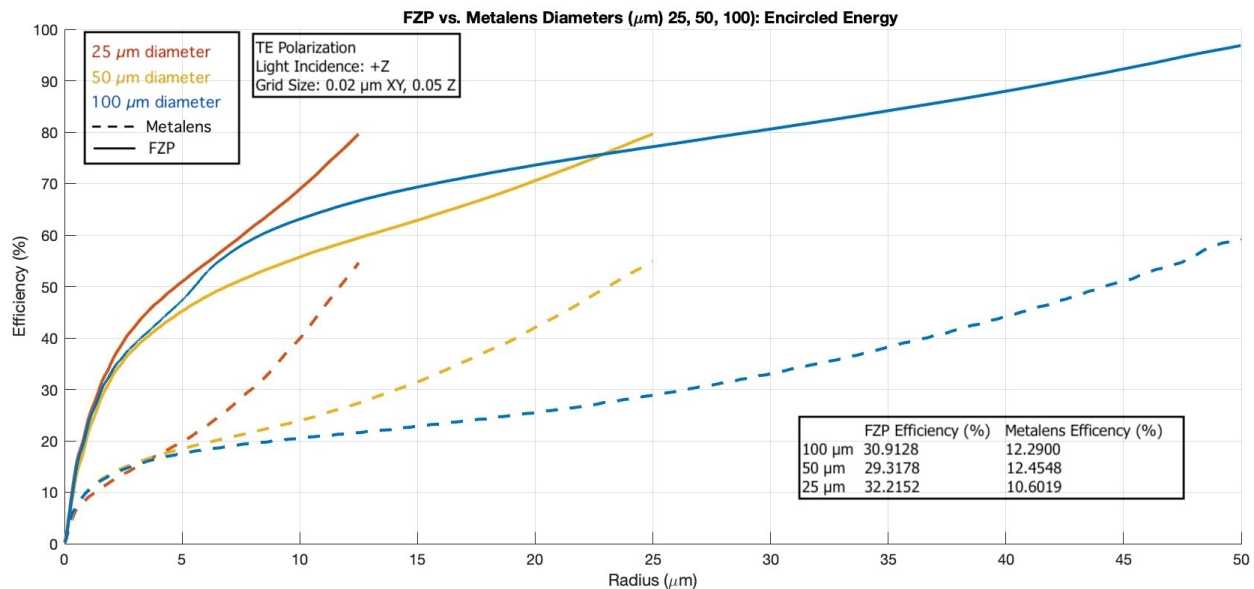


Fig S1.23: Simulated encircled power in the XY (focal) plane for the metalens and FZP with diameter = 100 μm , 50 μm and 25 μm . The inset tables summarize the efficiencies at 3 x FWHMx. In all cases, the FZP clearly outperforms the metalens at the corresponding diameter.

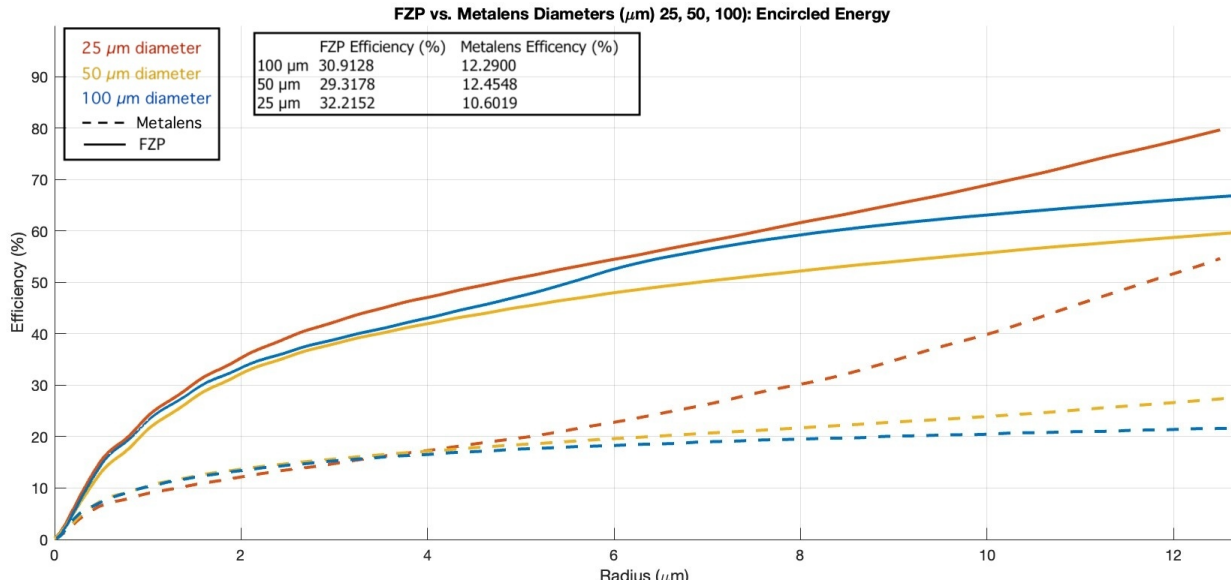


Fig S1.24: Magnified view close to the optical axis from Fig. S1.11.

1.11 Simulating Fabricable FZP with Ring-Width of 500 nm

Fabricating Fresnel Zone Plates (FZPs) with sub-0.1 nm features presents significant challenges, as the precision required strains current manufacturing capabilities and escalates costs. To explore a more practical design, we simulated an FZP with a 25 μm diameter, no substrate, and a ring width of 500 nm across 25 concentric rings.

We assessed the FZP's performance under incidence from both +Z and -Z directions, adopting parameters outlined in Sections 1.3, 1.4, and 1.5: a wavelength of 647 nm (TE polarization), grid size of 0.02 μm (X, Y) and 0.05 μm (Z), NA of 0.98, and focal distance of 2.5 μm . Compared to small feature size FZPs, which suffer from pronounced shadowing effects—particularly in the -Z direction from air—this 500 nm design demonstrated greater directional consistency. For -Z incidence, the FWHM measured 0.51917 μm (XZ) and 0.27955 μm (YZ), with efficiencies of 9.5015% at 3 \times FWHM (XZ) and 7.3272% at 1.5 \times FWHM (XZ). For +Z incidence, the FWHM was 0.55911 μm (XZ) and 0.27955 μm (YZ), with efficiencies of 10.2264% at 3 \times FWHM (XZ) and 7.3804% at 1.5 \times FWHM (XZ).

Despite this improved consistency, the larger feature size resulted in significantly lower overall focusing efficiency compared to small feature size FZPs, which benefit from sharper focusing when shadowing is mitigated. The 500 nm FZP thus represents a trade-off: while it underperforms in peak efficiency, its reduced shadowing and enhanced fabricability make it a compelling option for applications prioritizing manufacturability over optimal focusing. Efficiency calculations, detailed in Section 1.8, further elucidate this balance between practicality and performance.

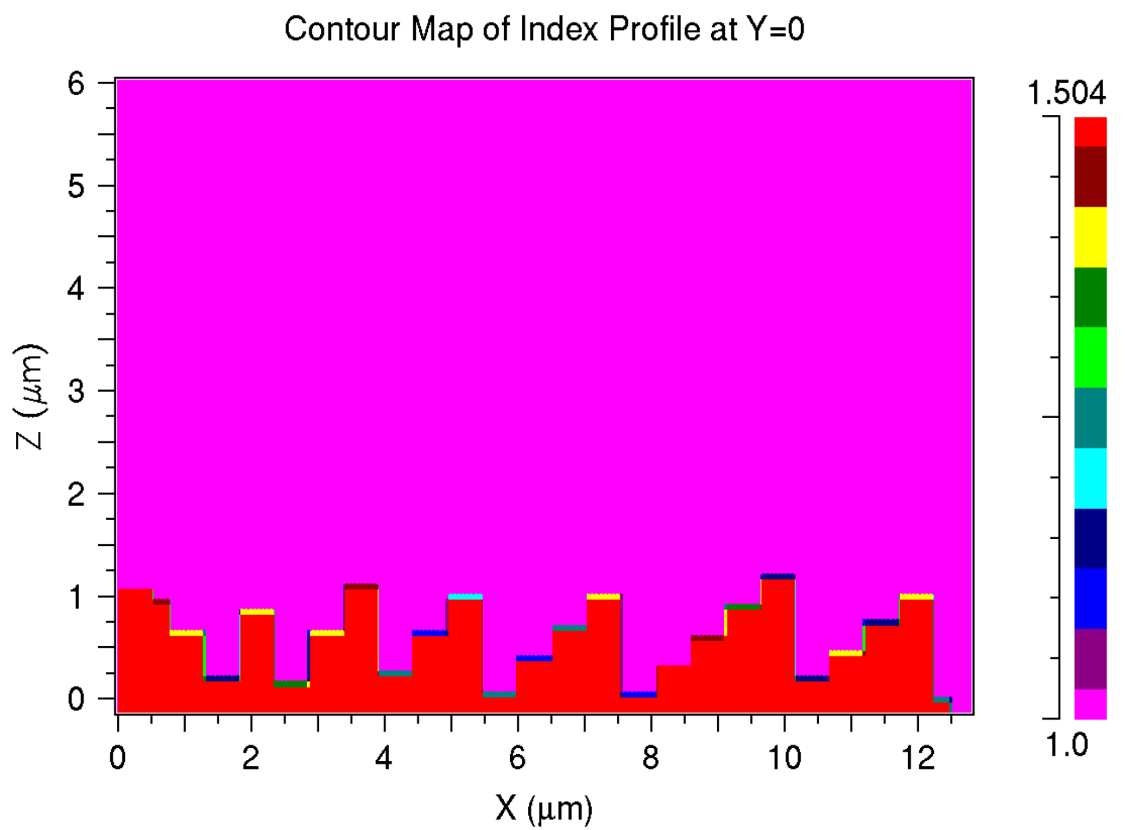


Fig S1.25: Material Profile of FZP with diameter = 25 μm , feature-size=0.5 μm , and focal length = 2.67 μm without substrate.

| FWHM (XZ) (μm) | | FWHM (YZ) (μm) | | Efficiency at FWHM*3 (XZ) (%) | | Efficiency at FWHM*1.5 (XZ) (%) | |
|-----------------------------|---------|-----------------------------|---------|-------------------------------|---------|---------------------------------|--------|
| +Z | -Z | +Z | -Z | +Z | -Z | +Z | -Z |
| 0.51917 | 0.55911 | 0.27955 | 0.27955 | 9.5015 | 10.2264 | 7.3272 | 7.3804 |

Table S1.26: Simulation results comparing incidence from air vs. substrate size of FZP with feature-size=500nm.

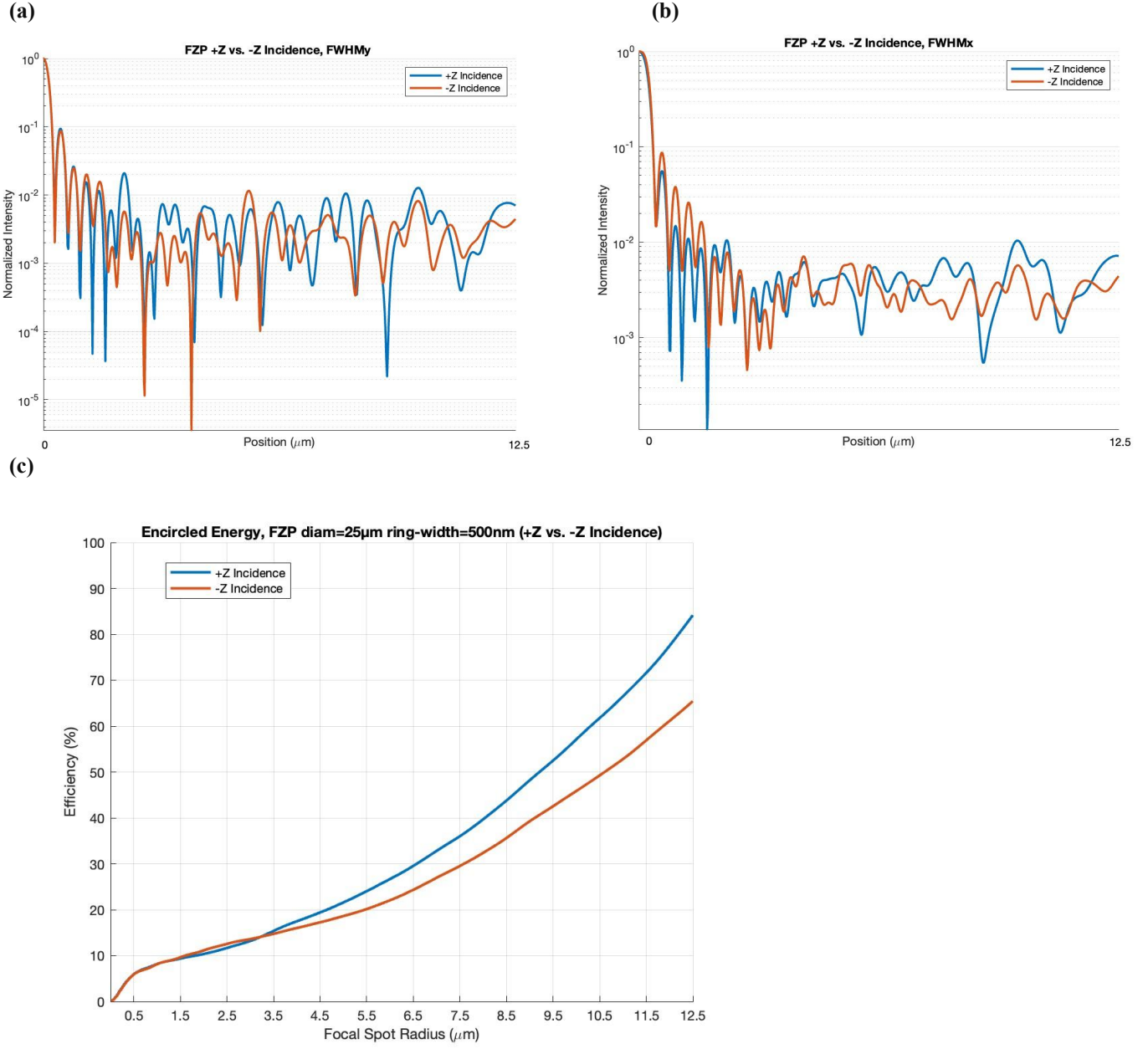


Fig S1.27: FZP Performance Metrics with ring-width=500nm. (a) FWHM in YZ plane comparing both incidence directions. (b) FWHM in XZ plane comparing both incidence directions. (c) Encircled energy comparing focusing efficiency in both incidence directions. For -Z incidence, the FWHM measured 0.51917 μm (XZ) and 0.27955 μm (YZ), with efficiencies of 9.5015% at 3 \times FWHM (XZ) and 7.3272% at 1.5 \times FWHM (XZ). For +Z incidence, the FWHM was 0.55911 μm (XZ) and 0.27955 μm (YZ), with efficiencies of 10.2264% at 3 \times FWHM (XZ) and 7.3804% at 1.5 \times FWHM (XZ).

2. Analysis of blazed gratings using finite element method (COMSOL Multiphysics)

We used the Wave Optics module of COMSOL Multiphysics [1] to simulate the performance of the prism type and the binary type diffraction gratings. The following sections elaborate the geometries created, convergence studies, and discusses the results in detail.

2.1. Simulation setup

COMSOL uses the finite element method (FEM) to solve for the electromagnetic fields in a given computational cell. The accuracy of the numerical solutions depends on the choice of the FEM mesh used to solve the given computational problem. We used the Wave Optics module and a Frequency Domain study to analyze the diffraction efficiency of the prism type and binary type blazed gratings. We used a Parametric Sweep to study the variation of the diffraction efficiencies with respect to the grating numerical aperture (NA) defined as the ratio of the wavelength of the incident light (λ) to the grating period (P). $NA = \frac{\lambda}{P}$. The height of the grating (gh) was chosen such that $gh = \frac{\lambda}{(n-1)}$, which, according to the thin-element approximation suggests a grating efficiency of 100% (ignoring Fresnel losses at interfaces). However, for large values of NA, or inversely, small values of period-to-wavelength ratio, the thin-element approximation and the scalar diffraction theory cease to be accurate. This necessitates the use of electromagnetic theories for accurate calculation of the diffraction efficiencies [2].

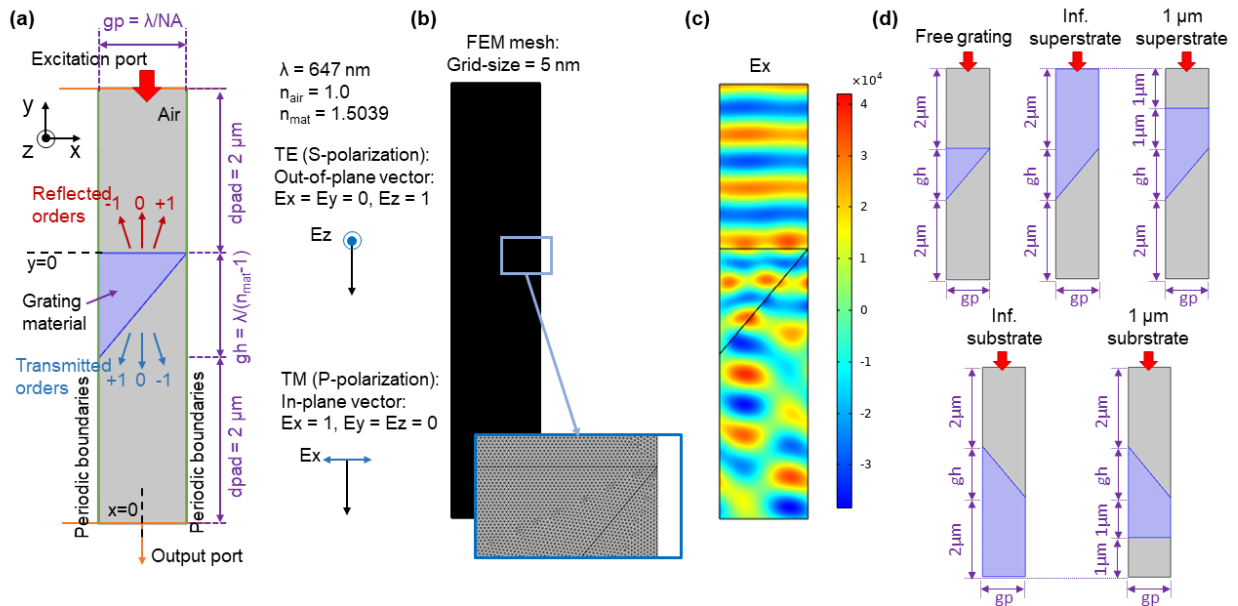


Fig. S2.1: Computation cell setup in COMSOL Wave Optics Module: (a) Computational cell showing the location of the input and output ports, periodic boundaries and the grating structure. All the typical dimensions used in the simulations are shown, along with the definitions of the TE and TM polarizations. (b) FEM mesh using a grid size of 5 nm per pixel with a magnified view inset. (c) Exemplary full-field solution for TM illumination and $NA = 0.6$. (d) The five structures studied: free grating, infinite superstrate, finite (1 μm) superstrate, infinite substrate and finite (1 μm) substrate, shown here for the prism-type blazed grating.

COMSOL Multiphysics uses the FEM approach to solve for full-fields and also uses monitors to calculate the powers diffracted into the various orders, given a grating of a certain geometry and material property at a particular optical frequency. The basic computational cell setup is shown in Fig. S2.1. We used the following definitions for TE (otherwise known as S-polarization) and TM (otherwise known as

P-polarization). For COMSOL, the grating geometry lies in the X-Y plane, is infinitely extended in the Z-axis and exhibits periodicity in the X-direction. The light travels in the -Y direction.

- TE: Electric field is perpendicular to the plane of the grating. Field excited in the simulation = Ez only
- TM: Electric field is parallel to the plane of the grating. Field excited in the simulation = Ex only

Fig. S2.1 (a) shows a typical computational cell constructed in the COMSOL Wave Optics simulation module. Without loss of generality, we chose the simulation wavelength (λ) equal to 647 nm and the corresponding material refractive index of 1.5039 [3]. Fig. S2.1(b) and (c) show the FEM mesh of 5 nm grid size used for the study and an exemplary full-field simulation result for TM (Ex) illumination, respectively. We studied five structures as shown in Fig. S2.1(d): free grating, with air in front and behind the grating, infinite superstrate (thick layer of the grating material under the grating and the light is incident from the back of the grating, through this material), finite superstrate (1 μm thick grating material behind the grating with light incident from air, behind this material layer), infinite substrate (same as the superstrate case, but the light is incident from air, atop the grating) and finite substrate (same as the finite superstrate case, but the light is incident from air, atop the grating). We note that as shown in Fig. S2.2, the infinite superstrate case may be the most practical scenario for demonstrating and measuring the grating performance in experiment with the transmission grating being illuminated from behind with the detector located in air.

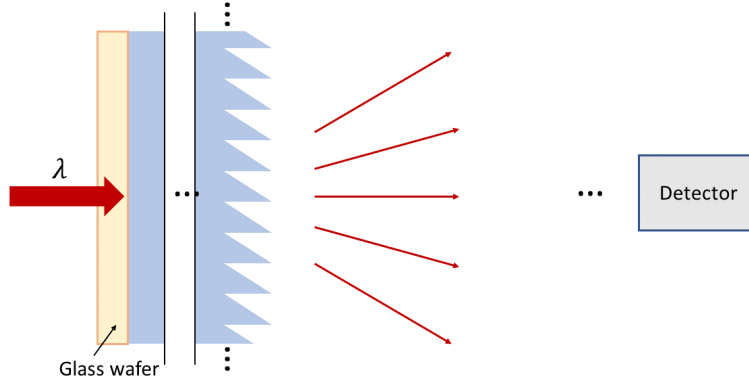


Fig. S2.2: Schematic diagram showing practical use case of the “infinite superstrate” type grating structure.

Following are the details of the model created in COMSOL to perform the simulations:

- Parameters: The simulation parameters are listed in Table S2.1.
- Materials: We defined two materials: air (refractive index = $n_{\text{air}} = 1$) and the grating material (refractive index = $n_{\text{mat}} = 1.5039$).
- Geometry: We created the geometry as per the structure being simulated (prism-type blazed grating or binary-type blazed grating of 3 or 5 cells). See Fig. S2.3 for the dimensions of the binary blazed gratings.
- Electromagnetic Waves Frequency Domain (ewfd): Electric field component solved for: Out-of-plane vector, Formulation: Full field. We added an input or excitation port at the top boundary of the computational cell and an output port at the bottom boundary. The waves propagate downward, i.e. -Y direction. Increases in diffraction order correspond to clockwise rotations of both the reflected and transmitted wave vectors on either side of the unit cell, as shown in Fig. S2.1. Thus, higher reflected orders point more to the right, while higher transmitted orders point more to the left. Port boundary conditions are used to release the incident wave and to absorb the reflected and transmitted waves of order 0. To ensure that no unphysical reflections occur, Diffraction Order subnodes were added to the

Port nodes to absorb outgoing waves of each nonzero diffraction order. The input to each periodic port is an electric field amplitude vector and an angle of incidence.

- ewfd setting for TE: Port 1 (excitation): Boundary selection: Top boundary of computational cell as shown in Fig. S2.1. Type of port: Periodic, Wave excitation at this port: On, Port input power = 1W, Input quantity: Electric field Ex = Ey = 0, Ez = 1, Angle of incidence = alpha, Refractive index real part: Set to either n_air or n_mat depending on the type of simulation.
- ewfd setting for TM: Port 1 (excitation): Boundary selection: Top boundary of computational cell as shown in Fig. S2.1. Type of port: Periodic, Wave excitation at this port: On, Port input power = 1W, Input quantity: Electric field Ex = 1, Ey = Ez = 0, Angle of incidence = alpha, Refractive index real part: Set to either n_air or n_mat depending on the type of simulation.
- ewfd setting for TE: Port 2 (output): Boundary selection: Bottom boundary of computational cell as shown in Fig. S2.1. Type of port: Periodic, Wave excitation at this port: Off, Port input power = 1W, Input quantity: Electric field Ex = Ey = 0, Ez = 1, Refractive index real part: Set to either n_air or n_mat depending on the type of simulation. Include in automatic diffraction order calculation: Enabled.
- ewfd setting for TM: Port 2 (output): Boundary selection: Bottom boundary of computational cell as shown in Fig. S2.1. Type of port: Periodic, Wave excitation at this port: Off, Port input power = 1W, Input quantity: Electric field Ex = 1, Ey = Ez = 0, Refractive index real part: Set to either n_air or n_mat depending on the type of simulation. Include in automatic diffraction order calculation: Enabled.
- Two diffraction order subnodes were added manually to the input port with the following settings: Components: Out-of-plane vector for TE, or In-plane vector for TM, Diffraction order m = -1 and m = 1.
- Diffraction order subnodes for the output port were added automatically by clicking “Add diffraction orders” in the input port.
- Mesh: Mesh was constructed with Sequence type: User-controlled mesh and for Size settings, Maximum element size = Minimum element size = res.
- Study: We added a Frequency Domain study for Frequencies = f0 and a Parametric sweep for the Parameter NA over the range 0.6:0.005:0.995.

Table S2.1: List of simulation parameters used in COMSOL modelling

| Parameter | Expression | Value | Description |
|-----------|----------------|---------------|--------------------------------------|
| n_air | 1 | 1 | Refractive index of air |
| n_mat | 1.5039 | 1.5039 | Refractive index of grating material |
| lam0 | 647[nm] | 6.47E-7 m | Simulation wavelength |
| f0 | c const/lam0 | 4.6336E14 1/s | Frequency |
| alpha | 0.0[deg] | 0 rad | Angle of incidence |
| gh | lam0/(n_mat-1) | 1.284E-6 m | Grating height |
| NA | 0.6 | 0.6 | Numerical aperture |
| gp | lam0/NA | 1.0783E-6 m | Grating period |
| dpad | 2[um] | 2E-6 m | Padding depths |
| res | 5[nm] | 5E-9 m | Resolution |

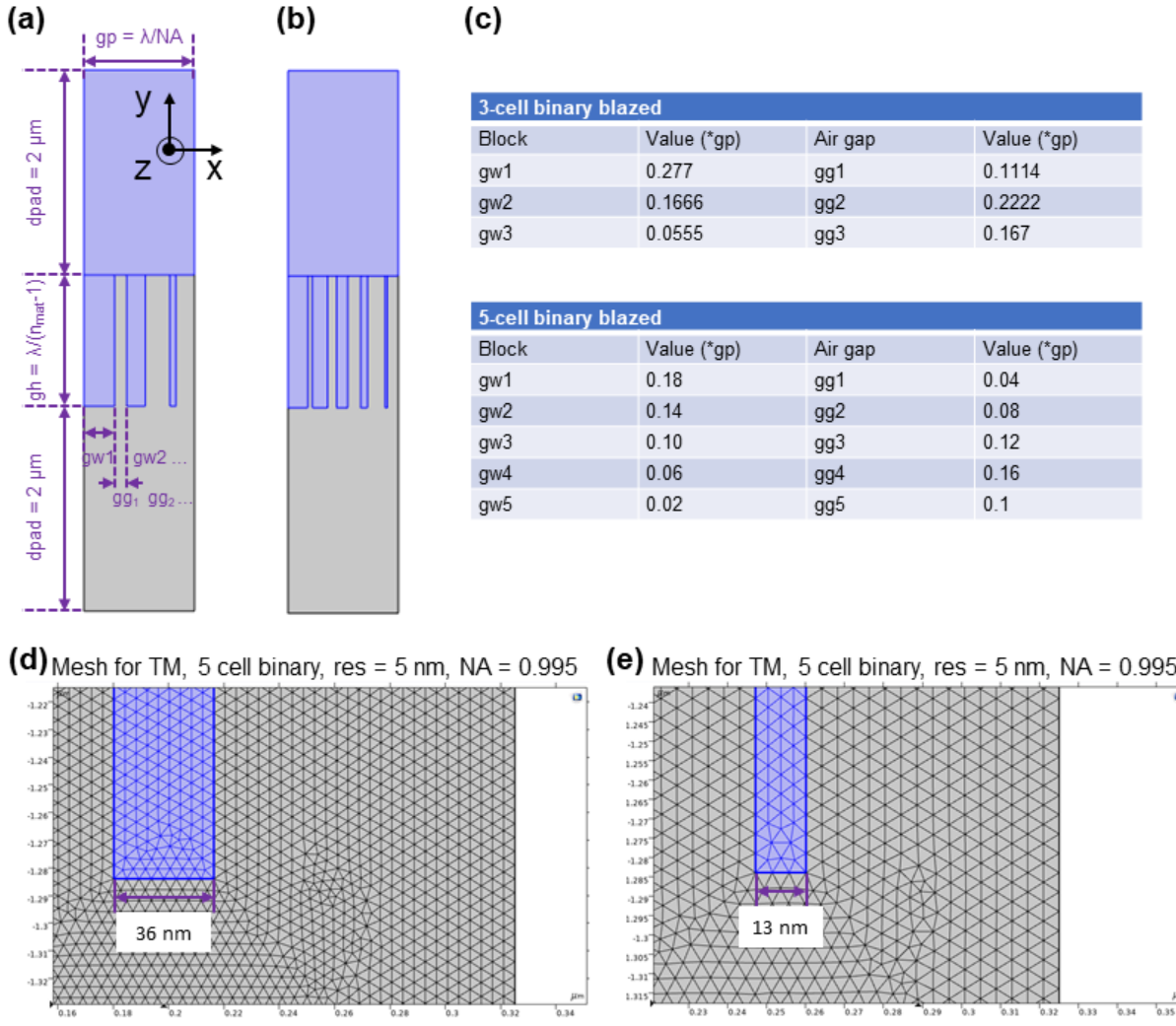


Fig. S2.3: Schematic diagram showing the (a) 3-cell and (b) 5-cell binary blazed gratings along with the values of the grating sub-pillar width (gw_n) and grating sub-pillar gap (gg_n).

2.2. Convergence study

In order to ensure proper convergence of the FEM numerical solutions, we tested different mesh settings. The results achieve convergence when there is no change in the results with increasing the resolution of the FEM grid, i.e. making the FEM mesh finer. We observed that convergence is achieved for a FEM mesh grid resolution of 5 nm. Fig. S2.4 shows the meshing for the computational cell region for the TE illumination case for two values of NA, 0.6 and 0.995 at 5 and 2.5 nm grid size. The corresponding simulation results of all the diffraction orders versus NA, for the two cases are shown in Fig. S2.5 (a-b) with the first order transmission diffraction efficiency (defined as the ratio of the power diffracted into the first transmitted order to the total transmitted power in percentage) is plotted in Fig. S2.5 (c) and the light intensity in the computational cell for three values of NA, 0.6, 0.75 and 0.995 for the two grid sizes 5 and 2.5 nm, shown in Fig. S2.5 (d) and (e) respectively. We observed no change in the results from decreasing the grid size from 5 to 2.5 nm and thus concluded that 5 nm is sufficient for achieving accurate results. It may be noted that the model with 2.5 nm mesh grid size consumes about 4 times the memory requirement compared to the model with 5 nm mesh grid size (15.5 GB vs 3.75 GB)

and takes almost 2.5 times longer to compute (~ 1.25 hrs vs ~ 2.75 hrs) and thus, using the 5 nm grid size was computationally efficient while ensuring the accuracy of the results.

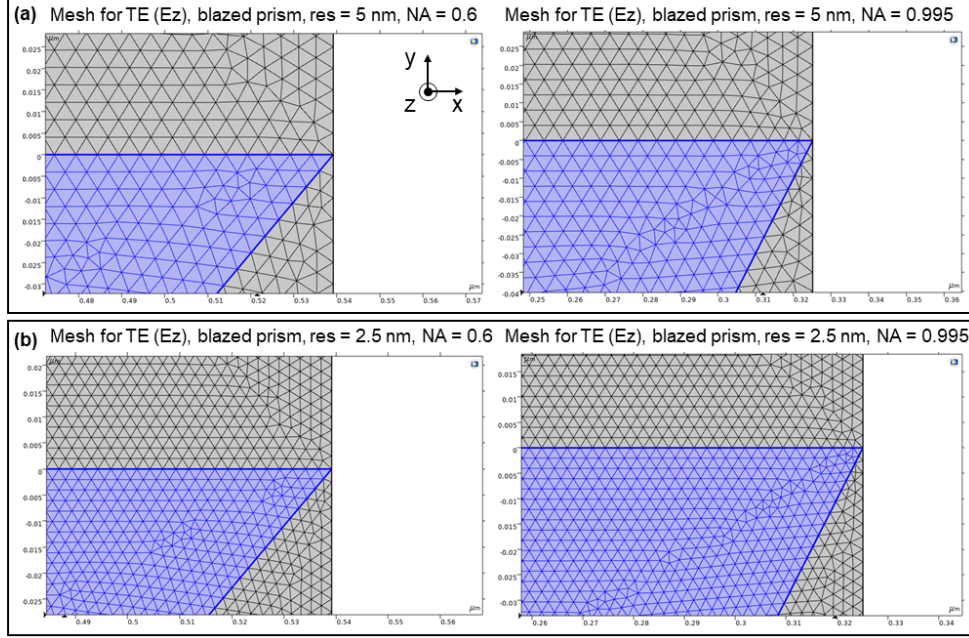


Fig. S2.4: FEM mesh for TE illumination for NA = 0.6 and 0.995 with (a) 5 nm and (b) 2.5 nm mesh grid size.

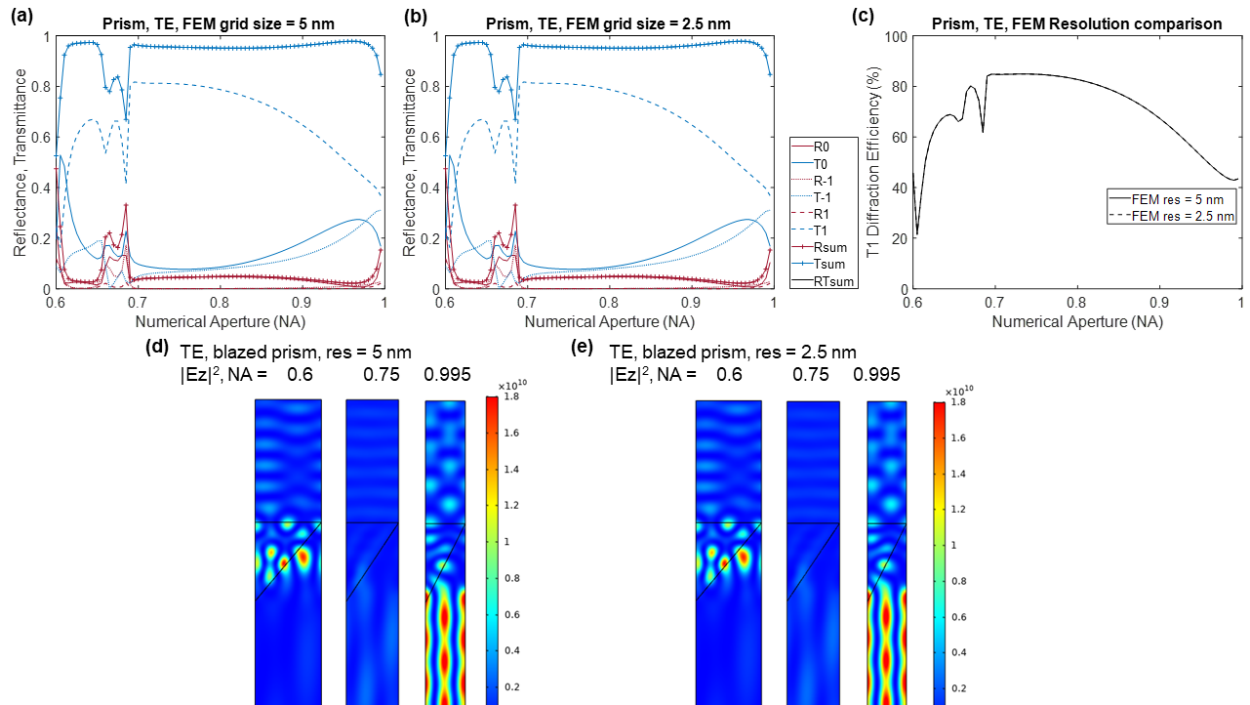


Fig. S2.5: Results of convergence study for TE illumination. All diffraction orders vs NA for (a) FEM mesh grid size = 5 nm and (b) FEM mesh grid size = 2.5 nm. (c) First-order transmission diffraction efficiency extracted from (a) and (b) vs NA, compared for FEM mesh grid sizes 5 and 2.5 nm showing good match. (d-e) Light intensity distribution in the computational cell for NA = 0.6, 0.75 and 0.995 for FEM mesh grid sizes 5 and 2.5 nm showing good match.

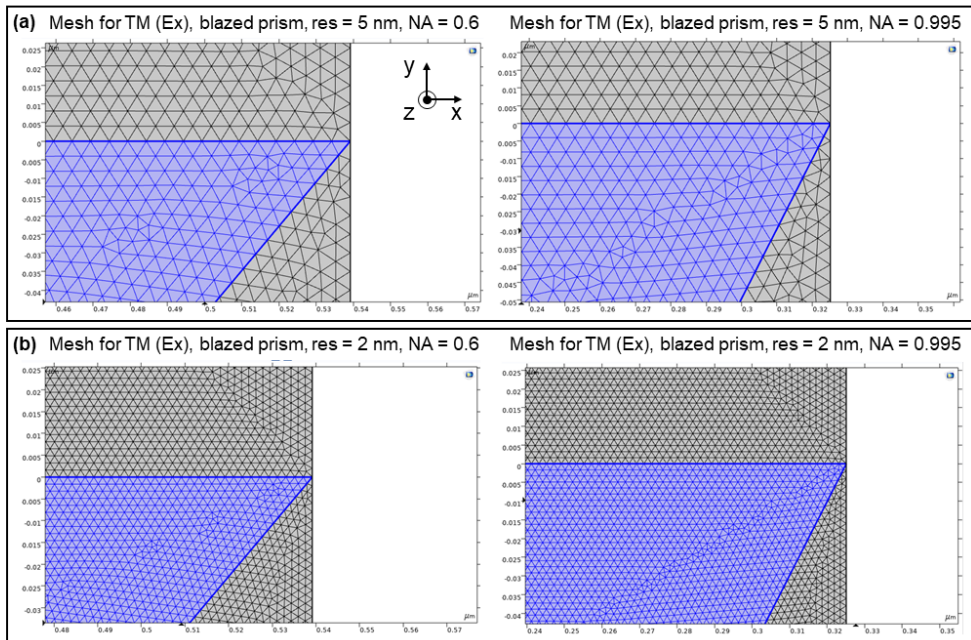


Fig. S2.6: FEM mesh for TM illumination for NA = 0.6 and 0.995 with (a) 5 nm and (b) 2.5 nm mesh grid size.

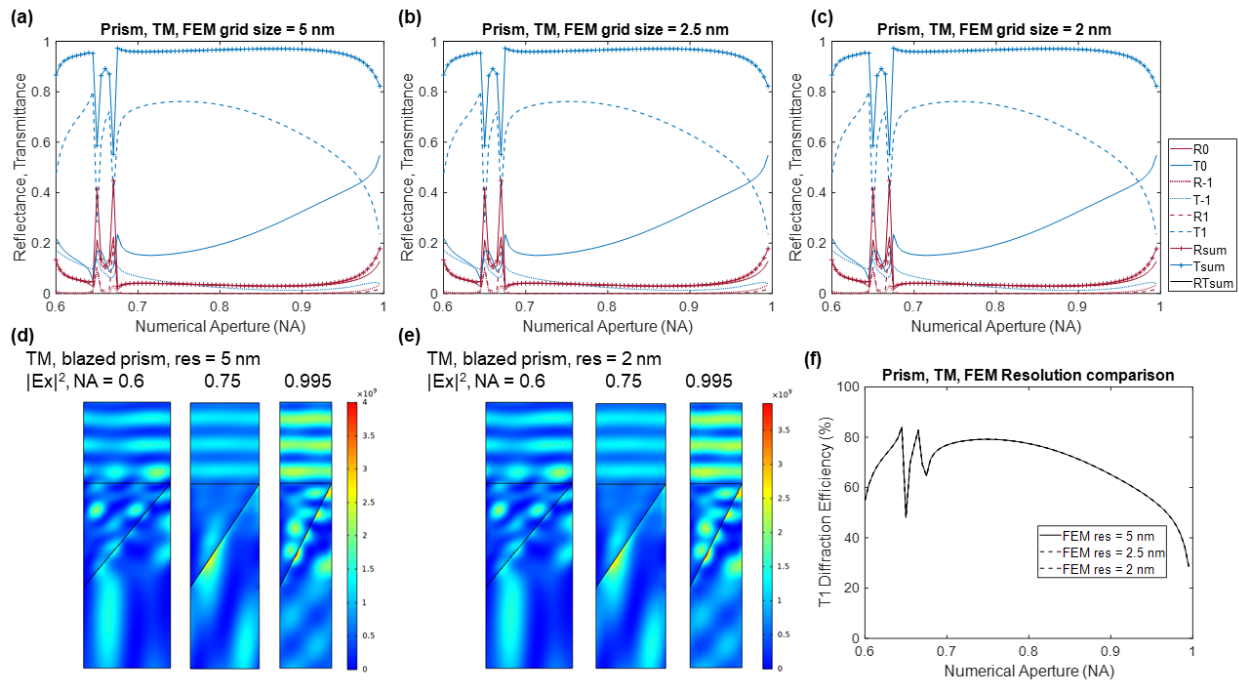


Fig. S2.7: Results of convergence study for TM illumination. All diffraction orders vs NA for (a) FEM mesh grid size = 5 nm and (b) FEM mesh grid size = 2.5 nm, and (c) 2 nm. (d-e) Light intensity distribution in the computational cell for NA = 0.6, 0.75 and 0.995 for FEM mesh grid sizes 5 and 2 nm showing good match. (f) First-order transmission diffraction efficiency extracted from (a-c) vs NA, compared for FEM mesh grid sizes 5, 2.5, and 2 nm showing good match.

We performed the same convergence study for TM illumination as well, and tested different mesh settings. We observed that convergence is achieved for a FEM mesh grid resolution of 5 nm in the TM

illumination case as well. Fig. S2.6 shows the meshing for the computational cell region for the TM illumination case for two values of NA, 0.6 and 0.995 at 5 and 2 nm grid size. The corresponding simulation results of all the diffraction orders versus NA, for grid sizes equal to 5, 2.5, and 2 nm cases are shown in Fig. S2.7 (a-c) with the light intensity in the computational cell for three values of NA, 0.6, 0.75 and 0.995 shown in Fig. S2.7 (d) and (e) respectively, and the first order transmission diffraction efficiency plotted in Fig. S2.7 (f). We observed no change in the results from decreasing the grid size from 5 to 2 nm and thus concluded that 5 nm is sufficient for achieving accurate results.

2.3. Simulation results for prism type blazed grating

The simulation results for the prism-type blazed grating for TE and TM illumination are shown in Fig. S2.8 and S2.9, respectively. In each case, we show the full transmission and diffraction orders vs NA for the 5 cases: (a) free grating, (b) infinite superstrate, (c) finite superstrate, (d) infinite substrate, and (e) finite substrate cases. Finally, we calculated the first-order transmission diffraction efficiency for the 5 cases, extracting data from (a-e), and defining this as the ratio of the power diffracted into the first transmitted order to the total transmitted power in percentage. The value of the first-order transmission diffraction efficiency vs NA is shown in panel (f) in Fig. S2.8 and S2.9.

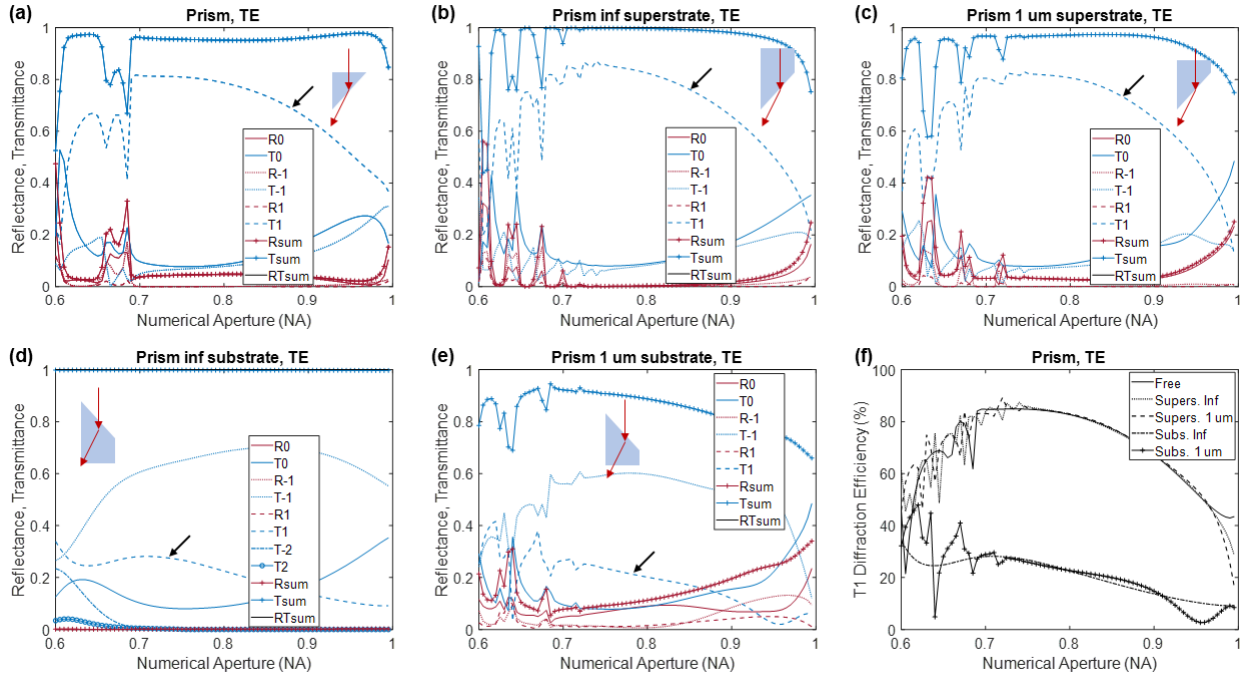


Fig. S2.8: Simulation results for TE illumination showing all transmission and diffraction orders vs NA for prism-type blazed grating for (a) free grating, (b) infinite superstrate, (c) finite superstrate, (d) infinite substrate, and (e) finite substrate cases. The first transmitted order is pointed out by the black arrow. (f) First-order transmission diffraction efficiency for the 5 cases, extracted from (a-e).

The steady-state light intensity inside the computational cell for three values of NA, 0.6, 0.75 and 0.995, for the infinite superstrate case are shown for the TE and TM illumination cases in Fig. S2.10 (a) and (b), respectively.

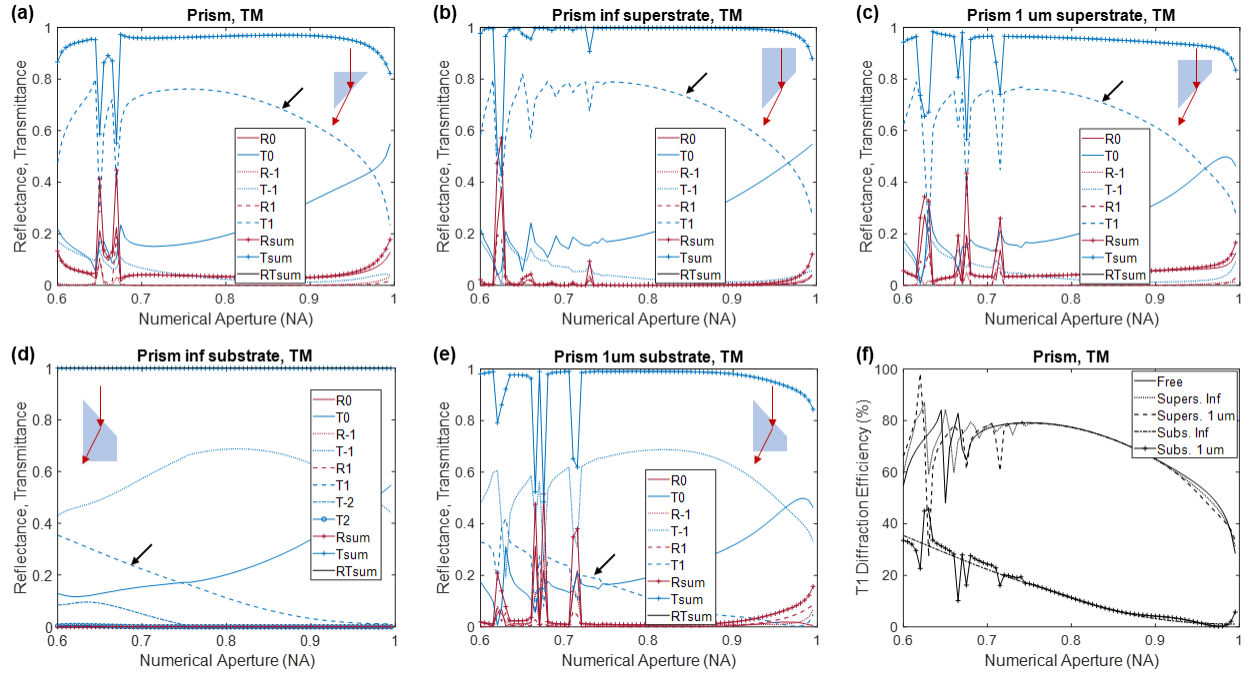


Fig. S2.9: Simulation results for TM illumination showing all transmission and diffraction orders vs NA for prism-type blazed grating for (a) free grating, (b) infinite superstrate, (c) finite superstrate, (d) infinite substrate, and (e) finite substrate cases. The first transmitted order is pointed out by the black arrow. (f) First-order transmission diffraction efficiency for the 5 cases, extracted from (a-e).

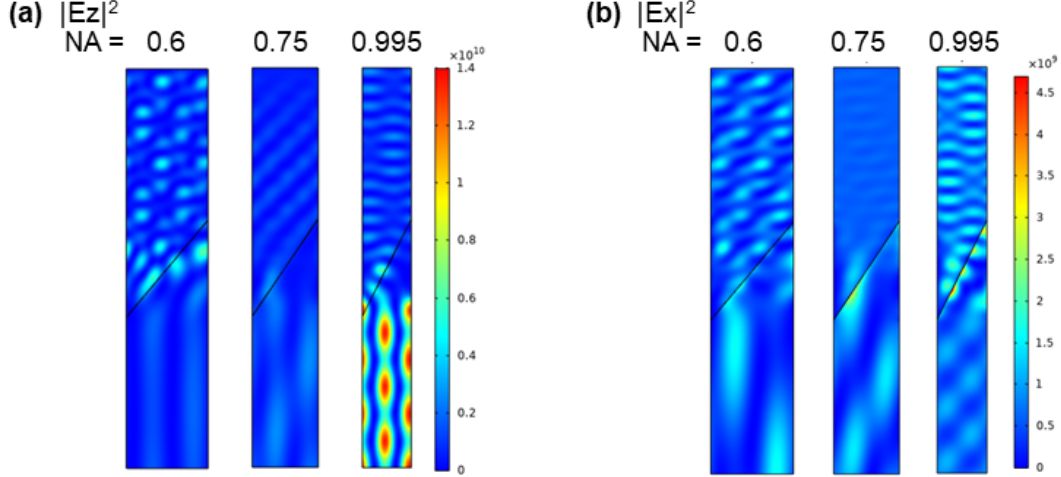


Fig. S2.10: Steady-state light intensity inside the computational cell for three values of NA, 0.6, 0.75 and 0.995, for the infinite superstrate case are shown for (a) TE and (b) TM illuminations.

2.4. Simulation results for 3-cell binary blazed grating

The simulation results for the 3-cell binary blazed grating for TE and TM illumination are shown in Fig. S2.11 and S2.12, respectively. In each case, we show the full transmission and diffraction orders vs NA for the 5 cases: (a) free grating, (b) infinite superstrate, (c) finite superstrate, (d) infinite substrate, and (e) finite substrate cases. The value of the first-order transmission diffraction efficiency (calculated in the same way as described in Section 2.3) vs NA is shown in panel (f) in Fig. S2.11 and S2.12.

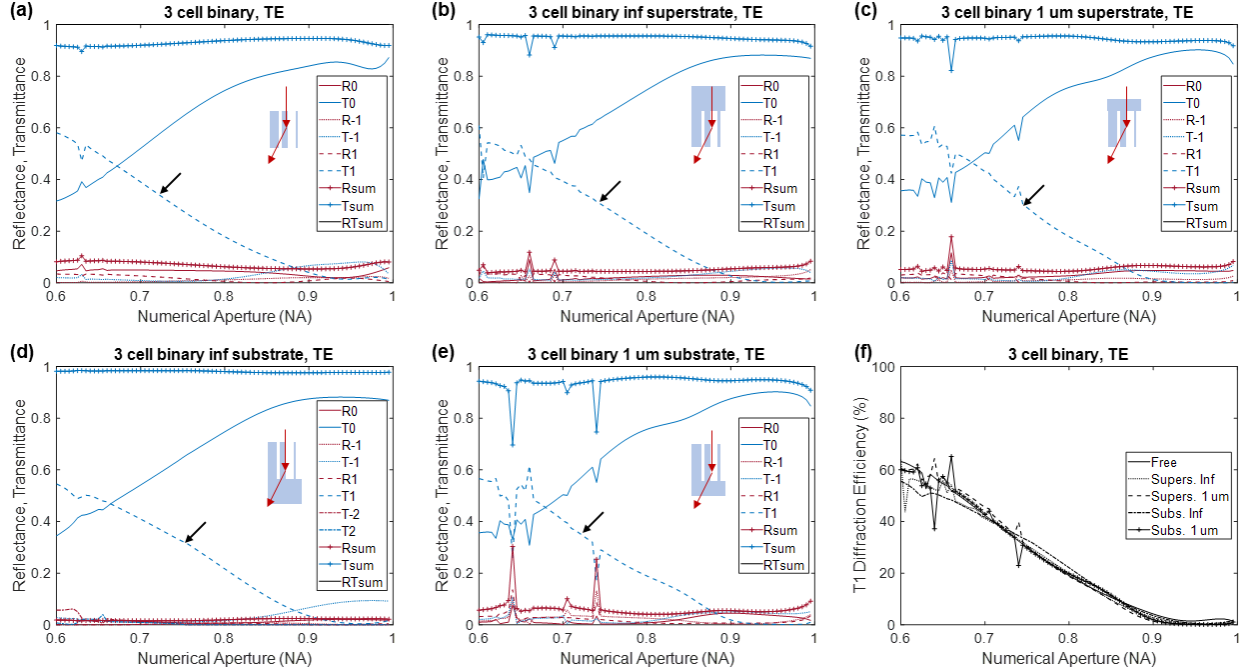


Fig. S2.11: Simulation results for TE illumination showing all transmission and diffraction orders vs NA for 3-cell binary blazed grating for (a) free grating, (b) infinite superstrate, (c) finite superstrate, (d) infinite substrate, and (e) finite substrate cases. The first transmitted order is pointed out by the black arrow. (f) First-order transmission diffraction efficiency for the 5 cases, extracted from (a-e).

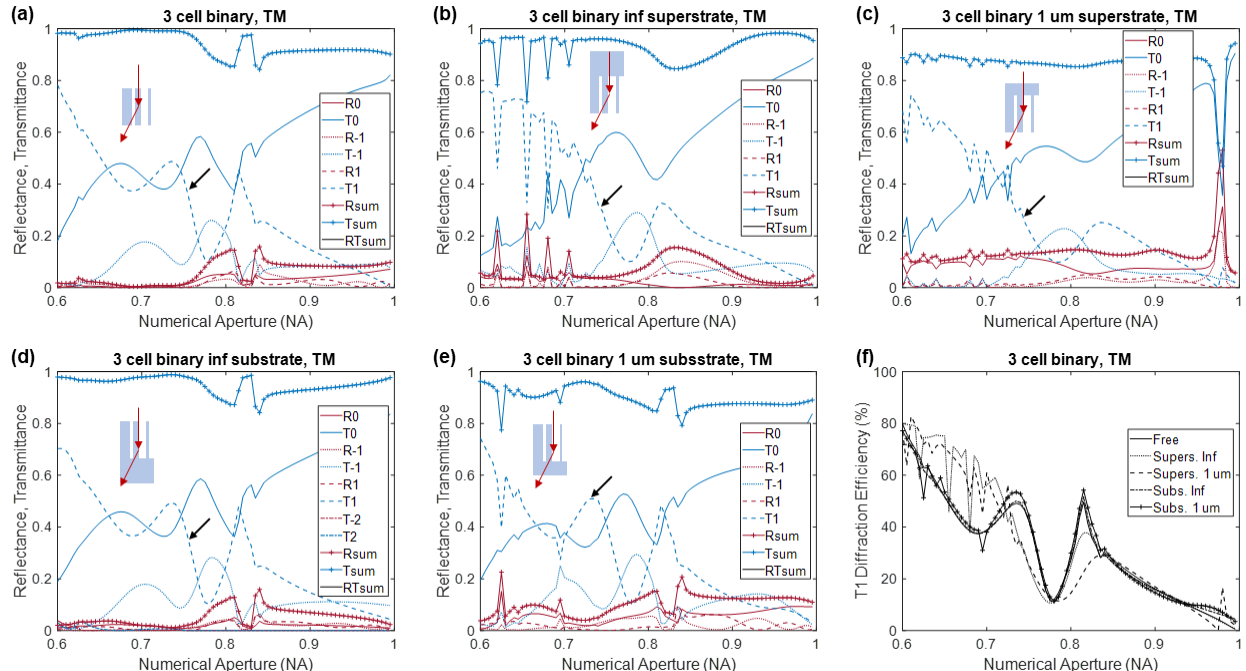


Fig. S2.12: Simulation results for TM illumination showing all transmission and diffraction orders vs NA for 3-cell binary blazed grating for (a) free grating, (b) infinite superstrate, (c) finite superstrate, (d) infinite substrate, and (e) finite substrate cases. The first transmitted order is pointed out by the black arrow. (f) First-order transmission diffraction efficiency for the 5 cases, extracted from (a-e).

The steady-state light intensity inside the computational cell for three values of NA, 0.6, 0.75 and 0.995, for the infinite superstrate case are shown for the TE and TM illumination cases in Fig. S2.13 (a) and (b), respectively.

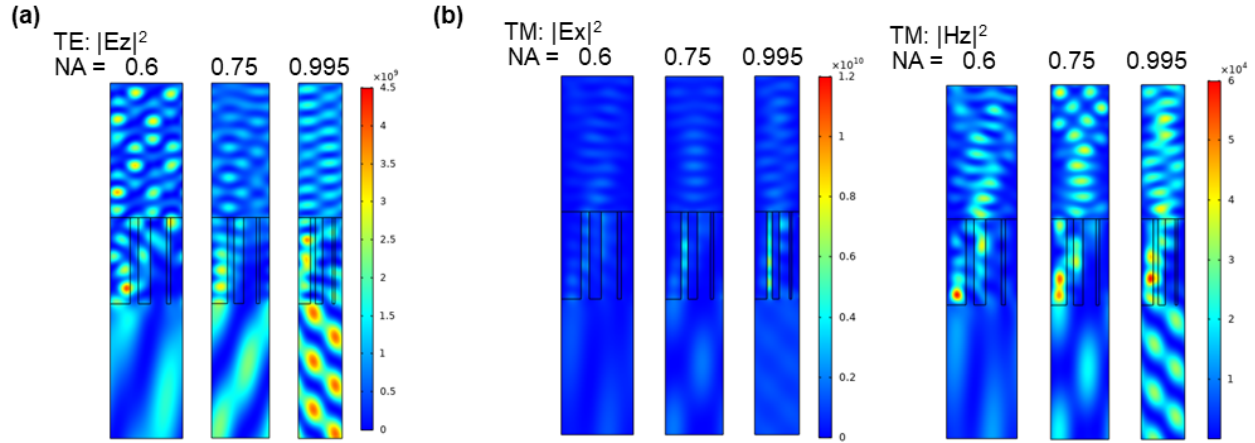


Fig. S2.13: Steady-state light intensity inside the computational cell for the infinite superstrate case for three values of NA, 0.6, 0.75 and 0.995, for the infinite superstrate case are shown for (a) TE ($|E_z|^2$) and (b) TM ($|E_x|^2$ and $|H_z|^2$) illuminations.

2.5. Simulation results for 5-cell binary blazed grating

The simulation results for the 5-cell binary blazed grating for TE and TM illumination are shown in Fig. S2.14 and S2.15, respectively. In each case, we show the full transmission and diffraction orders vs NA for the 5 cases: (a) free grating, (b) infinite superstrate, (c) finite superstrate, (d) infinite substrate, and (e) finite substrate cases. The value of the first-order transmission diffraction efficiency (calculated in the same way as described in Section 2.3) vs NA is shown in panel (f) in Fig. S2.14 and S2.15.

The steady-state light intensity inside the computational cell for three values of NA, 0.6, 0.75 and 0.995, for the infinite superstrate case are shown for the TE and TM illumination cases in Fig. S2.16 (a) and (b), respectively.

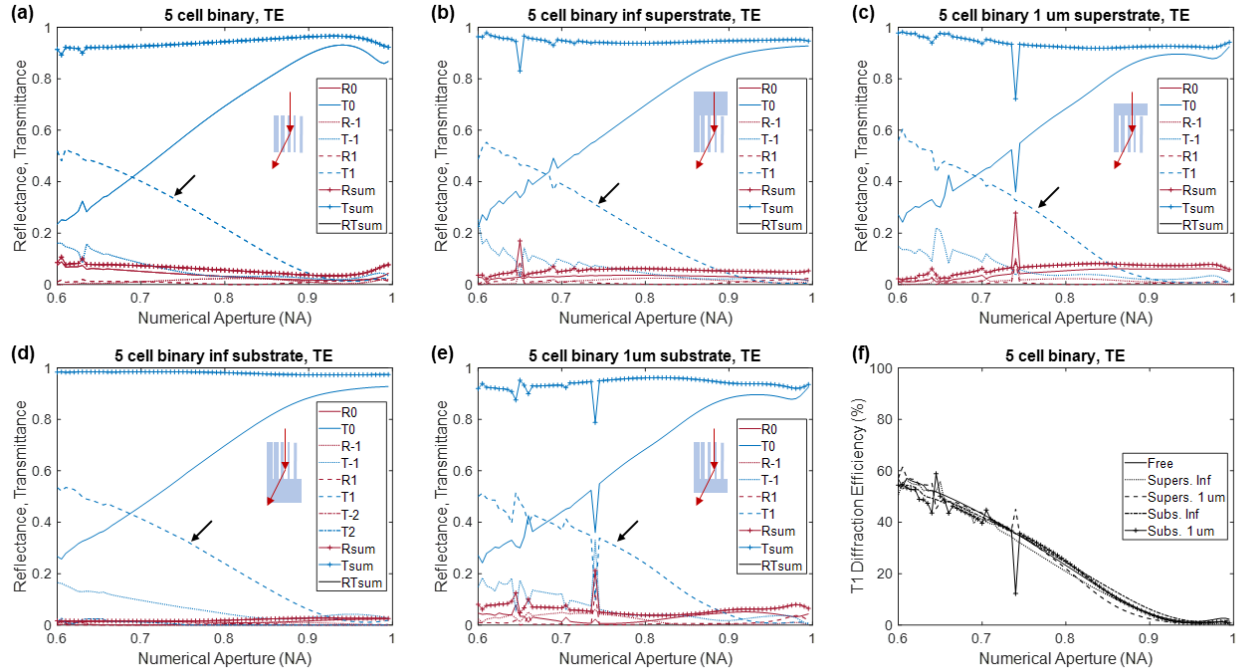


Fig. S2.14: Simulation results for TE illumination showing all transmission and diffraction orders vs NA for 5-cell binary blazed grating for (a) free grating, (b) infinite superstrate, (c) finite superstrate, (d) infinite substrate, and (e) finite substrate cases. The first transmitted order is pointed out by the black arrow. (f) First-order transmission diffraction efficiency for the 5 cases, extracted from (a-e).

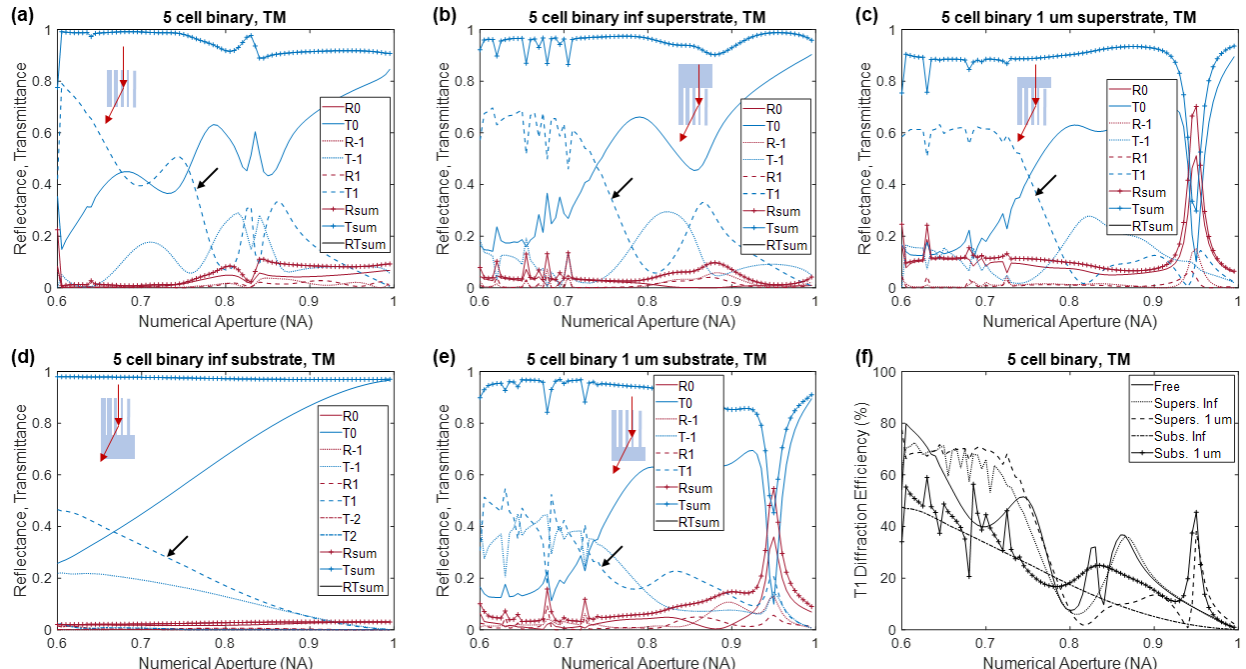


Fig. S2.15: Simulation results for TM illumination showing all transmission and diffraction orders vs NA for 5-cell binary blazed grating for (a) free grating, (b) infinite superstrate, (c) finite superstrate, (d) infinite substrate, and (e) finite substrate cases. The first transmitted order is pointed out by the black arrow. (f) First-order transmission diffraction efficiency for the 5 cases, extracted from (a-e).

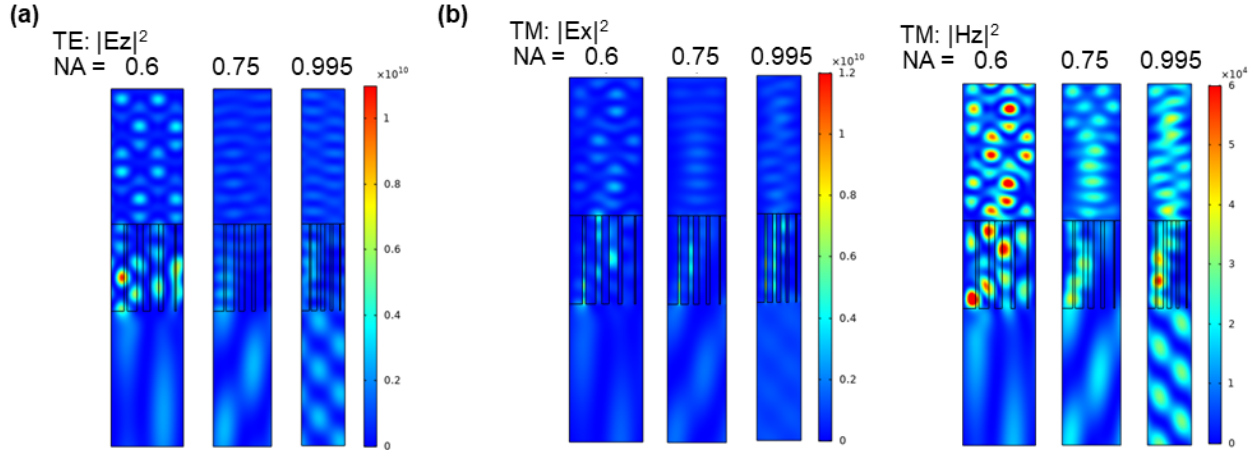


Fig. S2.16: Steady-state light intensity inside the computational cell for the infinite superstrate case for three values of NA, 0.6, 0.75 and 0.995, for the infinite superstrate case are shown for (a) TE ($|E_z|^2$) and (b) TM ($|E_x|^2$ and ($|H_z|^2$) illuminations.

We show the first order transmission diffraction efficiency for the infinite superstrate and substrate cases in Fig. S2.17. This data is extracted from panel (f) of Fig. S2.8, Fig. S2.9, Fig. S2.11, Fig. S2.12, Fig. S2.14, and Fig. S2.15.

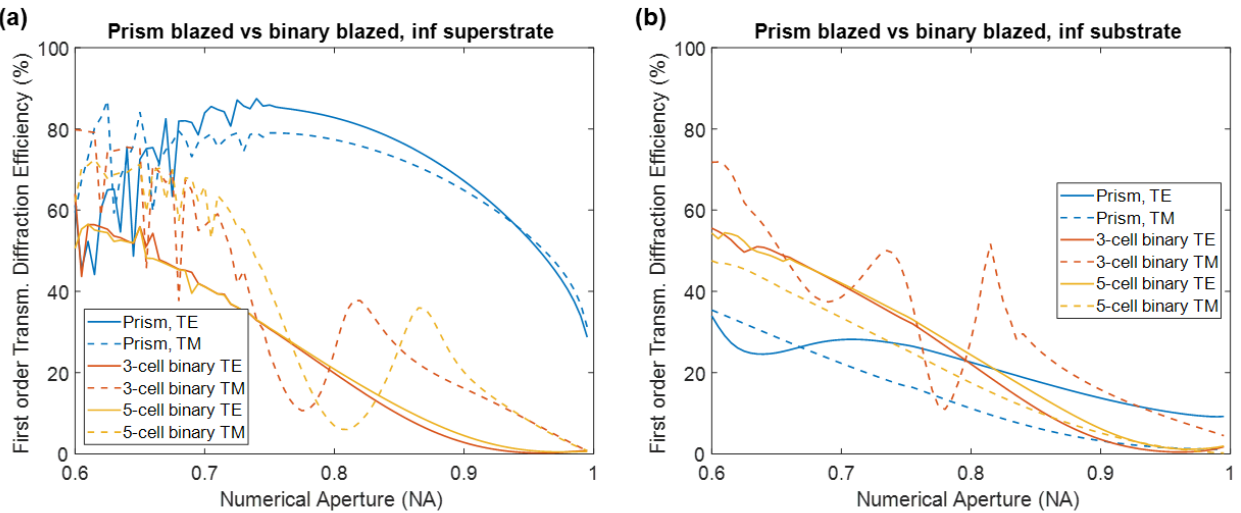


Fig. S2.17: First order transmission diffraction efficiency for the (a) infinite superstrate and (b) infinite substrate cases.

3. Analysis of blazed gratings using RCWA (RSoft DiffractMOD)

We also used the DiffractMOD feature of RSoft RCWA simulation software [4] to simulate the performance of the prism type and the binary type diffraction gratings. The following sections elaborate the geometries created, convergence studies, and discusses the results in detail.

3.1. Simulation setup

RSoft DiffractMOD uses the rigorous coupled-wave analysis (RCWA) to solve for the electromagnetic fields in a given computational cell and calculate the diffraction efficiencies of the transmitted and reflected orders. The accuracy of the numerical solutions depends on the choice of the grid size used to

solve the given computational problem. In addition to single simulations, we also used RSoft's Multi-Variable Optimization and Scanning Tool (MOST) to run a parametric sweep to study the variation of the diffraction efficiencies with respect to the grating numerical aperture (NA). As in the previous section, the height of the grating (gh) was chosen such that $gh = \frac{\lambda}{(n-1)}$ and $NA = \frac{\lambda}{P}$, where λ is the wavelength of the incident light, and P is the grating period.

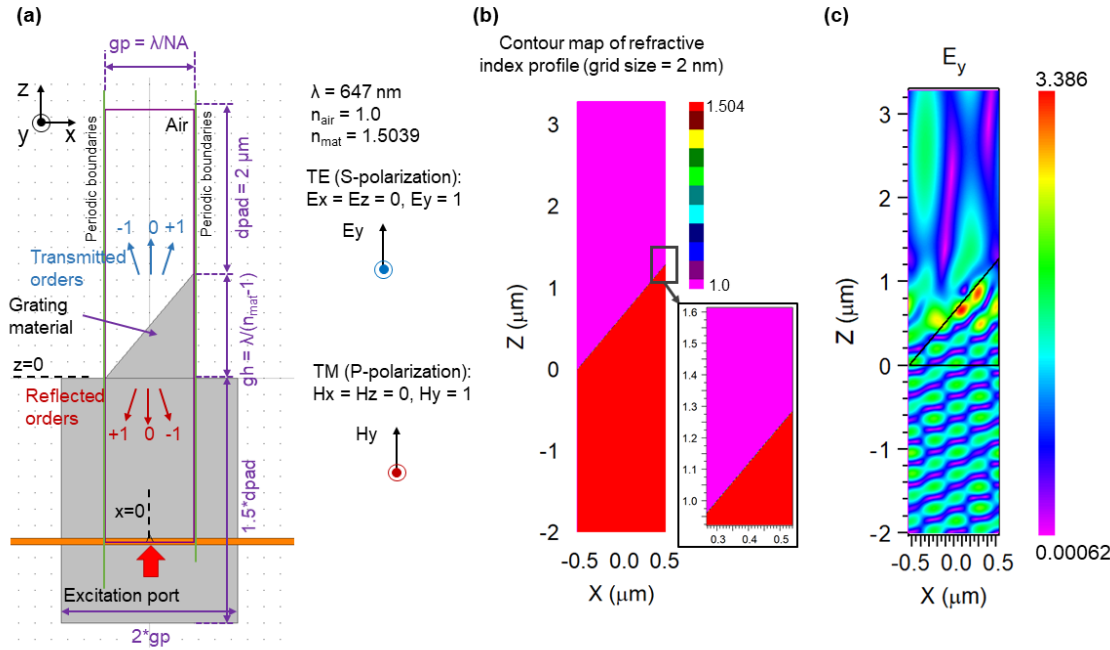


Fig. S3.1: Computation cell setup in RSoft DiffractMOD: (a) Computational cell (bound by purple box) showing the location of the source (excitation port), periodic boundaries and the grating structure. All the typical dimensions used in the simulations are shown, along with the definitions of the TE and TM polarizations. (b) Refractive index distribution with grid size = 2 nm per pixel with a magnified view inset. (c) Exemplary full-field solution for TE illumination and NA = 0.6.

RSoft uses a different co-ordinate system compared to COMSOL (Section 2) and the computational cell for RSoft is shown in Fig. S3.1. We used the following definitions for TE (otherwise known as S-polarization) and TM (otherwise known as P-polarization). For RSoft, the grating geometry lies in the X-Z plane, is infinitely extended in the Y-axis and exhibits periodicity in the X-direction. The light travels in the +Z direction.

- TE: Electric field is perpendicular to the plane of the grating. Field excited in the simulation = E_y only
- TM: Magnetic field is perpendicular to the plane of the grating. Field excited in the simulation = H_y only

Similar to Section 2, we chose the simulation wavelength (λ) equal to 647 nm and the corresponding material refractive index of 1.5039 [3]. Fig. S3.1(b) and (c) show the refractive index distribution in the computational cell with a grid size of 2 nm, and an exemplary full-field simulation result for TE (E_y) illumination. We studied the same five structures as described in Section 2: free grating, infinite superstrate, finite superstrate, infinite substrate, and finite substrate.

Following are the details of the model created in RSoft DiffractMOD to perform the simulations:

- Parameters: The simulation parameters are listed in Table S3.1.
- Materials: We defined two materials: air (refractive index = $n_{\text{air}} = 1$) and the grating material (refractive index = $n_{\text{mat}} = 1.5039$).
- Geometry: We created the geometry as per the structure being simulated (prism-type blazed grating or binary-type blazed grating of 3 or 5 cells). See Fig. S3.2 for the dimensions of the binary blazed gratings. This is same as that for the COMSOL based modelling in Section 2, except for the change in the orientation of the axes.
- EM waves launch: We used either TE or TM mode in the E-vector definition in Plane Wave Launce Options. We also set Launch Phi_r to 0 for normal incidence.
- Simulation: A single simulation to compute the full-fields and diffraction orders takes ~ 5 s, at 2 nm grid resolution.
- Multi-Variable Optimization and Scanning Tool (MOST): We parameterized 80 simulations for NA = 0.6 to 1 over 80 equally spaced points. The full simulation takes between 10-15 minutes, depending on the processor load.

Table S2.1: List of simulation parameters used in RSoft DiffractMOD modelling

| Parameter | Expression | Value | Description |
|------------------|----------------------------------|---------------|--------------------------------------|
| M | 20 | 20 | Number of harmonics |
| n_{air} | 1 | 1 | Refractive index of air |
| n_{mat} | 1.5039 | 1.5039 | Refractive index of grating material |
| lam0 | 647[nm] | 6.47E-7 m | Simulation wavelength |
| f_0 | $c_{\text{const}}/\text{lam0}$ | 4.6336E14 1/s | Frequency |
| alpha | 0.0[deg] | 0 rad | Angle of incidence |
| gh | $\text{lam0}/(n_{\text{mat}}-1)$ | 1.284E-6 m | Grating height |
| NA | 0.6 | 0.6 | Numerical aperture |
| gp | $\text{lam0}/\text{NA}$ | 1.0783E-6 m | Grating period |
| dpad | 2[um] | 2E-6 m | Padding depths |
| res | 2[nm] | 2E-9 m | Resolution (grid size) |

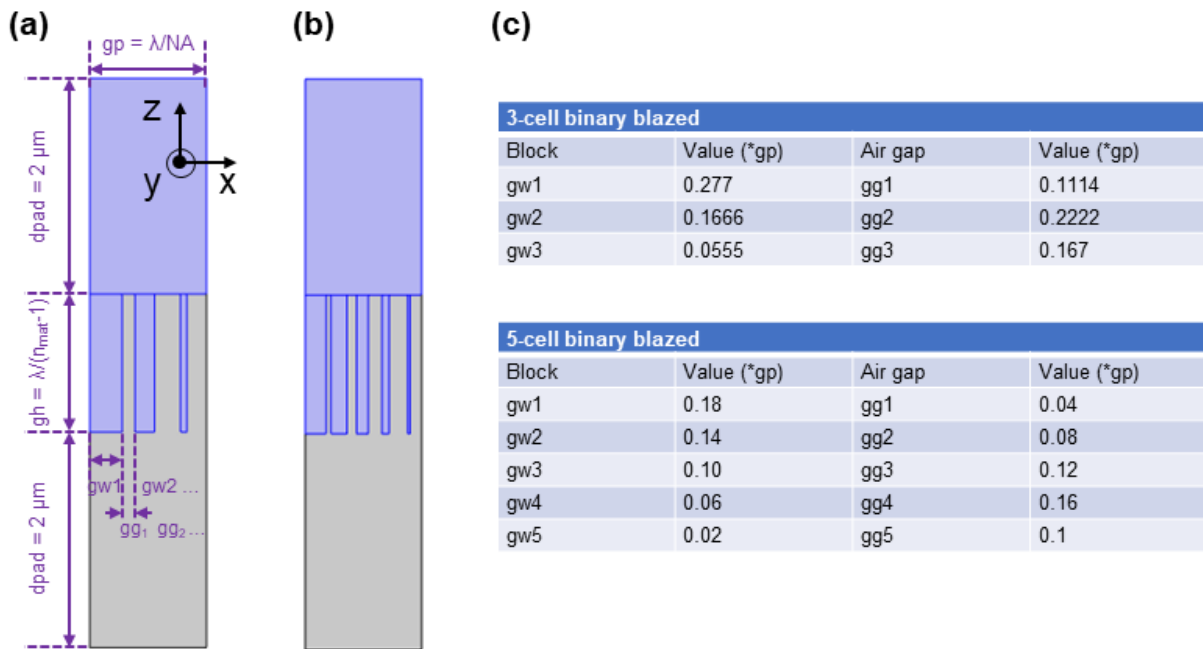


Fig. S3.2: Schematic diagram showing the (a) 3-cell and (b) 5-cell binary blazed gratings along with the values of the grating sub-pillar width (g_{w_n}) and grating sub-pillar gap (g_{g_n}).

3.2. Convergence study

In order to ensure proper convergence of the RCWA numerical solutions, we tested different grid resolution and number of harmonics. The results achieve convergence when there is no change in the results with increasing the resolution of the grid, i.e. making the grid size smaller or with increase in the number of harmonics. RSoft's DiffractMOD is based on the Rigorous Coupled Wave Analysis (RCWA) method and implements several advanced algorithms including a fast converging formulation of Maxwell equations and a numerical stabilization scheme. We observed that convergence is achieved for a grid resolution of 8 nm, yet we chose to simulate at higher resolution of 2 nm grid size since the computation is fast. Similarly, we chose $M = 20$ as the number of harmonics which is more than sufficient for convergence. Fig. S3.3 (a and d) show the first order transmission diffraction efficiency vs NA for the grid sizes = 1, 2, 5 and 8 nm for TE and TM illumination, respectively. The steady state light intensity in the computation cell for NA = 0.6, 0.75, and 0.995 for grid sizes = 1 and 2 nm for TE is shown in Fig. S3.3(b-c) and for TM is shown in Fig. S3.3(e-f). We observed no change in the results from decreasing the grid size from 2 to 1 nm and thus concluded that 2 nm is sufficient for achieving accurate results.

Next, we performed convergence study for number of harmonics (M). The results comparing three values 10, 15 and 20 are shown in Fig. S3.4 for TE and TM illumination. It was observed that $M = 10$ is sufficient. However, since the computation was fast, we chose $M = 20$.

Thus, all the following results were computed using a 2 nm grid size and number of harmonics = 20.

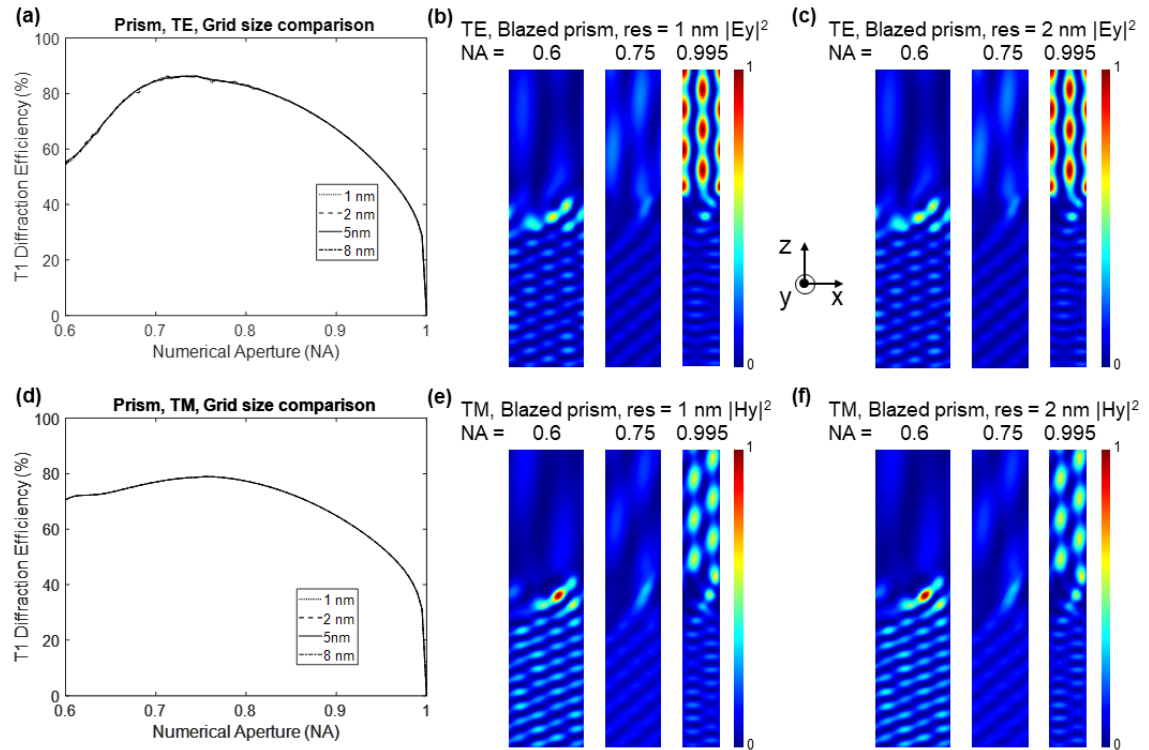


Fig. S3.3: Results of convergence study for grid resolution. (a) First order transmission diffraction efficiency vs NA for grid sizes = 1, 2, 5 and 8 nm for TE illumination. Steady-state light intensity distribution in the computational cell for NA = 0.6, 0.75, and 0.995 for (b) TE and 1 nm grid size and (c) TE and 2 nm grid size. (d) First order

transmission diffraction efficiency vs NA for grid sizes = 1, 2, 5 and 8 nm for TM illumination. Steady-state light intensity distribution in the computational cell for NA = 0.6, 0.75, and 0.995 for (e) TM and 1 nm grid size and (f) TM and 2 nm grid size.

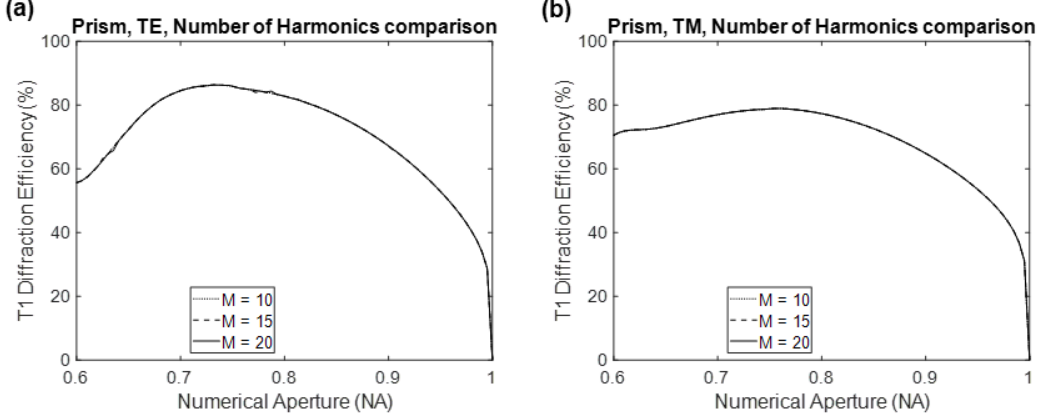


Fig. S3.4: Results of convergence study for number of harmonics. First order transmission diffraction efficiency vs NA for number of harmonics (M) = 10, 15, and 20 for (a) TE illumination and (b) TM illumination.

3.3. Simulation results for prism type blazed grating

The simulation results for the prism-type blazed grating for TE and TM illumination are shown in Fig. S3.5 and S3.6, respectively. In each case, we show the full transmission and diffraction orders vs NA for the 5 cases: (a) free grating, (b) infinite superstrate, (c) finite superstrate, (d) infinite substrate, and (e) finite substrate cases. Finally, we calculated the first-order transmission diffraction efficiency for the 5 cases, extracting data from (a-e), and defining this as the ratio of the power diffracted into the first transmitted order to the total transmitted power in percentage. The value of the first-order transmission diffraction efficiency vs NA is shown in panel (f) in Fig. S3.5 and S3.6.

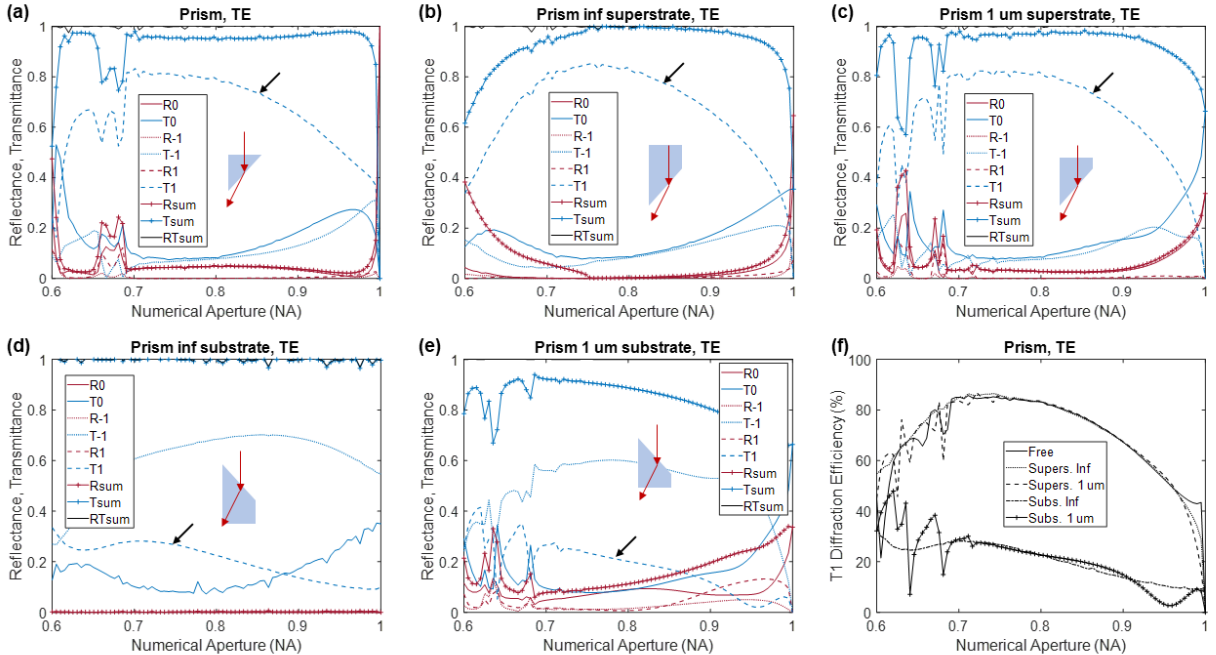


Fig. S3.5: Simulation results for TE illumination showing all transmission and diffraction orders vs NA for prism-type blazed grating for (a) free grating, (b) infinite superstrate, (c) finite superstrate, (d) infinite substrate, and (e) finite substrate cases. The first transmitted order is pointed out by the black arrow. (f) First-order transmission diffraction efficiency for the 5 cases, extracted from (a-e). We noted the presence of +/- 2nd reflected and transmitted orders for NA<0.8 in (b) and (d) respectively, but they have not been plotted here.

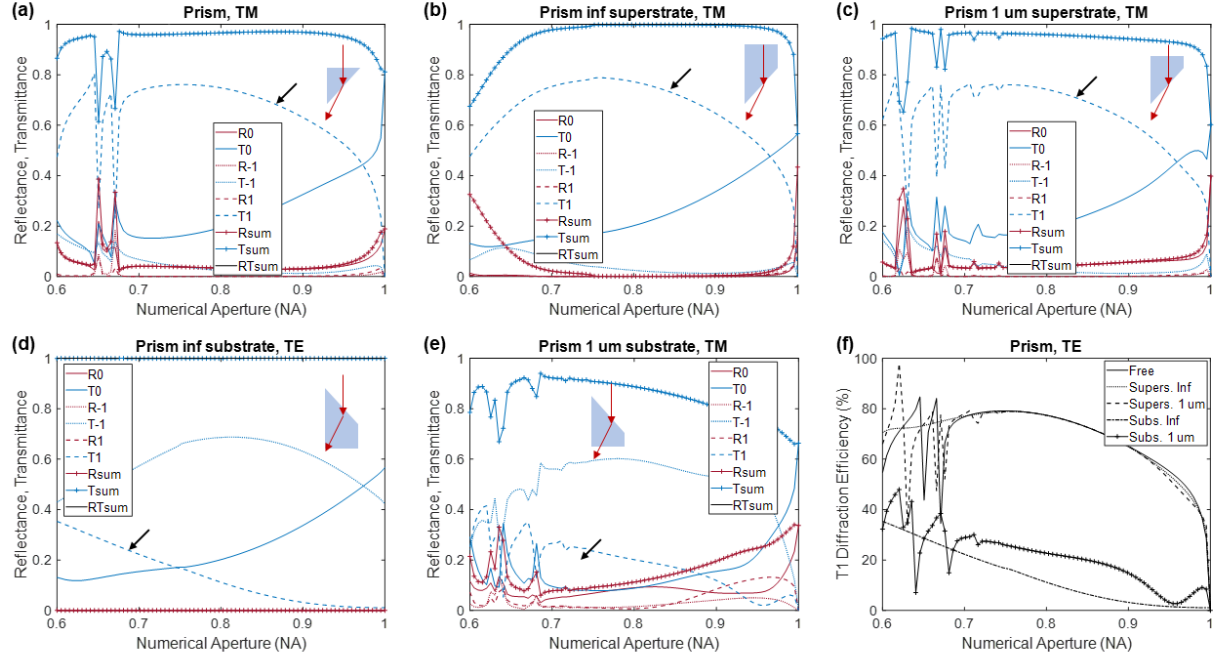


Fig. S3.6: Simulation results for TM illumination showing all transmission and diffraction orders vs NA for prism-type blazed grating for (a) free grating, (b) infinite superstrate, (c) finite superstrate, (d) infinite substrate, and (e) finite substrate cases. The first transmitted order is pointed out by the black arrow. (f) First-order transmission diffraction efficiency for the 5 cases, extracted from (a-e). We noted the presence of +/- 2nd reflected and transmitted orders for NA<0.8 in (b) and (d) respectively, but they have not been plotted here.

The steady-state light intensity inside the computational cell for three values of NA, 0.6, 0.75 and 0.995, for the infinite superstrate case are shown for the TE and TM illumination cases in Fig. S3.7 (a) and (b), respectively.

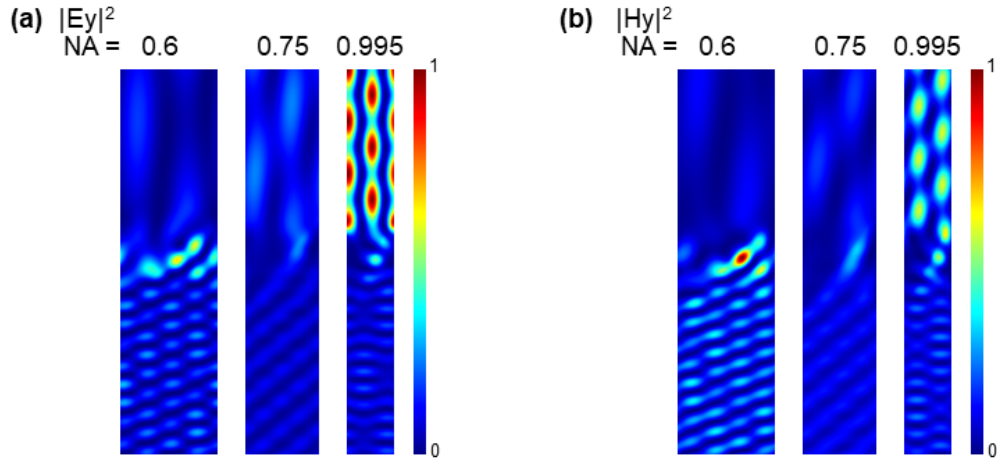


Fig. S3.7: Steady-state light intensity inside the computational cell for three values of NA, 0.6, 0.75 and 0.995, for the infinite superstrate case are shown for (a) TE and (b) TM illuminations.

3.4. Simulation results for 3-cell binary blazed grating

The simulation results for the 3-cell binary blazed grating for TE and TM illumination are shown in Fig. S3.8 and S3.9, respectively. In each case, we show the full transmission and diffraction orders vs NA for the 5 cases: (a) free grating, (b) infinite superstrate, (c) finite superstrate, (d) infinite substrate, and (e) finite substrate cases. The value of the first-order transmission diffraction efficiency (calculated in the same way as described in Section 2.3) vs NA is shown in panel (f) in Fig. S3.8 and S3.9.

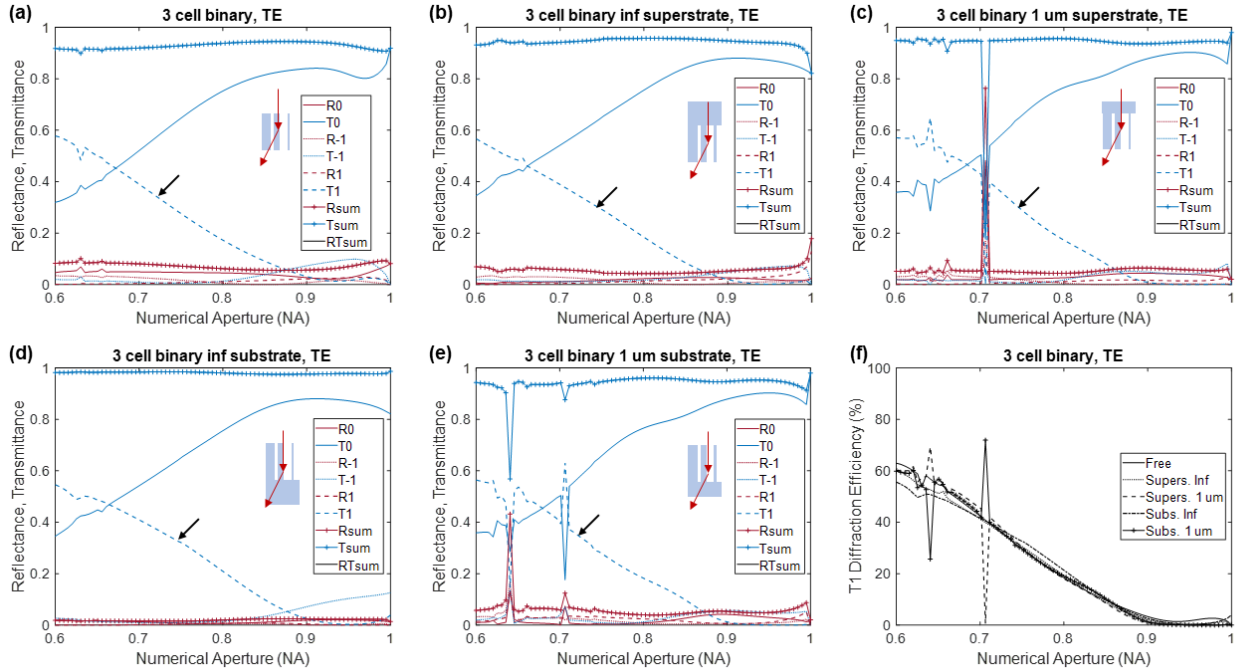


Fig. S3.8: Simulation results for TE illumination showing all transmission and diffraction orders vs NA for 3-cell binary blazed grating for (a) free grating, (b) infinite superstrate, (c) finite superstrate, (d) infinite substrate, and (e) finite substrate cases. The first transmitted order is pointed out by the black arrow. (f) First-order transmission diffraction efficiency for the 5 cases, extracted from (a-e). We noted the presence of +/- 2nd reflected and transmitted orders for NA<0.8 in (b) and (d) respectively, but they have not been plotted here.

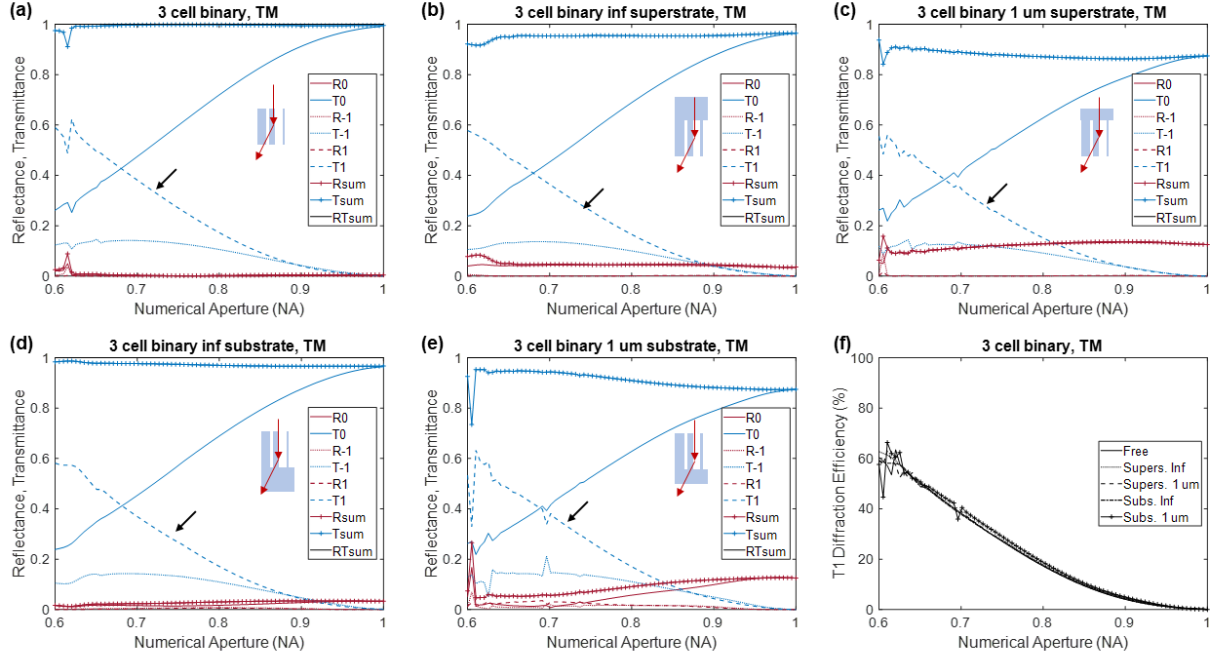


Fig. S3.9: Simulation results for TM illumination showing all transmission and diffraction orders vs NA for 3-cell binary blazed grating for (a) free grating, (b) infinite superstrate, (c) finite superstrate, (d) infinite substrate, and (e) finite substrate cases. The first transmitted order is pointed out by the black arrow. (f) First-order transmission diffraction efficiency for the 5 cases, extracted from (a-e). We noted the presence of +/- 2nd reflected and transmitted orders for NA<0.8 in (b) and (d) respectively, but they have not been plotted here.

The steady-state light intensity inside the computational cell for three values of NA, 0.6, 0.75 and 0.995, for the infinite superstrate case are shown for the TE and TM illumination cases in Fig. S3.10 (a) and (b), respectively.

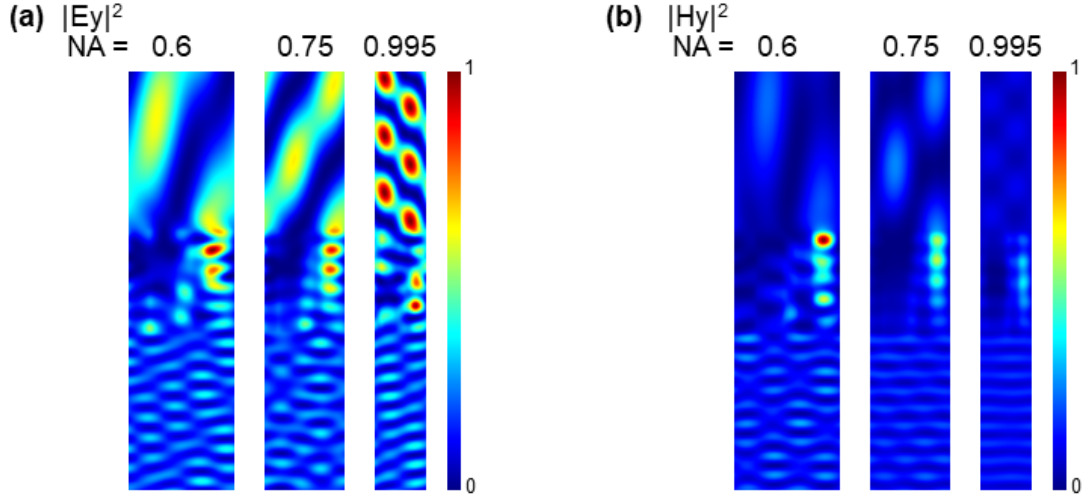


Fig. S3.10: Steady-state light intensity inside the computational cell for three values of NA, 0.6, 0.75 and 0.995, for the infinite superstrate case are shown for (a) TE and (b) TM illuminations.

3.5. Simulation results for 5-cell binary blazed grating

The simulation results for the 5-cell binary blazed grating for TE and TM illumination are shown in Fig. S3.11 and S3.12, respectively. In each case, we show the full transmission and diffraction orders vs NA for the 5 cases: (a) free grating, (b) infinite superstrate, (c) finite superstrate, (d) infinite substrate, and (e) finite substrate cases. The value of the first-order transmission diffraction efficiency (calculated in the same way as described in Section 2.3) vs NA is shown in panel (f) in Fig. S3.11 and S3.12.

The steady-state light intensity inside the computational cell for three values of NA, 0.6, 0.75 and 0.995, for the infinite superstrate case are shown for the TE and TM illumination cases in Fig. S3.13 (a) and (b), respectively.

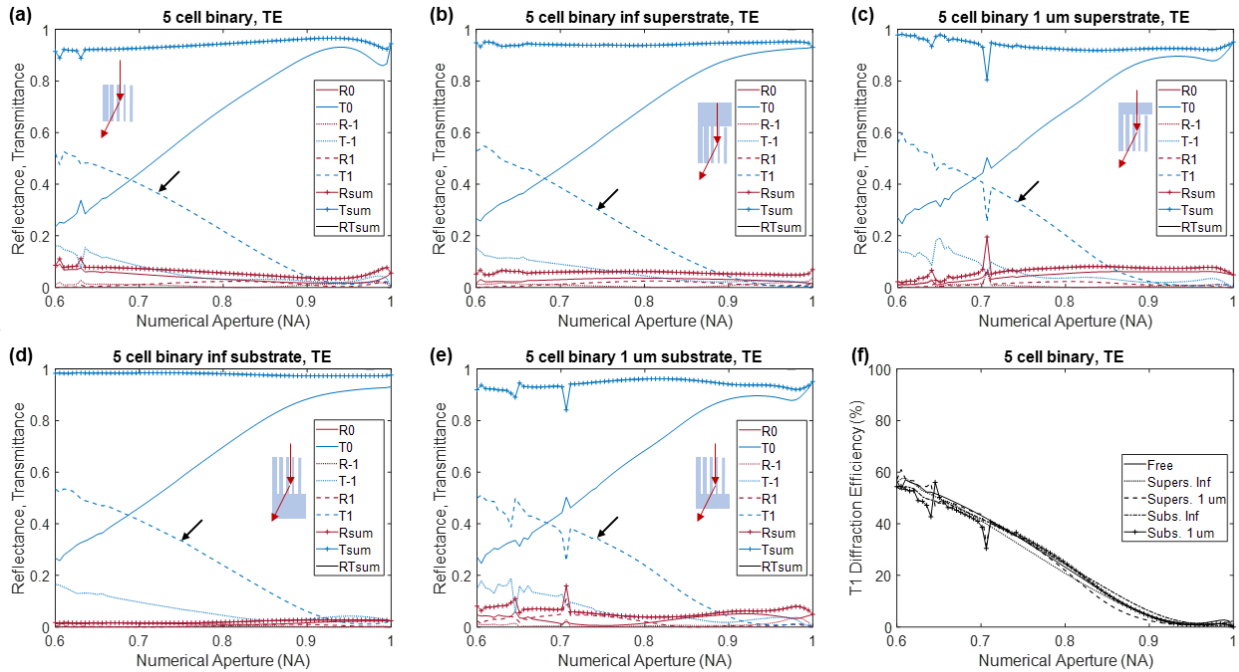


Fig. S3.11: Simulation results for TE illumination showing all transmission and diffraction orders vs NA for 5-cell binary blazed grating for (a) free grating, (b) infinite superstrate, (c) finite superstrate, (d) infinite substrate, and (e) finite substrate cases. The first transmitted order is pointed out by the black arrow. (f) First-order transmission diffraction efficiency for the 5 cases, extracted from (a-e). We noted the presence of +/- 2nd reflected and transmitted orders for NA<0.8 in (b) and (d) respectively, but they have not been plotted here.

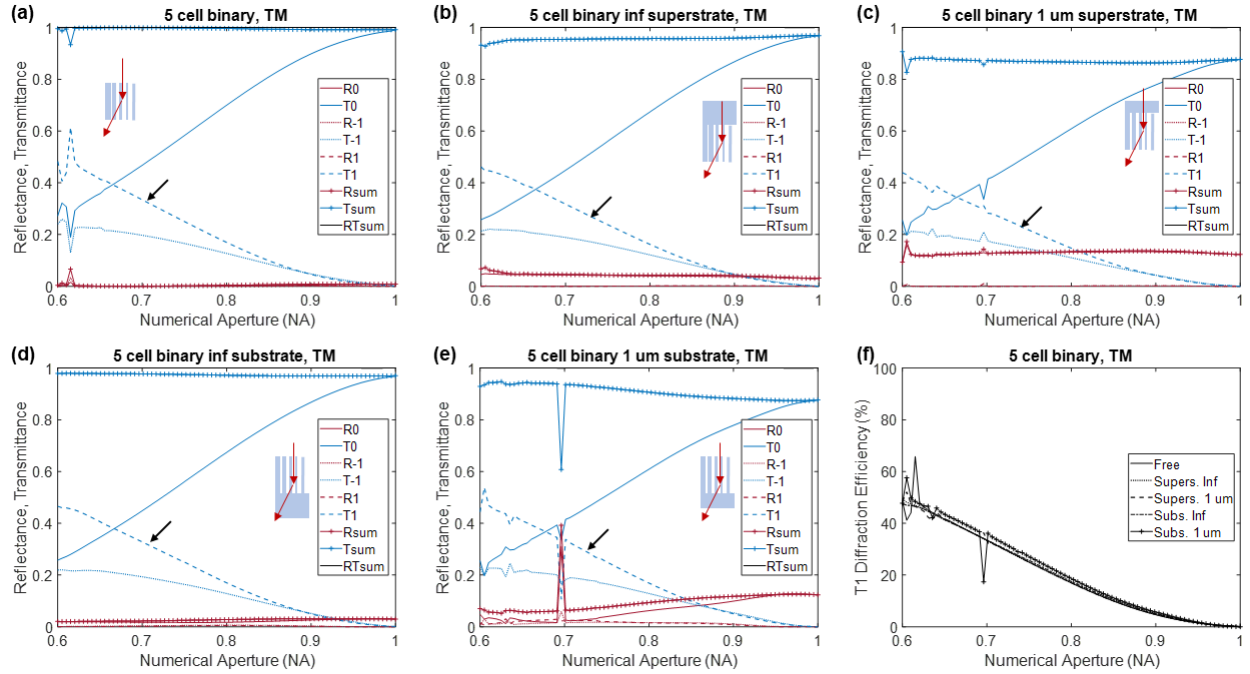


Fig. S3.12: Simulation results for TM illumination showing all transmission and diffraction orders vs NA for 5-cell binary blazed grating for (a) free grating, (b) infinite superstrate, (c) finite superstrate, (d) infinite substrate, and (e) finite substrate cases. The first transmitted order is pointed out by the black arrow. (f) First-order transmission diffraction efficiency for the 5 cases, extracted from (a-e). We noted the presence of +/- 2nd reflected and transmitted orders for NA<0.8 in (b) and (d) respectively, but they have not been plotted here.

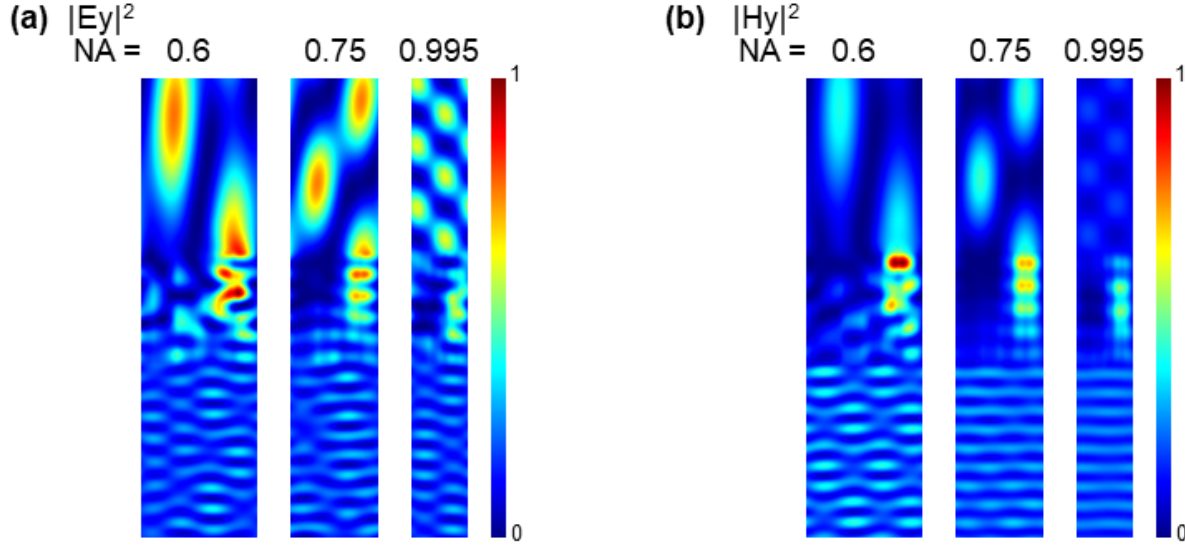


Fig. S3.13: Steady-state light intensity inside the computational cell for three values of NA, 0.6, 0.75 and 0.995, for the infinite superstrate case are shown for (a) TE and (b) TM illuminations.

We show the first order transmission diffraction efficiency for the infinite superstrate and substrate cases in Fig. S3.14. This data is extracted from panel (f) of Fig. S3.5, Fig. S3.6, Fig. S3.8, Fig. S3.9, Fig. S3.11, and Fig. S3.12.

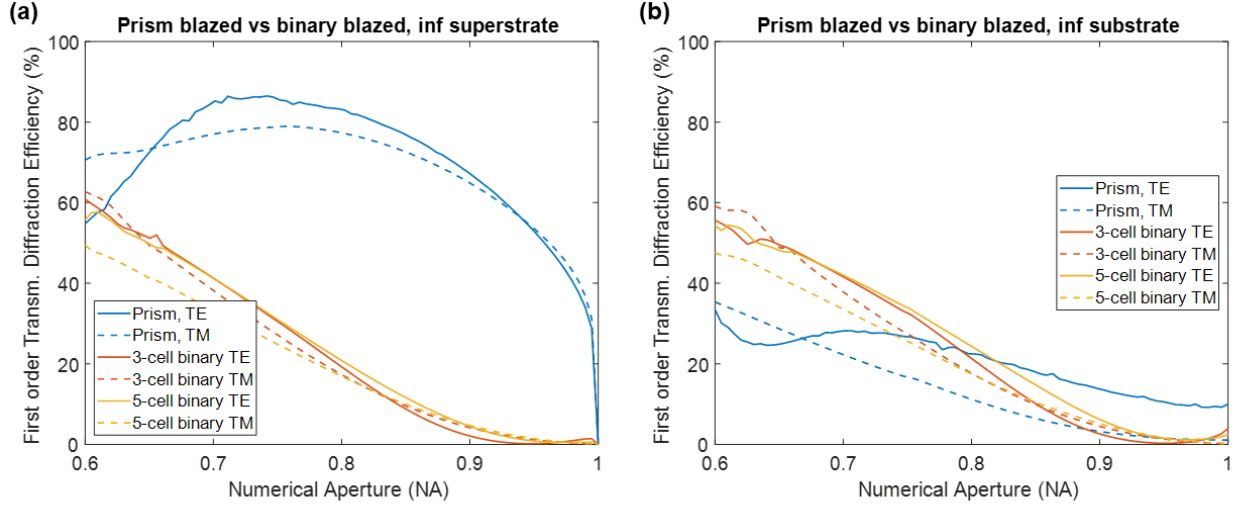


Fig. S3.14: First order transmission diffraction efficiency for the (a) infinite superstrate and (b) infinite substrate cases.

The results of the performance comparison shown in Fig. 2 (main text) assumed light incident from the material side, which we call the superstrate case. Under this situation, the prism-type grating outperforms the meta-grating at high numerical apertures. We used RCWA for these simulations. Additionally, we also studied the case when the light is incident from the air side, which we call the substrate case. We also used FEM analysis to validate the simulations. Although we noticed minor discrepancies between RCWA (RSoft) and FEM (COMSOL), the overall trend was similar. Our findings are similar to a previous work. [5] It was traditionally understood that prism-type blazed gratings suffer from shadowing effect, [6] but we point out using geometric optics that for the superstrate case, the shadowing effect does not exist (see section 6).

4. Simulation of gratings using Gsolver.

The details of the grating geometries are summarized below.

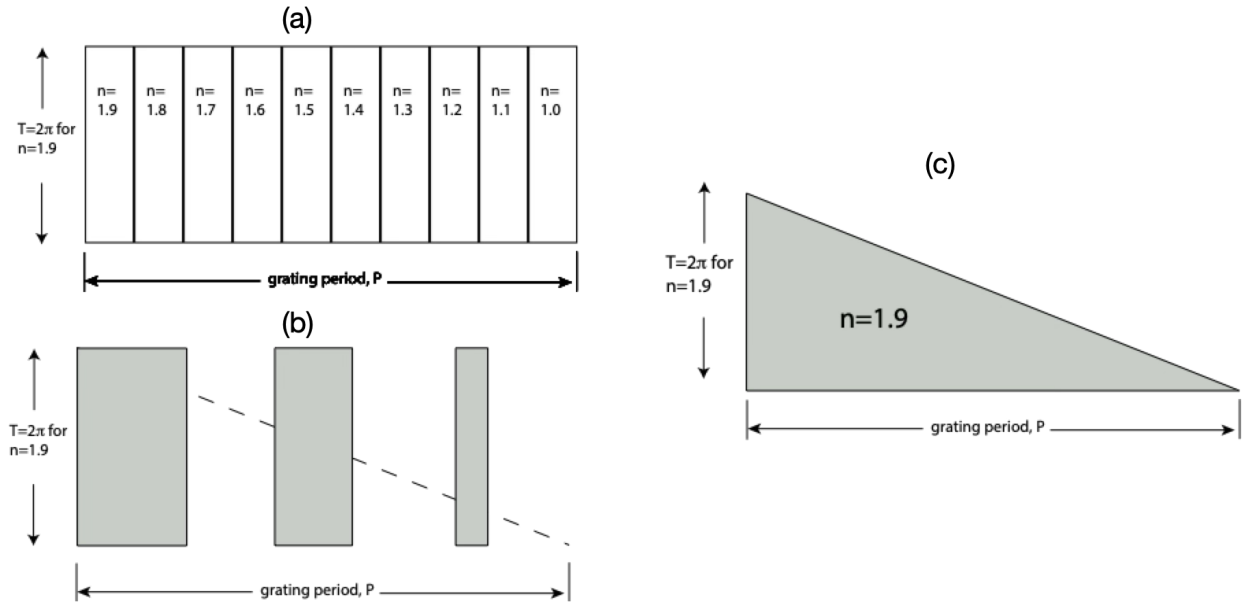


Fig. S4.1: (a) 10-step refractive index blaze, i.e., the thickness is fixed at a value that would produce a 2π phase shift in transmitted light. Across the period the index is dropped in 10 equal stages from $n=1.9$ to $n=1$. Intuitively, one would consider this is ideal but it is not achievable in practice. (b) Effective-index blaze. The thickness is fixed to correspond to 2π phase shift. The grating period is divided into cells smaller than a wavelength. The diagram shows 3 cells. The width of each dielectric ridge in each cell is adjusted to simulate linear drop of the refractive index and prism blazes. Note the dotted line traces the slope of the prism blaze. We simulate the slope with partial filling. (c) The prism blaze, i.e the thickness of the dielectric material is triangular shaped with maximum thickness corresponding to 2π phase shift. This is the traditional blazed grating.

Table below summarizes the simulated efficiencies.

| NA | blazed / TE | meta / TE | blazed / TM | meta / TM |
|----------|-------------|-----------|-------------|-----------|
| 0.998996 | 11% | 2% | 13% | 0% |
| 0.969071 | 44% | 9% | 44% | 1% |
| 0.940886 | 56% | 13% | 53% | 3% |
| 0.914294 | 64% | 17% | 59% | 5% |
| 0.889164 | 71% | 21% | 64% | 7% |
| 0.865378 | 75% | 25% | 68% | 9% |
| 0.842832 | 79% | 29% | 70% | 11% |
| 0.821431 | 81% | 32% | 73% | 14% |
| 0.80109 | 83% | 35% | 74% | 16% |

| | | | | |
|----------|-----|-----|-----|-----|
| 0.781731 | 84% | 38% | 75% | 19% |
| 0.763287 | 84% | 40% | 76% | 21% |
| 0.745692 | 84% | 43% | 76% | 23% |
| 0.728891 | 81% | 45% | 74% | 25% |
| 0.71283 | 78% | 47% | 73% | 27% |
| 0.697461 | 75% | 48% | 72% | 29% |
| 0.682742 | 72% | 50% | 71% | 31% |
| 0.66863 | 68% | 51% | 68% | 33% |
| 0.65509 | 62% | 52% | 65% | 35% |
| 0.642088 | 56% | 53% | 62% | 36% |
| 0.629592 | 49% | 53% | 57% | 38% |
| 0.617573 | 42% | 55% | 53% | 38% |

5. Numerical simulations from Ref. 11 in main text:

We reproduce Fig. 2f from Ref. 11 (main text) below to indicate the calculated diffraction efficiencies therein. We further confirmed with the authors of the paper that these plots are created assuming a focal-spot radius of $3 \times \text{FWHM}$. Note that this simulation was performed by the authors of Ref. 11 for lens diameter of $20 \mu\text{m}$.

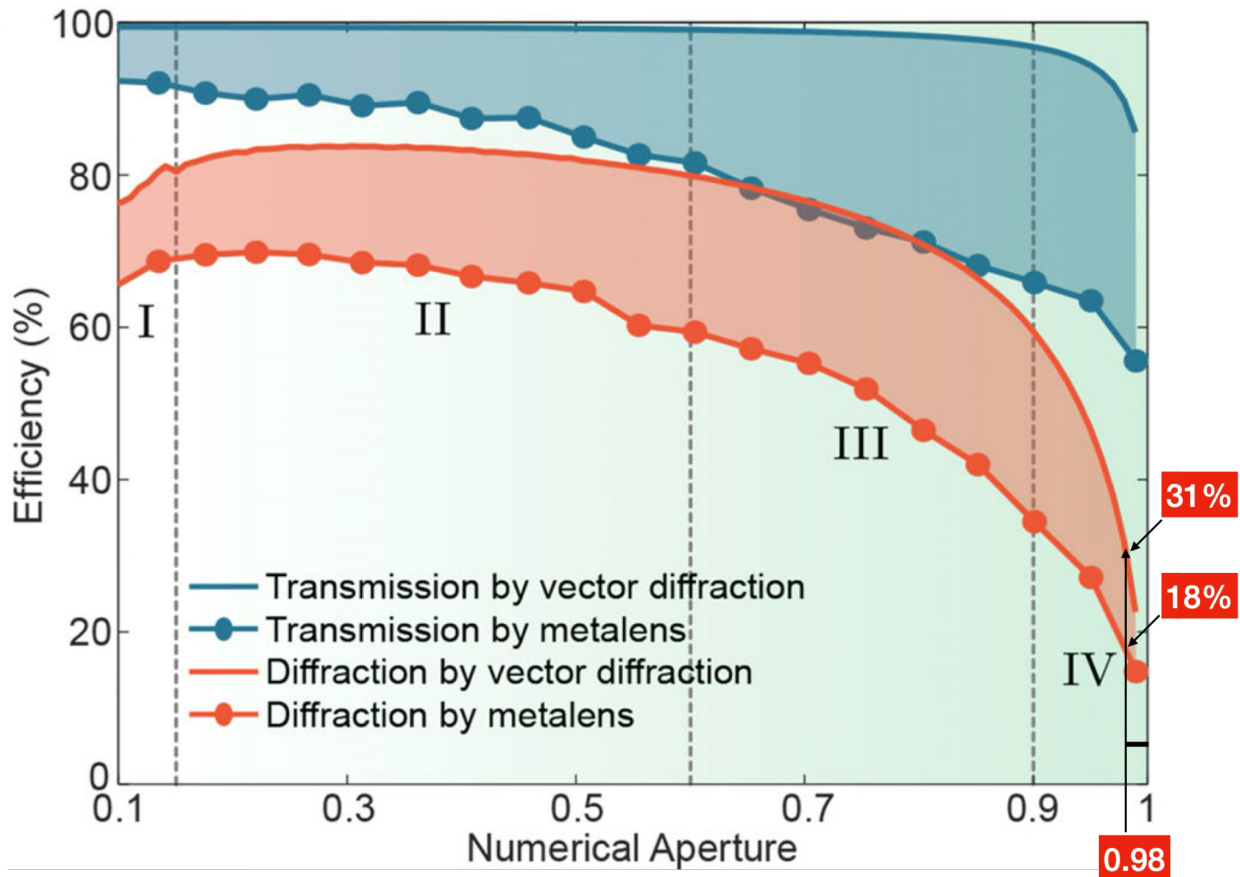


Fig. S5.1: Theoretical upper bound of flat-lens efficiencies. We have noted the efficiencies for $\text{NA} = 0.98$.

6. Shadow effect depends upon direction of incidence

Figure S6.1 illustrates how shadowing varies with the direction of incident light. When light is incident from the “superstrate,” ray tracing shows no shadowing occurs. In contrast, illumination from the opposite direction results in expected shadowing. This observation aligns with the simulations discussed in Section 4. In the main text, we compare illumination from the superstrate for both the Fresnel Zone Plate (FZP) and the metlens, as this configuration avoids shadowing and achieves the highest efficiency.

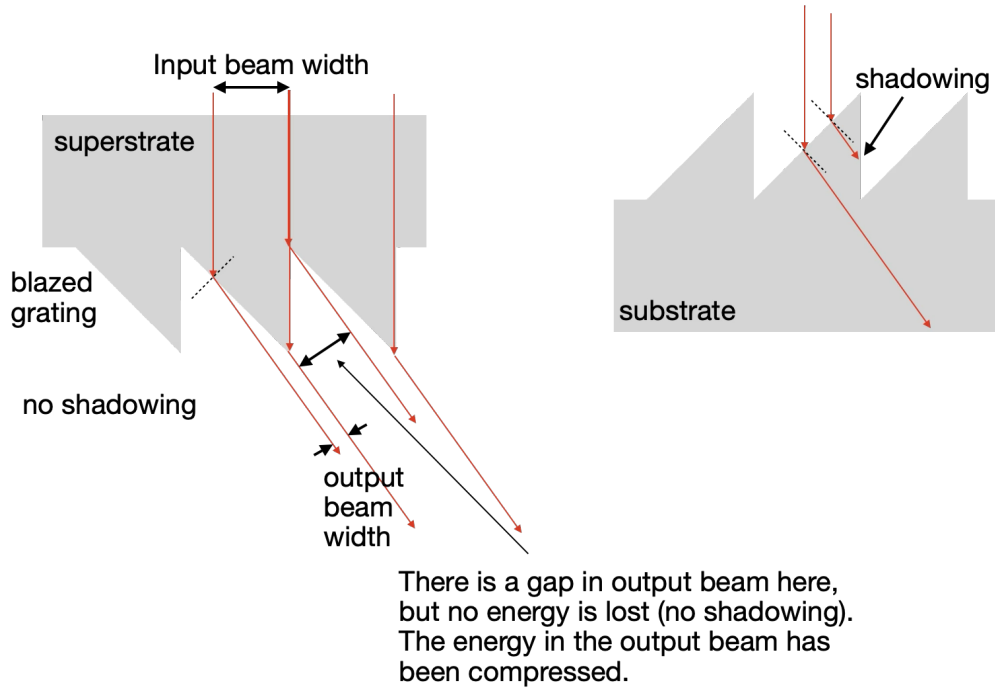


Fig. S6.1: Shadowing occurs when diffracted light encounters an interface that partially reflects it, reducing diffraction efficiency. In the left panel, with incidence from the superstrate, no shadowing is observed. In contrast, the right panel shows significant shadowing for incidence from air.

7. Experiments.

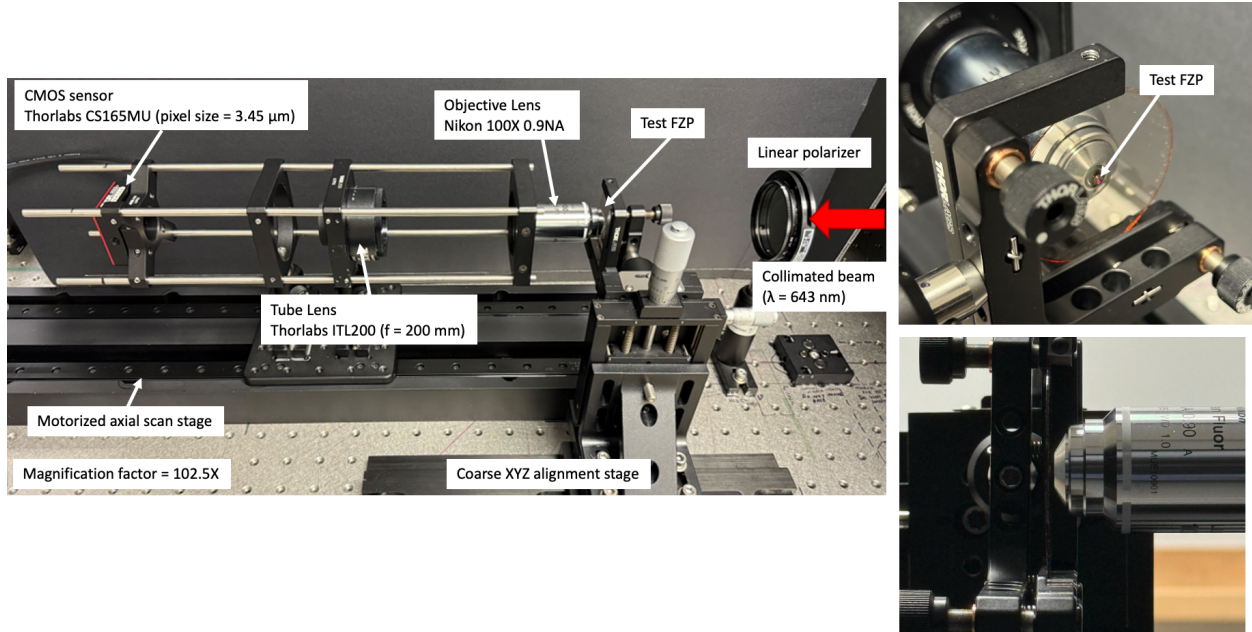


Fig. S7.1 Experimental setup for magnification of the PSF of the FZP.

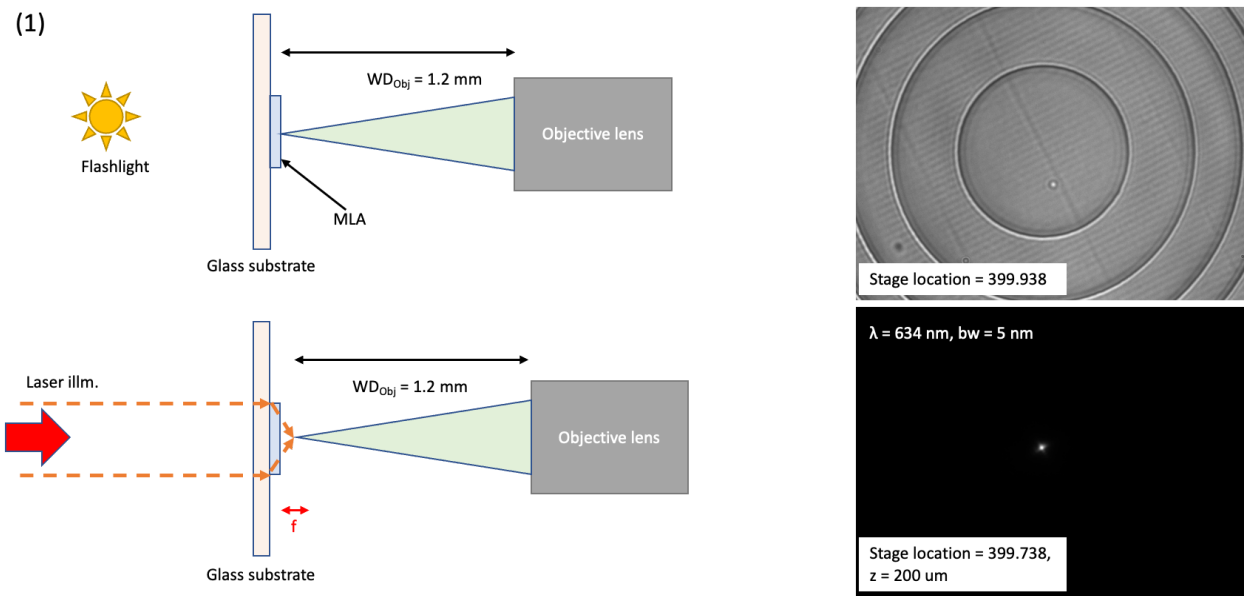


Fig. S7.2 Experimental setup for illumination from superstrate (+Z direction). First, the MLA is brought in focus of the Objective lens by illuminating from behind using LED flashlight. Patterned side faces measurement setup. Next, the Objective is moved back by the expected focal length to search for the PSF. In this case, the flashlight is removed and the collimated superK laser illumination is incident on the sample.

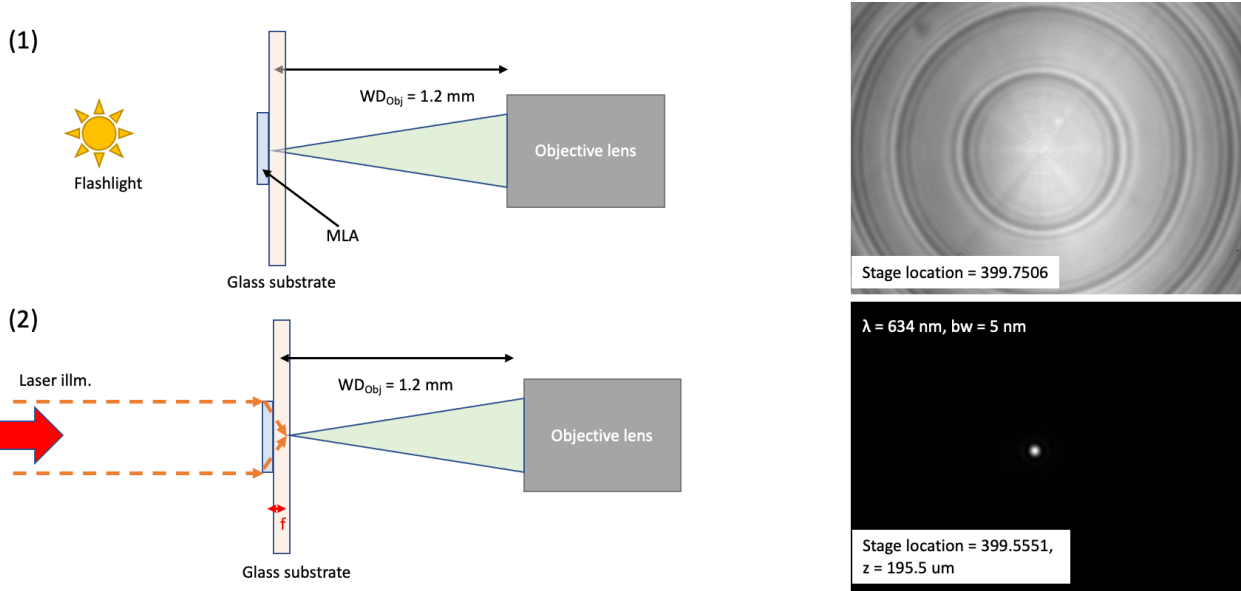


Fig. S7.3 Experimental setup for illumination from substrate (-Z direction). First, the MLA is brought in focus of the Objective lens by illuminating from behind using LED flashlight. Focusing is performed through the glass surface. Patterned side faces incident illumination. Next, the Objective is moved back by the expected focal length to search for the PSF. In this case, the flashlight is removed and the collimated superK laser illumination is incident on the sample.

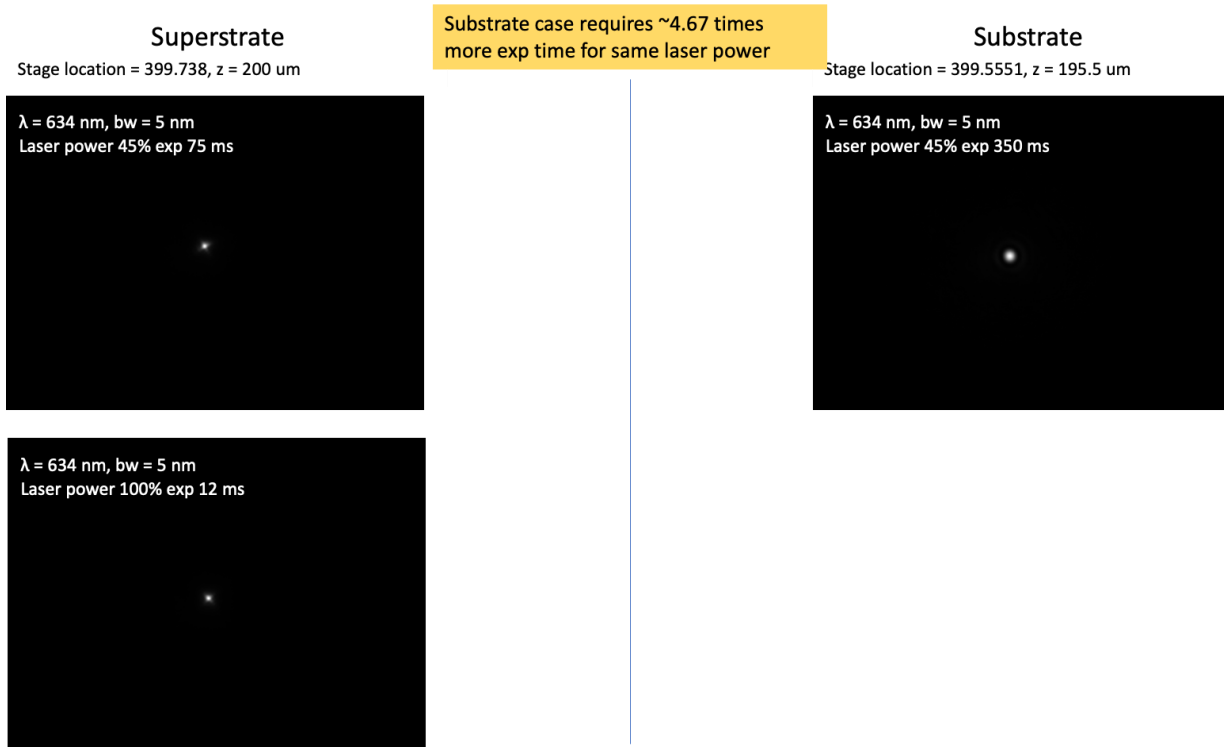


Fig. S7.4 Measured PSFs with different laser power. Superstrate refers to +Z direction, while substrate refers to -Z direction.

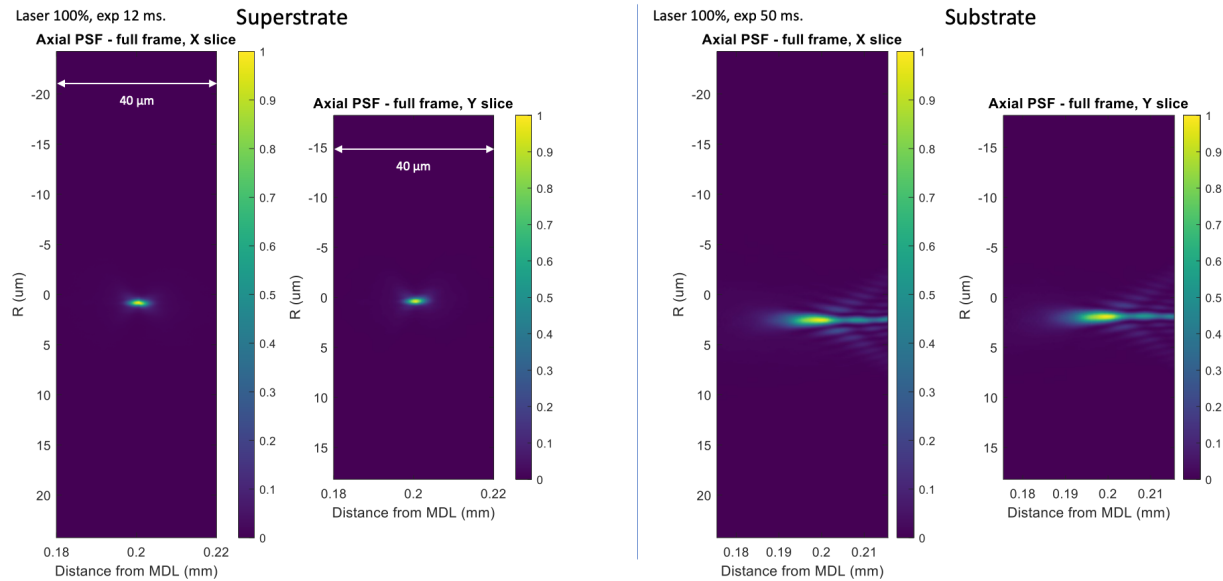


Fig. S7.5 Measured axial PSF full frame data. Scan length: +/- 20 μm on either side of best focal plane, Total length = 40 μm , Step size = 0.1 μm , Number of steps = 400, $\lambda = 634 \text{ nm}$, bw = 5nm (set using VARIA).

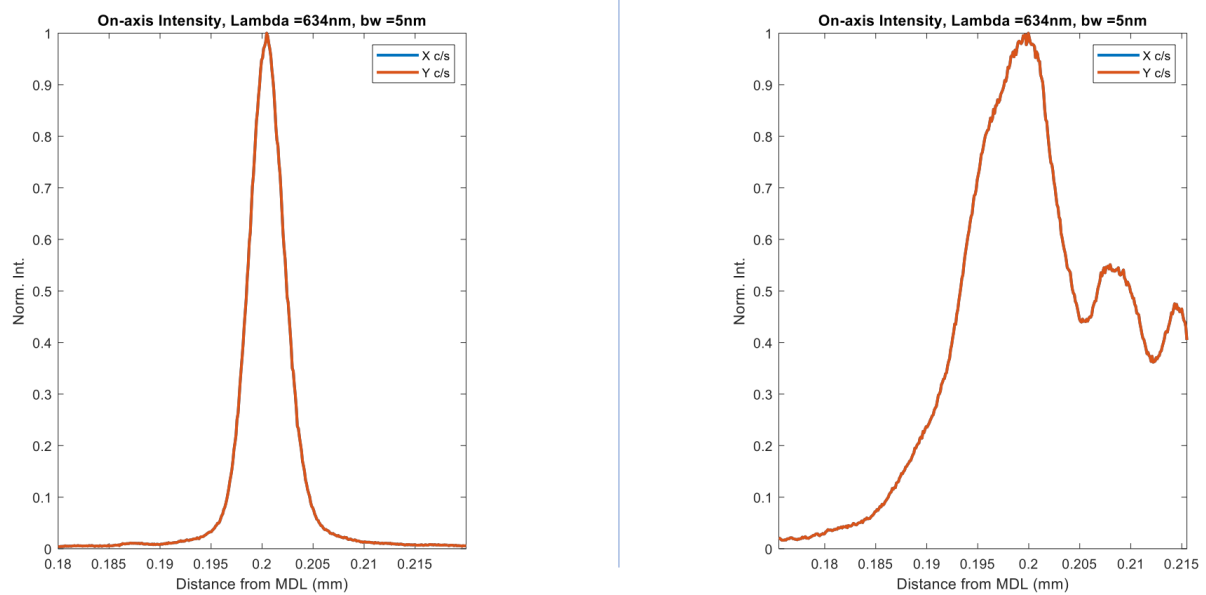


Fig. S7.6 Measured on-axis PSF data. Scan length: +/- 20 μm on either side of best focal plane, Total length = 40 μm , Step size = 0.1 μm , Number of steps = 400, $\lambda = 634 \text{ nm}$, bw = 5nm (set using VARIA).

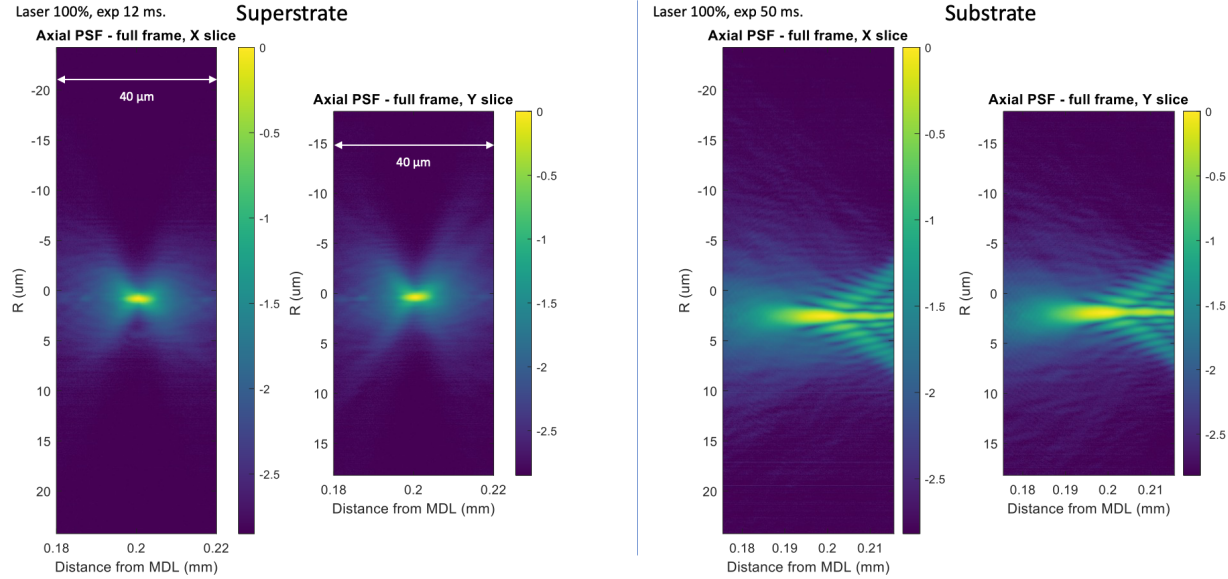


Fig. S7.7 Measured axial PSF data, full-frame log scale. Scan length: +/- 20 μm on either side of best focal plane, Total length = 40 μm , Step size = 0.1 μm , Number of steps = 400, $\lambda = 634 \text{ nm}$, $bw = 5\text{nm}$ (set using VARIA).

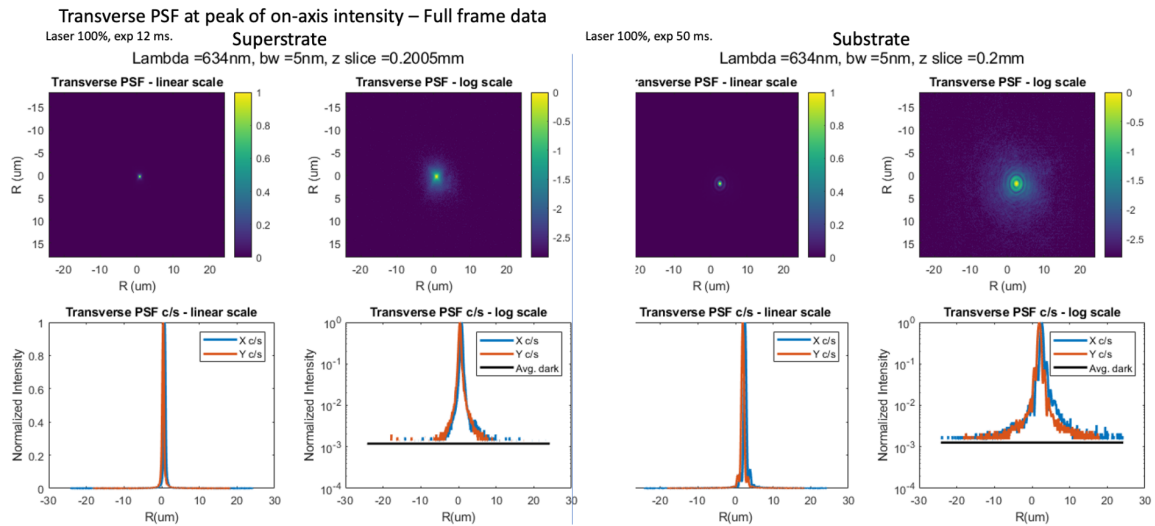


Fig. S7.8 Measured transverse PSFs at peak on-axis intensity location.

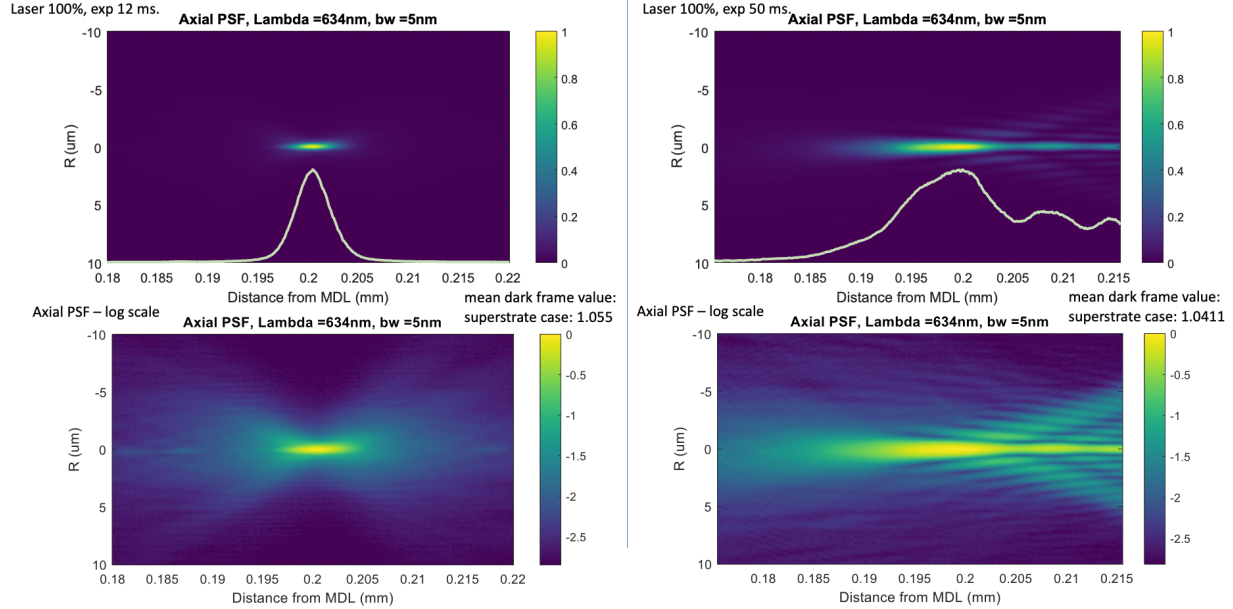


Fig. S7.9 Measured axial PSFs. Scan length: +/- 20 μm on either side of best focal plane, Total length = 40 μm , Step size = 0.1 μm , Number of steps = 400, $\lambda = 634 \text{ nm}$, bw = 5nm (set using VARIA).

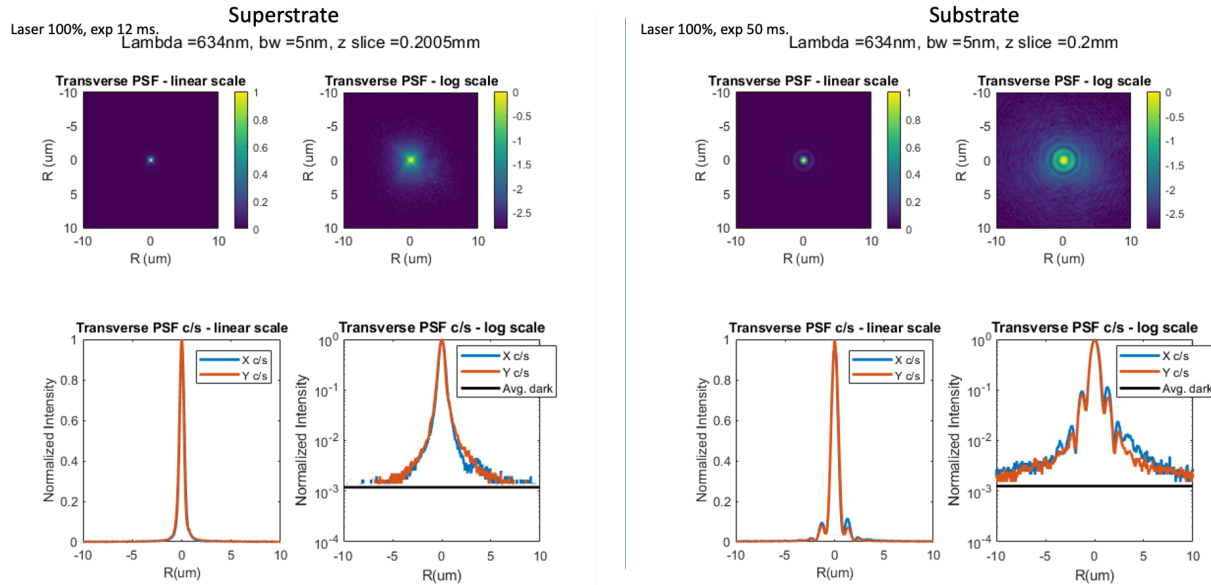


Fig. S7.10 Measured transverse PSFs. Scan length: +/- 20 μm on either side of best focal plane, Total length = 40 μm , Step size = 0.1 μm , Number of steps = 400, $\lambda = 634 \text{ nm}$, bw = 5nm (set using VARIA).

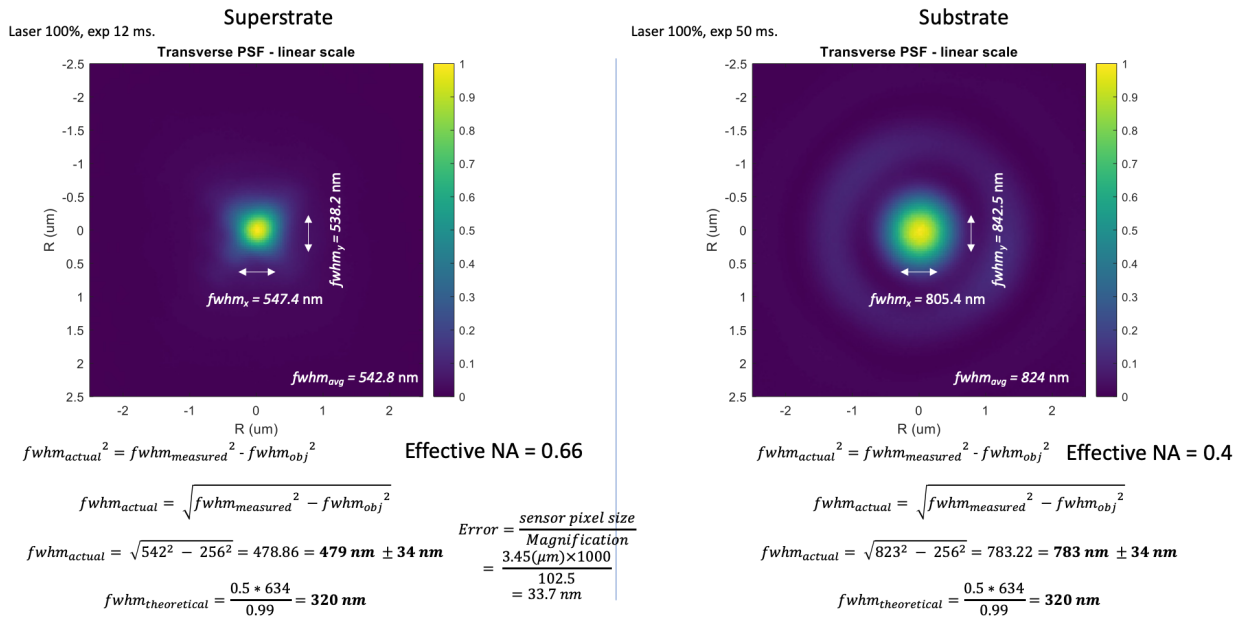


Fig. S7.11 Estimating FWHM in both directions of incidence.

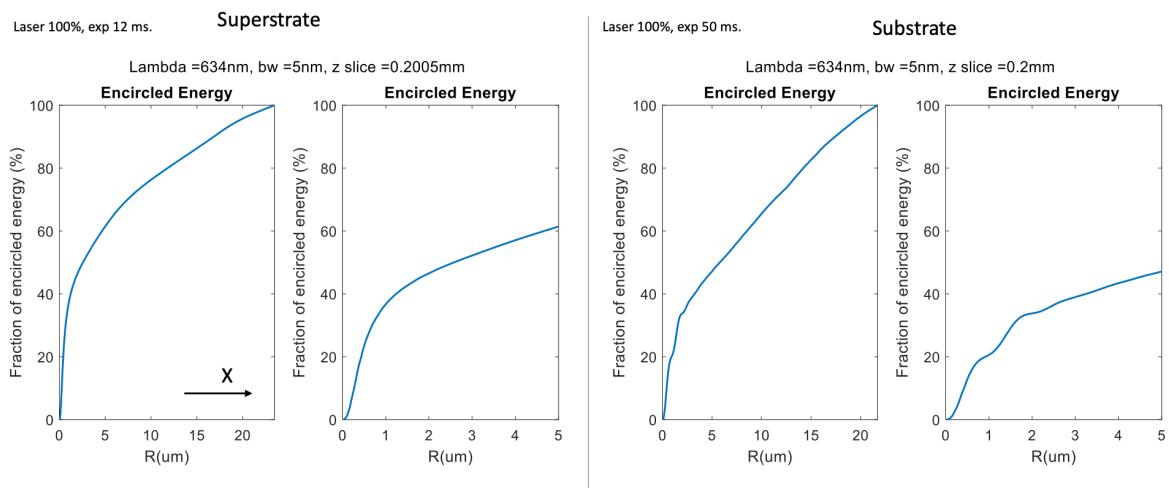


Fig. S7.12 Measured encircled energy for both directions of incidence.

References

1. <https://www.comsol.com/>
2. D. A. Pommet, M. G. Moharam, and E. B. Grann, "Limits of scalar diffraction theory for diffractive phase elements," *J. Opt. Soc. Am. A* 11, 1827–1834 (1994).
3. IPS resist, Nanoscribe.
4. <https://www.synopsys.com/photonic-solutions/rsoft-photonic-device-tools/passive-device-diffractmod.html>
5. M. Oliva, "High efficiency blazed gratings in resonance domain," Dissertation zur Erlangung des akademischen Grades Doktor-Ingenieur (Dr.-Ing.), Friedrich-Schiller-Universität Jena (2014).
6. P. Lalanne, S. Astilean, P. Chavel, E. Cambril, and H. Launois, "Design and fabrication of blazed binary diffractive elements with sampling periods smaller than the structural cutoff," *J. Opt. Soc. Am. A* 16, 1143-1156 (1999).